The Determination of Atom-Molecule Interaction Potentials from Total Differential Cross Sections

Thesis by
Michael John O'Loughlin

In Partial Fulfillment of the Requirements
for the Degree of
Doctor of Philosophy

California Institute of Technology
Pasadena, California
1986
(Submitted October 4, 1985)

To Kathy

Acknowledgements

First and foremost, I wish to thank my wife and best friend, Kathleen, whose unceasing love and companionship have been a constant source of energy and strength. She also deserves alot of credit for typing a majority of this thesis. My parents are also deserving of my gratitude. Their support has always been more deeply appreciated than I probably let them know.

Of the people I have known at Caltech, there have been far too many who have contributed advise, assistance and companionship to thank everyone personally. Not the least of these contributors is my advisor, Randy Sparks, who was always willing to let me have a "free hand" even though this sometimes led to catastrophic results. My coworker and friend of four years, Brian Reid, deserves a tremendous amount of credit for this thesis. Without Brian, I probably would still be assembling the apparatus. His knowledge and perfectionism have never ceased to amaze me.

Ken Janda and his coworkers, Bas, Bubba, Dwight, Francis, Joe and Sally were always gracious hosts and stimulating conversationalists. The many interesting activities, both scientific and otherwise, I have shared with these individuals are some of my fondest memories of Caltech. Dwight, Joe and Sally also deserve a special thanks for enduring wave after wave of rough drafts of this thesis.

The shop personnel were very instrumental in the construction and emergency maintenance of my apparatus. In particular, Bill, Delmer, Guy, Jack, the Jims, Ray, Tom and Tony have all been very helpful. Their friendship is also very much appreciated. For all those people I have failed to mention, suffice it to say that I have enjoyed my stay at Caltech and the interaction with all the members of the Division and the community with whom I have had contact.

Abstract

A newly constructed crossed molecular beams apparatus has been used to measure total (elastic plus inelastic) differential cross sections for collisions between rare gas atoms and methane and chlorine molecules. The total differential cross sections were then used in an iterative trial and error potential fitting program to determine the interaction potentials between these species. In the rare gas-methane study (Chapter 2), the methane molecule has been approximated as being a spherical entity, and the standard equations and techniques have been applied to simulate the laboratory scattering distributions from an assumed isotropic potential. The isotropic potentials determined in this manner are compared with some recently proposed anisotropic potentials for these systems. In the rare gas-chlorine study (Chapter 3), anisotropic potentials have been determined using the infinite order sudden approximation and a Legendre parameter expansion of a central field potential. The resulting potentials compare rather favorably with what is known about these potential surfaces from photodissociation experiments.

Table of Contents

List of Figures

Chapter 1. Introduction

Chapter 2. Neon-Methane and Argon-Methane Isotropic Interaction Potentials from Total Differential Cross Sections

List of Tables

Appendix B. (continued)

Appendix C. Helium-Chlorine and Neon-Chlorine Experimental Data

Chapter 1

Introduction

1.1 Introduction

The forces of interaction between atoms and molecules have long been a subject of intense interest. These forces are fundamental in the analysis of the structure and properties of all matter, and yet for all but a small fraction of the simplest two body interactions, they have not been fully quantified. One of the best and most generally applicable methods for the determination of intermolecular forces is the measurement of collision cross sections using the crossed molecular beams technique. Although this technique is some 52 years old,[1] it has only come to fruition within the past quarter century. The crossed molecular beams technique employs two beams of atoms or molecules which intersect each other at a well defined angle. The scattering of the particles in one beam by the particles in the other beam is measured as a function of the angle through which those particles are scattered. This type of measurement, known as a differential cross section, is very sensitive to the potential energy function between the two particles and can be used to quantitatively analyze that potential. The actual analysis of experimental differential cross sections is difficult, although well defined, even for the simple atom-atom interactions. A significant number of atom-atom interaction potentials of very high quality have been reported in the past 15 years.[2-4] Recently, however, most efforts have been directed towards the understanding of the interaction of molecules with atoms or other molecules. The analysis of these experiments is inherently more complicated because the interparticle potential depends not only on the separation of the two particles but also on the relative orientations of the

molecules. In addition, inelastic scattering processes in which relative kinetic energy is transferred to or from the internal states of the molecules are also possible in the collision. In the studies described in this thesis, we have examined several atom-molecule interaction potentials using a simplistic extension of the well developed theories and methods[2,4-6] of the elastic scattering of atoms.

For the initial experiment on our newly constructed apparatus, we desired to undertake a study which would be relatively straightforward from an experimental viewpoint and yet would be topical. The determination of total (elastic plus inelastic) differential cross sections for methane with neon, argon and methane was just such an experiment. Methane potentials are of great interest because of their application in the theoretical modeling of the inter- and intramolecular interactions of larger organic molecules.[7,8] Also, the determination of total differential cross sections for an anisotropic system is equivalent experimentally to the well developed methodology for the measurement of elastic atom-atom differential cross sections. These total differential cross sections can be used to determine either effective spherical potentials[9-11] or estimates of the complete anisotropic potential surface.[12-14] In the case of methane, most of the approximate methods available for the calculation of differential cross sections from anisotropic potentials are not valid, and thus it would be necessary to use a computer intensive close-coupled calculation to determine the anisotropic surface. Since methane is somewhat spherical anyway, it was felt that effective spherical potentials would be sufficient. As an added attraction, an argon-methane potential had recently been reported

by Buck *et al.*[15] which would be very useful in our initial attempts to model our data. The results of the neon-methane and argon-methane studies are presented in Chapter 2 while the methane-methane results have been presented elsewhere.[16]

Our inability to determine the anisotropic potential energy surfaces for methane was not very intellectually satisfying. Thus, we decided to undertake a determination of a complete anisotropic potential for some system. Once again, we desired the atom-molecule potential be of some dynamical interest. In addition, it was required that the use of a simplifying approximation to the full quantum mechanical theory be a tenable treatment. For the past ten years there has been considerable interest in the photodissociation of van der Waals molecules of halogen molecules and rare gas atoms.[17] These systems have been used as simple models in the study of dynamical effects in the intramolecular redistribution of energy. Recently, Brinza *et al.*[18,19] have observed evidence of metastable, vibrationally excited neon-chlorine van der Waals molecules. This observation gives credence to the energy gap theory of Beswick and Jortner[20] and the momentum gap theory of Ewing.[21] Unfortunately, these theories cannot be tested or utilized to their fullest extent because very little information is known about the potential energy surfaces of either the ground or the excited state van der Waals molecule. To rectify this situation we have measured total differential cross sections for both neon-chlorine and helium-chlorine and determined anisotropic potential surfaces for each using the infinite order sudden (IOS) approximation. The preliminary results of these studies are presented in Chapter 3.

In the remainder of this chapter the fundamental aspects of the measurement of total differential cross sections and their use to determine both isotropic and anisotropic potentials will be discussed. Section 1.2 deals exclusively with the theory of intermolecular collisions. The apparatus which was constructed and utilized to perform these experiments is discussed extensively in Section 1.3, and in Section 1.4, the methodology used to determine laboratory differential cross sections and to extract knowledge of the intermolecular potential from those cross sections will be reviewed.

1.2 Molecular Collision Theory

Most of the details of molecular collision theory have been known for more than half a century,[22] and have been presented in great detail elsewhere.[2,4–6] The intention of this section is to systematically present those terms, concepts, and equations that are necessary for the comprehension of the studies detailed in the following chapters. Much attention has been paid to the theory of elastic scattering from isotropic potentials (Subsections 1.2.1 and 1.2.2) because the analysis of the methane systems of Chapter 2 was done exclusively in this manner. In addition, the IOS approximation used for the chlorine systems reduces the anisotropic potential problem to a sum over differential cross sections computed for isotropic potentials at fixed intermolecular orientations. The IOS approximation and conditions on its effectiveness will be examined in more detail in Subsection 1.2.3.

1.2.1 Classical Dynamics of Elastic Scattering

Although classical theory is not very useful for the actual quantitative determination of an intermolecular potential from elastic scattering, it is very helpful in examining elastic scattering from a qualitative viewpoint. In this section, the classical theory will be examined briefly with the emphasis on those features, such as "rainbow" scattering, which are more comprehensible in classical theory than in the quantum approach.

The collision between two particles of mass m_1 and m_2, moving with velocities $\vec{v}_1$ and $\vec{v}_2$, is illustrated by a velocity vector or Newton diagram such as in Figure 1. Conservation of momentum and energy allow the problem to be separated into two parts, one a particle of mass $M = m_1 + m_2$ traveling at constant velocity, $\vec{v}_{com} = (m_1\vec{v}_1 + m_2\vec{v}_2)/M$, and a particle of mass $\mu = \frac{m_1 m_2}{m_1+m_2}$ of constant energy, $\frac{1}{2}\mu v_{rel}^2$ where $v_{rel} = |\vec{v}_1 - \vec{v}_2|$. An observer traveling with the particle of mass M at velocity $\vec{v}_{com}$ would be in a reference frame of zero momentum, *i.e.*, $m_1\vec{u}_1 = -m_2\vec{u}_2$ where $\vec{u}_i$ is the velocity of particle i in this center of mass reference frame. Within the center of mass frame, calculating the dynamics of the encounter reduces to determining the trajectory of a particle of mass μ moving with initial velocity $\vec{v}_{rel}$ subject to a force field originating at the center of mass. The force field is simply the interparticle potential energy, $U(\vec{r})$, where $\vec{r}$ is the vector connecting the center-of-mass of each particle. In this subsection and the following one, we will consider only those potentials which depend solely on the magnitude of $\vec{r}$, *i.e.*, isotropic potentials.

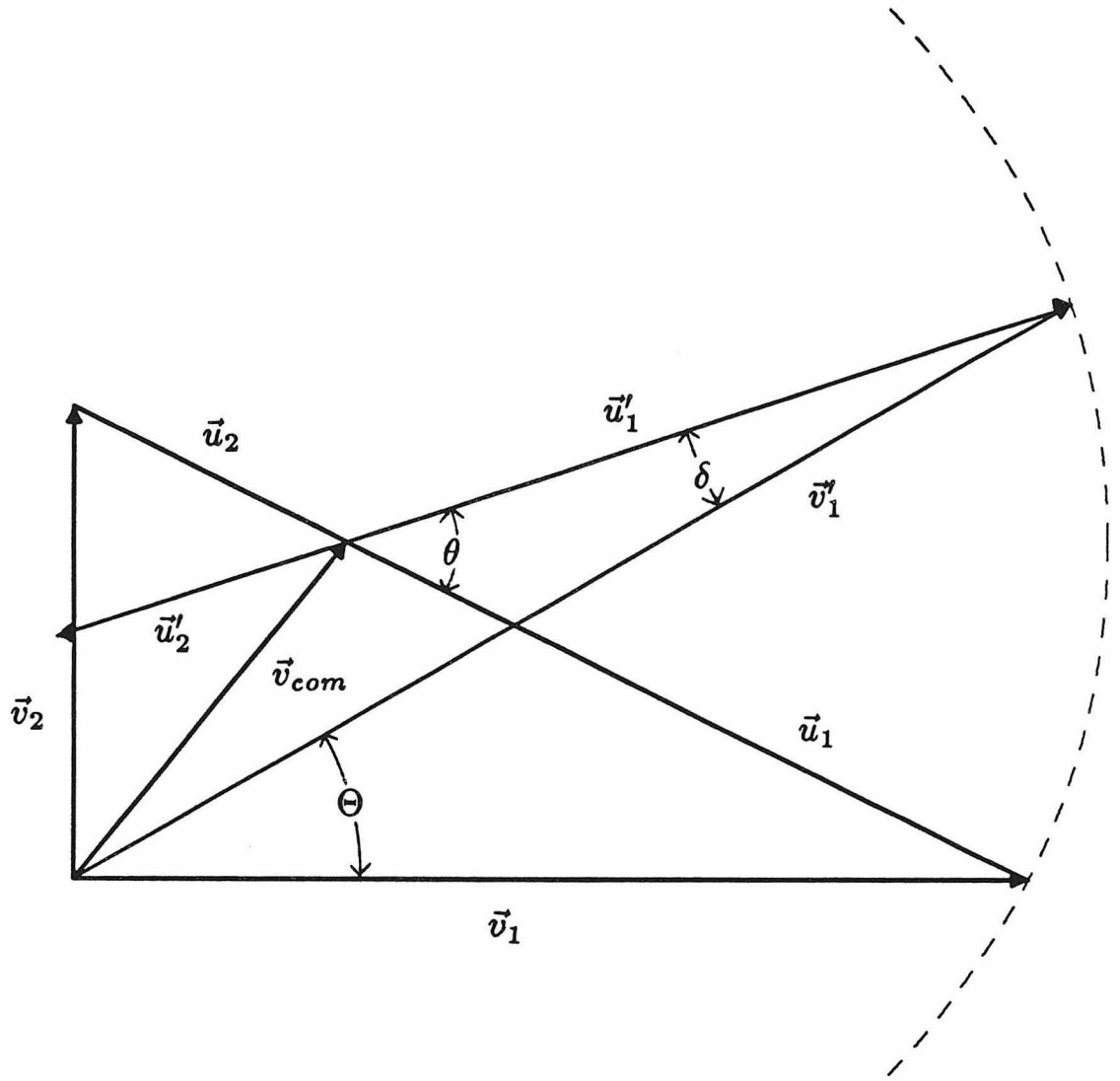

Figure 1. Newton diagram for methane $(m_1, \vec{v}_1)$ scattered from Argon $(m_2, \vec{v}_2)$. The $\vec{v}_i$ are laboratory velocity vectors and the $\vec{u}_i$ are the corresponding center-of-mass velocity vectors. The primes denote the final velocities of the scattered particles. Θ is the laboratory angle which corresponds to scattering through the center-of-mass angle, θ. For elastic scattering, $|\vec{u}'_i| = |\vec{u}_i|$ and the product velocity vectors are constrained to lie on the Newton circle of radius $|\vec{u}_i|$ centered on the tip of the center-of-mass velocity vector $\vec{v}_{com}$. A section of the Newton circle is represented by the dashed arc.

To illustrate some of the terms to be introduced, a one particle trajectory is shown in Figure 2. The deflection angle, χ, is related by simple geometry to the orientation angle, θ_0, of the classical turning point, r_0, by $\chi = \pi - 2\theta_0$. The total energy of the system at any point on the trajectory is just the sum of the kinetic and potential energies:

$$E = \frac{1}{2}\mu\left(\left(\frac{dr}{dt}\right)^2 + r^2\left(\frac{d\theta}{dt}\right)^2\right) + U(r). \tag{1}$$

For a realistic potential energy function ($U(r) \rightarrow 0$ as $r \rightarrow \infty$), the asymptotic value of E at infinite separation is just $\frac{1}{2}\mu v_{rel}^2$. Similarly, the asymptotic value of the angular momentum of the system is $L = \mu v_{rel} b$ where b is the orbital impact parameter defined as the distance of closest approach in the absence of a potential. Conservation of angular momentum allows us to eliminate the θ dependence of Equation (1) by replacing the angular momentum, $L = \mu r^2 \frac{d\theta}{dt}$, with its asymptotic value as in Equation (2).

$$E = \frac{1}{2}\mu\left(\frac{dr}{dt}\right)^2 + \frac{L^2}{2\mu r^2} + U(r) \tag{2}$$

The last two terms of Equation (2) are generally grouped together as an effective potential, $V(L,r)$. The centrifugal term, $\frac{L^2}{2\mu r^2}$, is always repulsive and when coupled with the attractive part of the the potential it has the effect of producing a centrifugal barrier in the effective potential. Thus, if the collision energy is low enough that the classical turning point lies on the centrifugal barrier, then the scattering is very sensitive to the attractive region of the potential. Conversely, when the collision energy is greater than the centrifugal barrier, the repulsive "hard wall" portion of the potential is sampled. Consequently,

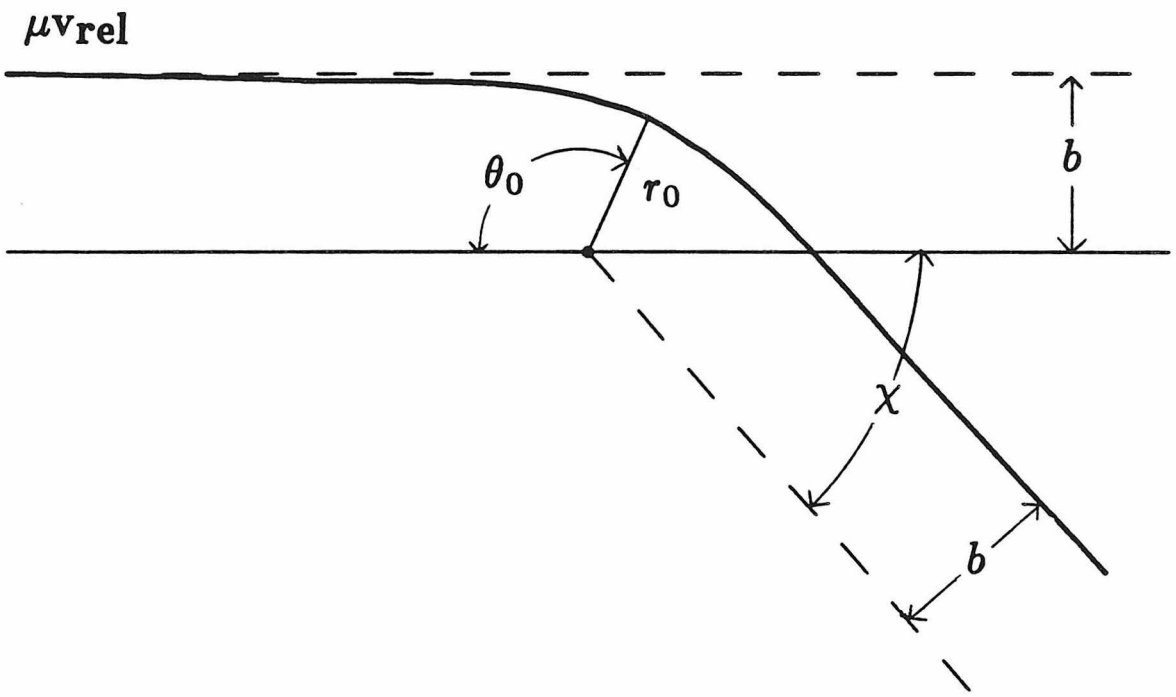

Figure 2. A classical trajectory for a particle of mass μ and initial velocity $\vec{v}_{rel}$ under the influence of a realistic intermolecular potential. b is the orbital impact parameter, r_0 and θ_0 are the distance and orientation angle of the classical turning point (where $\frac{dr}{dt} = 0$), and χ is the deflection angle.

molecular beam elastic scattering experiments can provide detailed information about the complete potential energy surface.

This information can be extracted from the elastic scattering data in the form of the classical deflection function, $\chi(b, v_{rel})$. It can be shown using Equation (2) and other relationships expressed in this text that

$$\chi(b, v_{rel}) = \pi - 2\int_{r_0}^{\infty} \frac{L}{\mu r^2}\left[\frac{2}{\mu}\left(E - \frac{1}{2}\mu v_{rel}^2\frac{b^2}{r^2} - U(r)\right)\right]^{-1/2} dr. \qquad (3)$$

However, this relationship in itself is not sufficient to experimentally determine a potential since it is impossible to select the impact parameter of a collision. Instead, we must look at the contribution to scattering at angle $\theta = |\chi|$ from all values of b. The quantity of interest then is the differential cross section which is defined as

$$\frac{d\sigma}{d\omega}(\theta, E) = \frac{\#\ of\ scattered\ particles/unit\ time/unit\ solid\ angle}{\#\ of\ incident\ particles/unit\ time/unit\ area}, \qquad (4)$$

or in this case,

$$\frac{d\sigma}{d\omega}(\theta, E) = \sum \left|\frac{b}{sin\chi(d\chi/db)}\right|, \qquad (5)$$

where the summation is over all values of b that can lead to scattering into the same angle. An important feature of the classical differential cross section is its inverse dependence on $sin\chi$ and $d\chi/db$. At values of χ where either of those quantities are zero there will be a singularity in the differential cross section. Those places where $sin\chi = 0$ are responsible for the "glory effect," the principal manifestation of which is the glory oscillations in measurements of the energy dependence of the integral cross section. More relevant to our studies is the angle

χ_r at which $d\chi/db = 0$. At this angle, many values of b project onto the same value of χ leading to infinite intensity at that angle. Thus, the angle χ_r is called the rainbow angle because of the analogy to the optical rainbow caused by the turning point in the internal reflection of light rays in water droplets. The value of the rainbow angle is inversely proportional to the reduced collision energy, $E^* = \frac{1}{2}\mu {v_{rel}}^2/\epsilon$, where ϵ is the well depth of the potential. Thus, if the collision energy is known, the well depth of the potential can be determined from the rainbow angle.

In practice, the rainbow effect does not lead to a singularity in the differential cross section but merely a broad area of enhanced intensity. This is partially a consequence of the Heisenberg uncertainty principle since it is impossible to determine both the impact parameter and the deflection angle to an accuracy of better than $\Delta b \Delta\chi \geq \hbar/\mu v_{rel}$. Principally, however, the failure of classical mechanics arises from the summation over intensities resulting from multiple trajectories as in Equation (5). These multiple trajectories lead to interference effects in the form of oscillatory features, superimposed on the classical differential cross section, which can only be explained in a quantum mechanical treatment.

1.2.2 Quantum Theory of Elastic Scattering: Isotropic Potentials

The quantum mechanical approach begins, as in the classical treatment, with the separation of the problem into a particle of mass M moving with a constant velocity $\vec{v}_{com}$ and a particle of mass μ with initial velocity $\vec{v}_{rel}$. The

center of mass motion can be disregarded (until we wish to compare calculations with experiment) and the problem is then reduced to one particle of mass μ interacting with a central potential. However, instead of having a well defined trajectory described by $\vec{r}(t)$ and $\vec{p}(t)$ as in the classical approach, we have only a wavefunction $\Psi(\vec{r},t)$ with its associated expectation values.

As in all quantum mechanical problems, this treatment begins with the Schrödinger equation,

$$\frac{-\hbar^2}{2\mu}\nabla^2\Psi(\vec{r},t) + U(r)\Psi(\vec{r},t) = i\hbar\frac{\partial}{\partial t}\Psi(\vec{r},t). \tag{6}$$

Since the Hamiltonian does not explicitly depend on time, *i.e.*, the potential is invariant in that coordinate, the wavefunction for a monoenergetic beam can be assumed to be of the form $\Psi(\vec{r},t) = \Psi_k(\vec{r})e^{-iEt/\hbar}$. Substitution of this relationship into Equation (6) yields the time-independent Schrödinger equation which is presented in Equation (7), rearranged to a more convenient form.

$$\left[\nabla^2 - \frac{2\mu}{\hbar^2}U(r) + k^2\right]\Psi_k(\vec{r}) = 0\ , \tag{7}$$

where $k = \mu v_{rel}/\hbar$. In a field free space, *i.e.*, $U(r) = 0$, the most general solution of this equation is a plane wave, *i.e.*,

$$\Psi_k(\vec{r}) = e^{i(\vec{k}\cdot\vec{r})}. \tag{8}$$

Thus, we would expect that the asymptotic behavior of the wavefunction of Equation (7) would be an incoming plane wave coupled with an outgoing radial

wave centered on the origin with an amplitude that varies with angle. The total wavefunction can then be represented:

$$\Psi_k(\vec{r}) = e^{i(\vec{k}\cdot\vec{r})} + \frac{e^{ikr}}{r} f(\theta) = \Psi_p + \Psi_s, \qquad r \to \infty \tag{9}$$

where $f(\theta)$ is called the scattering amplitude, and the r^{-1} factor accounts for the necessary r^{-2} decrease in intensity with increasing r to conserve flux. The particle flux density of the incoming wave is

$$j_p = \frac{\hbar}{2i\mu}\left(\Psi_p^*\nabla\Psi_p - \Psi_p\nabla\Psi_p^*\right) = \frac{\hbar k}{\mu} = v_{rel}, \tag{10}$$

and similarly the particle flux density of the scattered wave is

$$j_s = \frac{\hbar k}{\mu r^2}|f(\theta)|^2. \tag{11}$$

Now, since the differential cross section is defined as in Equation (4) of Section 1.2.1, the quantum mechanical differential cross section becomes

$$\frac{d\sigma}{d\omega} = |f(\theta)|^2. \tag{12}$$

Thus, to obtain the differential cross section we need only solve Equation (7) for the scattering amplitude.

This task is not as formidable as it would seem since Equation (7) is a one particle, central force problem (somewhat analogous to the well documented one electron atom problem). In the central force problem it is useful to separate the wavefunction into its radial and angular parts. Beginning with the incoming plane wave, the wavefunction can be written,

$$\Psi_p(r,\theta) = R(r)\Theta(\theta)\ , \tag{13}$$

where the $\Theta(\theta)$ are the Legendre polynomials, $P_l(cos\theta)$, and $R(r)$ is a solution of

$$\left\{ \frac{1}{r^2} \frac{d}{dr}(r^2 \frac{d}{dr}) - \frac{l(l+1)}{r^2} + k^2 \right\} R(r) = 0. \tag{14}$$

Solutions to Equation (14) are called the spherical Bessel functions, $j_l(kr)$. The asymptotic value of the spherical Bessel functions is found by neglecting terms which vanish more rapidly than r^{-1}, and is found to be:

$$j_l(kr) \rightarrow \frac{sin(kr - l\pi/2)}{kr}, \qquad r \rightarrow \infty. \tag{15}$$

Now, combining $R(r)$ and $\Theta(\theta)$ we have

$$\Psi_{p,l}(r,\theta) = j_l P_l(cos\theta), \tag{16}$$

and in general

$$\Psi_p(r,\theta) = e^{i\vec{k}\cdot\vec{r}} = \sum_{l=0}^{\infty} c_l j_l(kr) P_l(cos\theta). \tag{17}$$

The c_l are constants whose values can be found by multiplying both sides of Equation (17) by $P_l(cos\theta)dcos\theta$ and integrating. The c_l are found to be equal to $(2l+1)i^l$, and therefore

$$\Psi_p(r,\theta) = \sum_{l=0}^{\infty} (2l+1) i^l j_l(kr) P_l(cos\theta). \tag{18}$$

A similar solution can be found for Equation (9) using the same means. Since the potential is dependent only on r, the angular function is once again equal to the Legendre polynomials. At large r, the potential vanishes and the solution of the radial equation must be similar to the Bessel functions. In particular, the radial part of the total wavefunction is

$$R_l(kr) \rightarrow \frac{sin(kr - l\pi/2 + \eta_l)}{kr}, \qquad r \rightarrow \infty \tag{19}$$

where the η_l are called the phase shifts (for obvious reasons). Thus, the partial wave expansions of Ψ_p and $\Psi_p + \Psi_s$ can be substituted into Equation (9) to solve for $f(\theta)$. The scattering amplitude is then found to be

$$f(\theta) = \frac{1}{2ik} \sum_{l=0}^{\infty} (2l+1)(e^{2i\eta_l} - 1) P_l(cos\theta). \tag{20}$$

The differential cross section resulting from a given potential is then completely determined by k and the η_l. The η_l are determined by solving the radial equation for each value of l. For the systems of interest here, several hundred η_l contribute significantly to the differential cross section and solving the radial equation for all those values of l would be very time consuming. In order to increase computing efficiency, the phase shifts are usually calculated using the semi-classical JWKB approximation.[23] Phase shifts calculated in this manner have been found to be accurate for most systems to within about 0.1%.[24]

Having determined the phase shifts, let us turn our attention to the qualitative aspects of the semi-classical scattering in the vicinity of the rainbow. As in the classical case, the intensity measured at some angles results from several values of l (b in the classical treatment) and is therefore related to the sum of the scattering amplitudes for all contributing values of l in equation (20). Figure 3 shows the relationship between χ, η and l for the argon-methane potential of Chapter 2. It can be seen from Figure 3 that for $|\chi| < |\chi_r|$, three values of l contribute to the intensity at θ, *i.e.*,

$$f(\theta) = f_a(\theta) + f_b(\theta) + f_c(\theta). \tag{21}$$

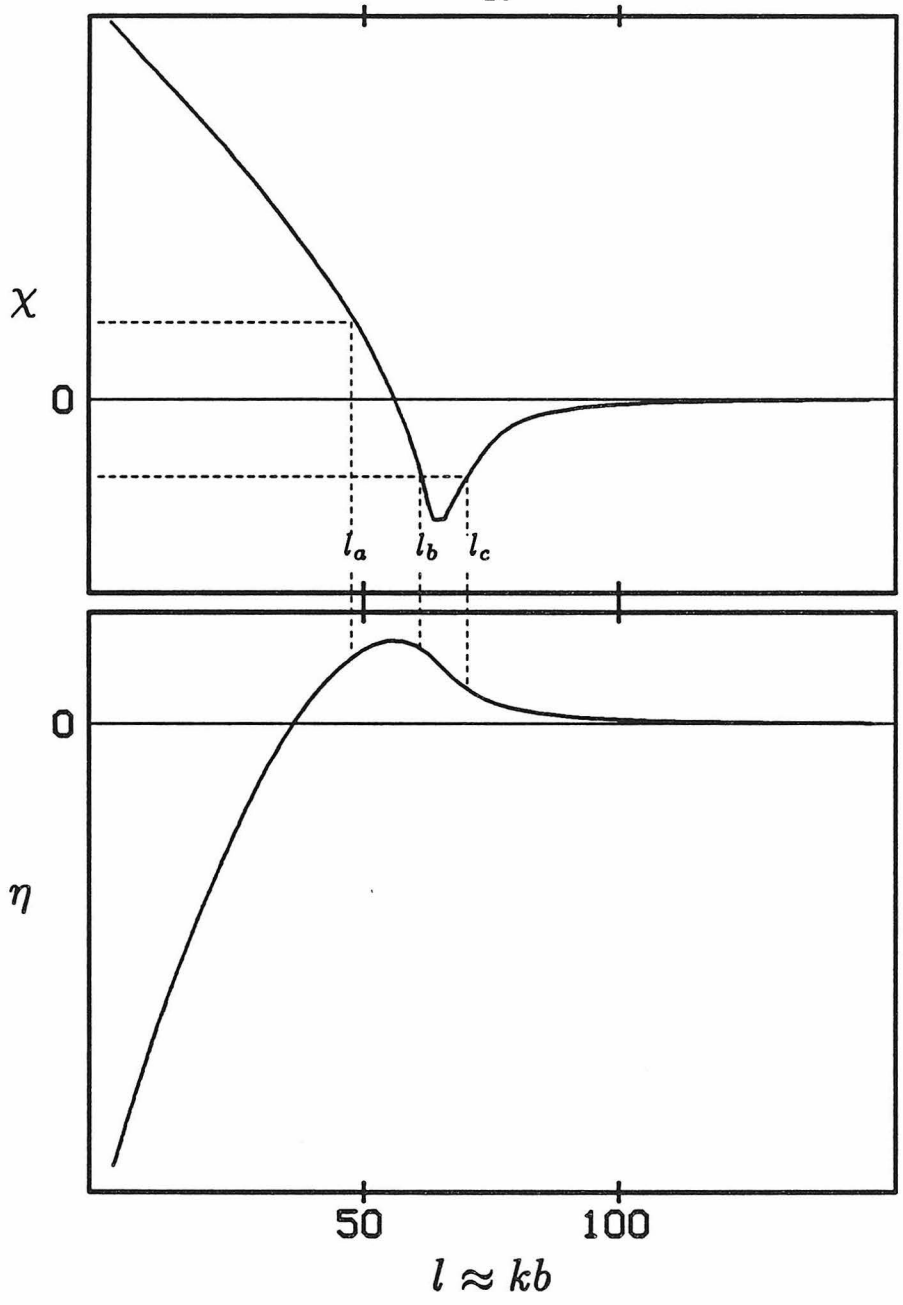

Figure 3. The phase shifts, η, resulting from the argon-methane potential of Chapter 2 and a collision energy of 400 K are shown as a function of the angular momentum quantum number, l. The semi-classical deflection function, χ, calculated from $\eta(l)$ is also shown to illustrate that several values of l can contribute to the scattering amplitude at an angle $\theta = |\chi|$.

The differential cross section, however, is equal to $|f(\theta)|^2$ and thus there are cross (or interference) terms in the differential cross section.

By using the stationary phase approximation[5] to solve for the scattering amplitudes, it can be shown that

$$f_b(\theta) + f_c(\theta) \approx \frac{1}{k}\left(\frac{2\pi l_r}{sin\chi}\right)^{1/2} \frac{Ai(x)}{q^{1/3}} e^{i\delta_r} \ , \tag{22}$$

where $Ai(x)$ is the Airy function,[25] $x = (\chi - \chi_r)q^{-1/3}$, $q = (\partial^2\chi/\partial l^2)_{l=l_r}$, and $\delta_r = 2\eta_r + l_r\chi - 3\pi/4$. The Airy function has the effect of producing a broad oscillatory behavior in the differential cross section. The maxima of the oscillations are called the "rainbow maxima." The actual rainbow angle is the outermost inflection point in the Airy function, occuring just beyond the first or "primary rainbow maximum." The maxima at lower angles are called the "supernumerary rainbow maxima." These features are strongly correlated to the attractive region of the potential and can provide information about the well depth, shape and to some extent the range of the potential.

When the contribution from $f_a(\theta)$ is taken into account it is found that a higher frequency oscillation is superimposed on the rainbow structure. These rapid or diffraction oscillations have a period[4]

$$\Delta\chi = \frac{2\pi}{(l_r + l_a)} \approx \frac{2\pi}{k(b_r + b_a)}. \tag{23}$$

Since the impact parameters, b, are related to the radius of the potential, the period of the oscillations is inversely proportional to the diameter of interaction.

Thus, experimentally observed quantum oscillations and rainbow maxima are so sensitive to the potential that the differential cross section can be inverted

to determine the potential.[26–28] Although we resolved those features in most of our differential cross sections, we could not use inversion procedures as they are only applicable to spherically symmetric potentials.[28] However, those features remain sensitive tools for elucidating the potential surface.

1.2.3 Anisotropic Potentials

For intermolecular potentials which depend not only on the intermolecular separation but also on the relative orientation of the molecules, such as those examined in Chapters 2 and 3 of this thesis, the problem of calculating cross sections is inherently more complicated. The potential is no longer only a function of internuclear separation, but also a function of the orientation of the molecules. In addition, those collisions which induce a transfer of energy to (or from) the internal modes of the molecule must be considered. To completely elucidate the potential energy surface, one would normally need to measure state-to-state differential cross sections for inelastic scattering.[29] Even with this detailed information, elaborate computer intensive calculations are required to determine the potential. Fortunately, approximate techniques have been developed which allow analysis of the total differential cross section (elastic plus inelastic) which is determined in the same manner as the elastic differential cross sections discussed in the previous sections. The most common of these techniques is the infinite order sudden approximation which we have used to analyze the rare gas-halogen potentials of Chapter 3. The infinite order sudden approximation will be breifly outlined in the following paragraphs. The reader is referred to several excellent articles[13,30] and texts[4,5,31] for more detailed information.

Consider the scattering of a closed shell atom, A, by a diatomic molecule, BC, as shown in Figure 4. To completely describe the scattering we must solve the Schrödinger equation,

$$E\Psi = \left\{ \frac{-\hbar^2}{2\mu r} \frac{d^2}{dr^2} r + \frac{L^2}{2\mu r^2} + H_{BC} + U(r, R, \gamma) \right\} \Psi \ , \tag{24}$$

where L is the angular momentum operator of the atom relative to the diatomic, $U(r, R, \gamma)$ is the orientation dependent potential energy function with the coordinates described as in Figure 4, and H_{BC} is the Hamiltonian of the isolated diatomic molecule,

$$H_{BC} = \frac{-\hbar^2}{2\mu_{BC} R} \frac{d^2}{dR^2} R + \frac{J^2}{2\mu_{BC} R^2} + U_{BC}(R) \ , \tag{25}$$

where J is the molecular orbital angular momentum operator. In this approximation, we simplify the Hamiltonian, by replacing the angular momentum operators with their eigenvalue forms, *i.e.*, $L^2 = \hbar^2 \bar{l}(\bar{l}+1)$ and $J^2 = \hbar^2 \bar{j}(\bar{j}+1)$ where $\bar{l}$, $\bar{j}$ denote an average quantum number of the initial and final states.

The substitution of the eigenvalue form of L into equation (24) is known as the centrifugal sudden approximation. It is expected to be a valid approximation when the relative kinetic energy is sufficiently large that the precise value of the centrifugal potential is unimportant. If the scattering is dominated by the repulsive "hard wall" of the potential, then the classical turning point (where the relative kinetic energy is a minimum) is virtually independent of the value of l and the above condition is satisfied. Kouri *et al.*[32] have determined a useful energy criterion for sufficiency of the approximation. The criterion is that the relative kinetic energy for both the initial and inelastically scattered particles

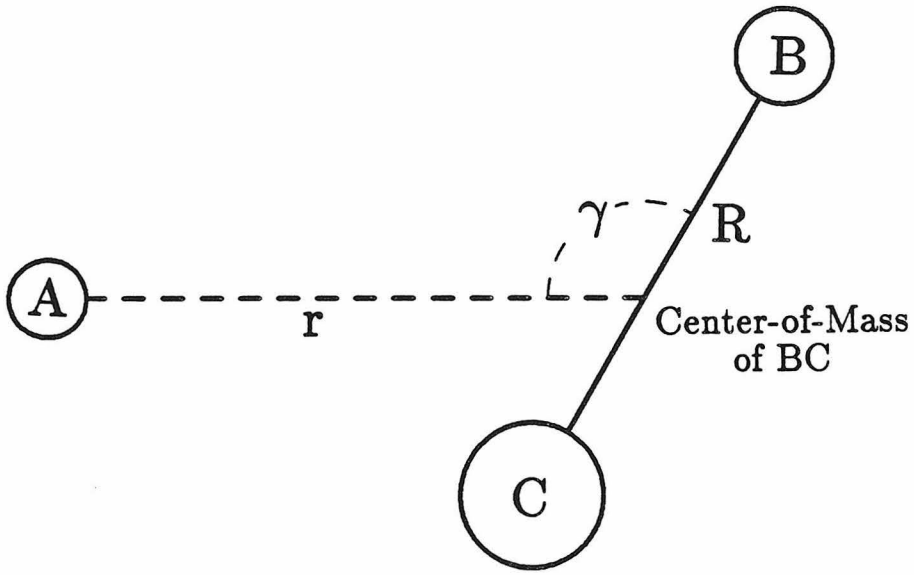

Figure 4. Pictorial representation of the coordinates of an atom-diatom interaction. R is bond length of the molecule BC, r is the distance between A and the center-of-mass of BC, and γ is the relative orientation angle between $\vec{R}$ and $\vec{r}$.

be greater than the well depth of the potential. This condition assures that there is no scattering from a centrifugal barrier in either the entrance or exit channels (the classical turning point varies rapidly with l for scattering from the centrifugal barrier).

The substitution of the eigenvalue form of J in Equation (25) is known as the energy sudden approximation. The energy sudden approximation is considered valid when the relative velocity of the atom with respect to the molecule is much greater than the velocity of the atoms within the molecule, *e.g.*, the rotational velocity. The validity constraint has actually been quantified by Top and Kouri[33] who found the approximation good if

$$\left(\frac{2\mu B_e}{\mu_{BC}}\right)^{1/2} \frac{|[j(j+1)]^{1/2} - [j'(j'+1)]^{1/2}|}{[2E - B_e(j(j+1) + j'(j'+1))]^{1/2}} < 1 \ , \tag{26}$$

where B_e is the rotational constant of the diatomic. It is evident from Equation (24) that this approximation is more useful for light atoms (small μ) scattered by heavy molecules (large μ_{bc}) with small rotational constants.

When both the energy sudden and the centrifugal sudden approximation are used together, the resulting analysis is called the infinite order sudden (IOS) approximation. The name "infinite order" derives from the fact that the equations that result from the IOS approximation include the effects of all terms of the potential to all orders, *i.e.*, no approximation has been made to the potential. The end result of using these approximations is that all of the operators that depend on the angle γ have been removed and γ only appears in Equation (24) as a parameter. If we also pick $\bar{l}$ to be the initial value, which

accounts well for the large elastic contribution, then Equation (24) can be solved for fixed γ with the resulting scattering amplitudes projected for all γ. Using these approximations the total differential cross section can be shown to be

$$I(v' \leftarrow v, \theta) = \frac{1}{2} \int_{-1}^{1} I(v' \leftarrow v, \gamma, \theta) dcos\gamma \ , \tag{27}$$

where $I(v' \leftarrow v, \gamma, \theta)$ is the just the differential cross section for vibrationally inelastic scattering from an isotropic potential. If, as in the experiments in Chapter 3, the relative kinetic energy is insufficient to "open" the vibrational excitation channels, the diatomic molecule can be approximated as a rigid rotor and Equation (27) reduces to

$$I(\theta) = \frac{1}{2} \int_{-1}^{1} I(\gamma, \theta) dcos\gamma. \tag{28}$$

Thus, the total differential cross section can be determined by calculating the differential cross section for an isotropic potential at fixed γ and performing a numerical integration over all values of γ.

1.3 The Crossed Beams Apparatus

In order to perform elastic scattering exeriments, it is necessary to have:

1) a means of producing a collision between two particles with a well defined initial relative velocity, $\vec{v}_{rel} = \vec{v}_1 - \vec{v}_2$ (see Figure 1 in Section 1.2.1),
2) a means of determining the angular distribution of the scattered molecules and of differentiating between the two molecules when detected, and
3) a means of assuring that there will be no collisions with other atoms or molecules after the collision of interest.

These requirements can be fulfilled by having:

1) two well collimated molecular beams whose dimensions and speed distributions are well characterized,
2) a detector which rotates with respect to the molecular beams and incorporates a mass filtering device, and
3) the beam sources, collision region and detector within a vacuum enclosure.

One versatile implementation which accounts for the criterion listed above is the universal crossed beams apparatus of Lee *et al.*[34] We have constructed a high resolution version of that apparatus which is nearly identical to the version described extensively by Sparks.[35] Essentially, the apparatus as shown in Figure 5 consists of two supersonic beam sources which are fixed in orientation relative to the main vacuum chamber, and a quadrupole mass spectrometer detector which rotates about the intersection point of the two beams (these two facets will be described in turn in the following paragraphs).

The supersonic molecular beams[36] are formed by the expansion of high pressure gas from a stagnation region through a small ($\sim 75\mu$m) aperture into a vacuum chamber. During the expansion, the gas is adiabatically cooled to very low temperatures (≤ 10 K) with the heat being converted into directional flow. The speed of the directional flow is

$$v_{ss} = \left(\frac{2}{m} \int_{T_f}^{T_i} C_p dt \right)^{1/2}, \tag{29}$$

where m is the mass of the gas, C_p is its constant pressure heat capacity, T_i is the temperature of the gas within the stagnation region and T_f the temperature of

Figure 5. Cross section through the universal crossed beams apparatus.

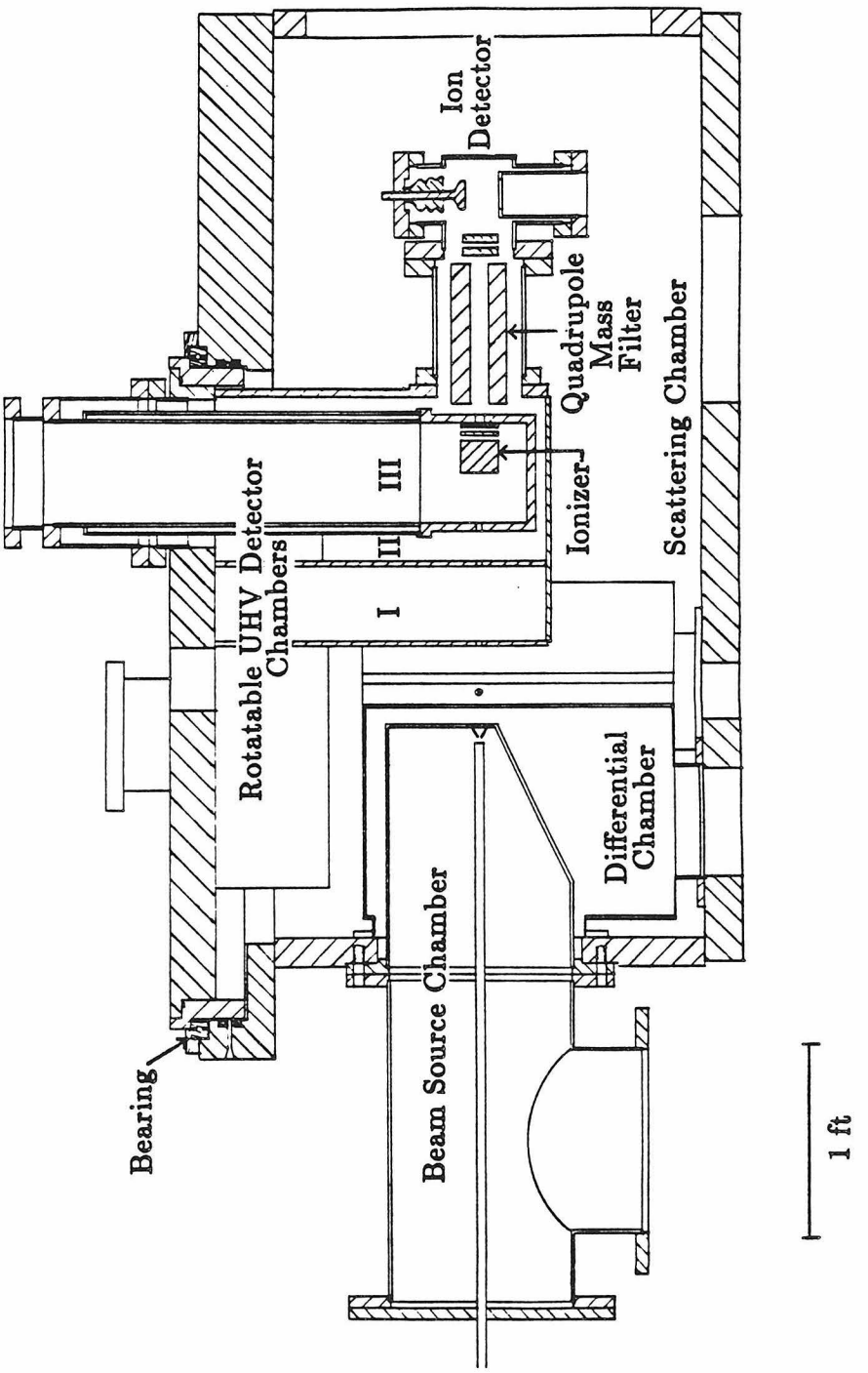
Ion Detector
Quadrupole Mass Filter
Scattering Chamber
Ionizer
III
II
I
Rotatable UHV Detector Chambers
Differential Chamber
Beam Source Chamber
Bearing
1 ft

the molecules within the beam. For a rare gas beam, $C_p = 5R/2$ and Equation (29) reduces to

$$v_{ss} = \left(\frac{5R(T_i - T_f)}{m} \right)^{1/2} . \tag{30}$$

The distribution of speeds about the flow speed in the beam is described well by the Maxwell distribution for the temperature T_f. Thus the speed distribution of the beam is found to be

$$P(v) \propto v^2 e^{-\beta(v - v_{ss})^2} , \tag{31}$$

where $\beta = m/2RT_f$. The quantity, $s = v_{ss}\beta^{1/2}$, is a dimensionless number known as the speed ratio (of the flow velocity to average relative velocity in the flow). Typical speed ratios range from about 7 for neat beams of polyatomics to 20 or more for rare gases. The flow velocity and speed ratio of the beams are determined experimentally using the time-of-flight (TOF) technique. In this technique, a rotating wheel with a narrow slit is placed in front of the detector. As the slit passes the detector aperture, a sample of the beam is allowed to pass into the detector opening and the time profile of the sample is detected downstream. The time distribution can then be converted to a speed distribution using the proper Jacobian, $|dv/dt| = (v^2/L)$ (L is the flight length) and the parameters of Equation (31) determined by a least squares fit. The program used to fit the distributions along with a much more detailed account of the TOF technique have been presented elsewhere.[37]

An interesting aspect of Equation (30) is that by varying the beam source stagnation temperature, one can adjust the velocity of the beams and select

the relative kinetic energy of the encounter. We have taken advantage of this relationship by employing liquid nitrogen cooled beam sources to:

1) displace the rainbow to higher angles and increase the period of the diffraction oscillations by lowering the collision energy, and
2) record differential cross sections at several energies thereby increasing the uniqueness of the derived potential.

The temperature of the stagnation region was controlled to $\pm .5°C$ by a thermocouple temperature controller coupled to resistive heaters clamped to the bottom of the copper block which defined the stagnation region. A cross section of the beam source is shown in Figure 6. By varying the composition or length of the threaded rods, any desired thermal conductance can be realized. This makes the beam source operable from 77 K to above 300 K.

The direction of the beams is predetermined by aligning the beam source apertures along axes defined by scribe marks on the main vacuum chamber. These scribe marks are located on the beam ports which have been precision machined such that the beam axes are perpendicular and intersect each other within 75 μm. The beams are spatially defined by a skimmer as they pass into a differential pumping region and then by a rectangular collimating aperture as they enter the scattering chamber. The intersection of the two beams defines a parallelepiped whose sides are typically about 2 to 4 mm. The scattering chamber is kept at $< 10^{-7}$ torr (1 torr = 1 mm Hg) at which pressure collisions with moleucles other than those in the other beam are infrequent (the mean free path for air at this pressure at room temperature is approximately 3 km).

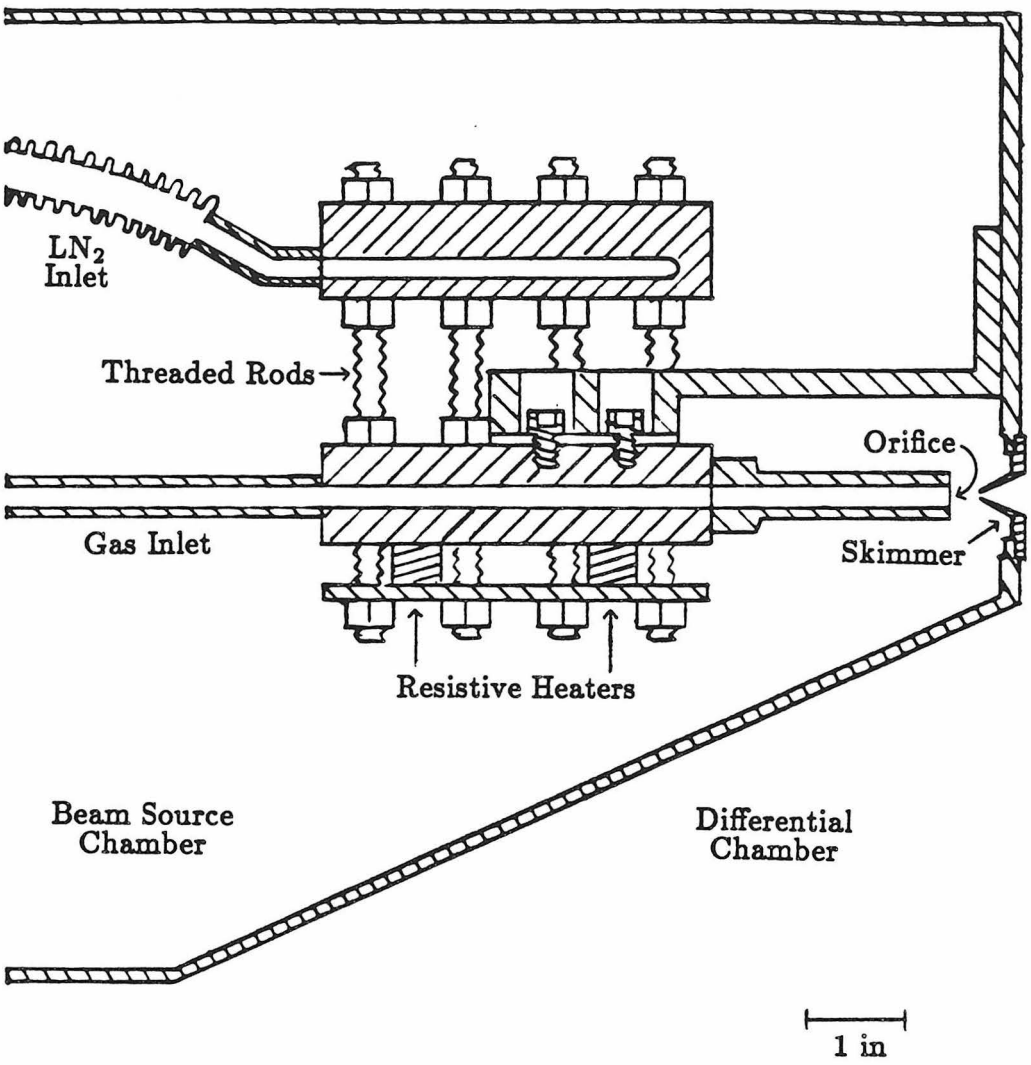

Figure 6. Cross section of the liquid nitrogen cooled, temperature controlled beam source. Cooling is provided by a liquid nitrogen reservoir in the upper copper block. The beam stagnation region is cooled by thermal conductance through the threaded rods. A temperature controller monitors the stagnation temperature via a thermocouple and regulates the temperature by controlling the current through the resistive heaters clamped to the bottom of the stagnation region.

Thus, we have accounted for the first and third conditions presented originally and now we turn our attention to the rotatable detector. The detector chamber rests on a large diameter (35 inch) bearing and is rotatable using a chain and sprocket assembly. The angular positioning is repeatable to less than 5 minutes. The bearing is mounted in a precision machined diameter on the main vacuum chamber. That diameter is parallel to the plane defined by the two beams and its axis intersects the two beam axes within 75 μm. The detector vacuum housing consists of three ultra high vacuum (UHV) chambers (I, II and III in Figure 5) which provide the necessary low pressure conditions required for particle detection. The construction process and the geometries of these three chambers have been significantly altered from the original design of Sparks[35] to increase the pumping speed in regions I and II and to obviate the necessity of purchasing special order ion pumps. In the present design the three Perkin-Elmer 220 ls^{-1} ion pumps can fit directly over their respective regions significantly increasing their effective pumping speed in the aperture region. The same care was used in selecting only UHV compatible materials as was espoused by Sparks, but to avoid the need for vacuum brazing, we used some external welds.

A schematic of the detection system is shown in Figure 7. It consists of an electron impact ionizer, a quadrupole mass spectrometer and an ion detector. The ionizer, based on the design by Brink[38] consists of a thoriated tungsten filament between an electron reflecting shield and a cylindrical grid held at a positive voltage (200 V). The electrons emitted by the filament (2 to 8 mA) are accelerated into the volume defined by the grid where they oscillate many times

Figure 7. Schematic of the universal particle detection system as described in the text. Modulation signals from the 150 Hz tuning fork chopper are processed by the timing-gating module which uses the processed signal to alternately gate the two CAMAC scalers.

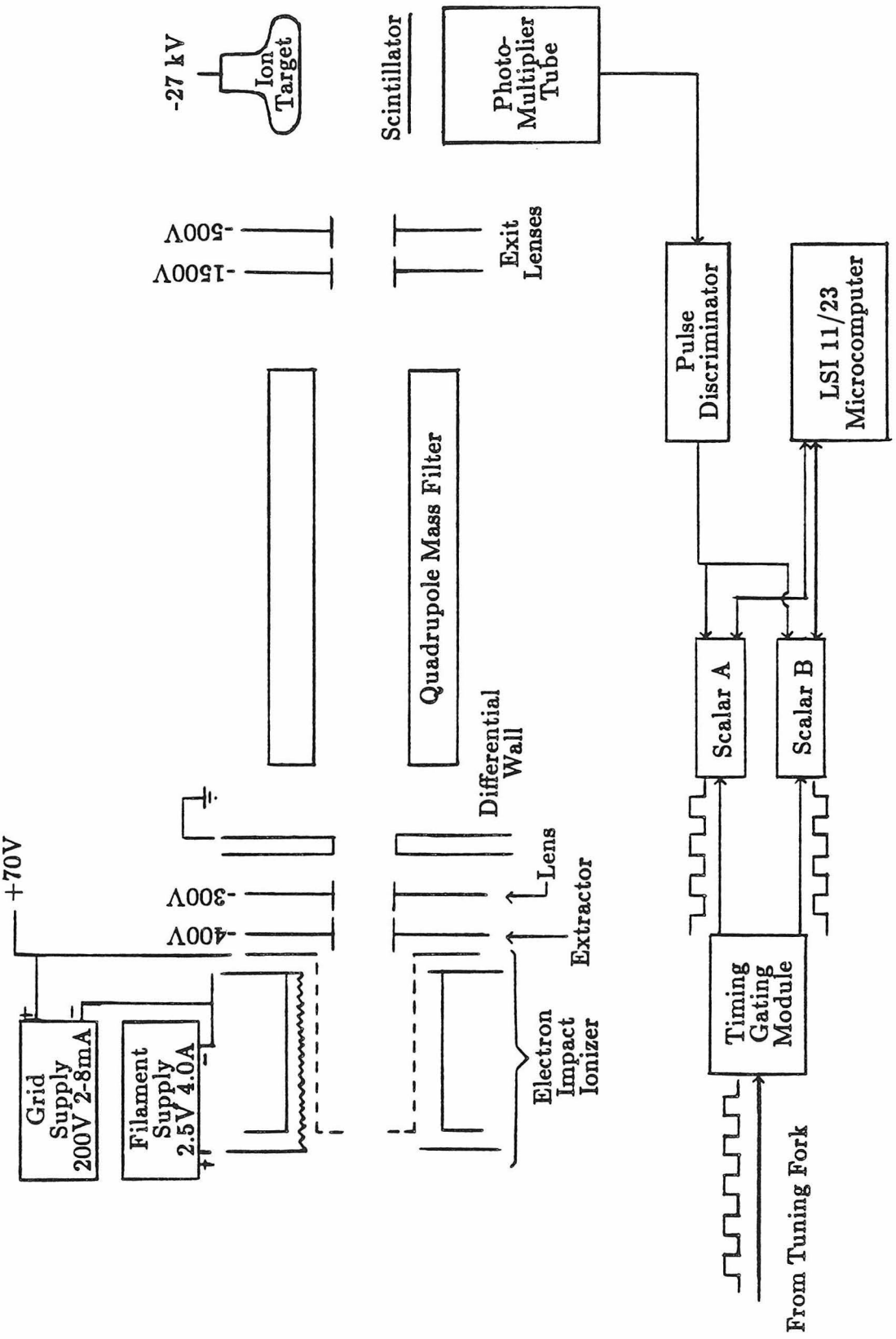
-27 kV
Ion Target
Scintillator
Photo-Multiplier Tube
-500V
-1500V
Exit Lenses
Pulse Discriminator
LSI 11/23 Microcomputer
Quadrupole Mass Filter
Differential Wall
+70V
-300V
-400V
Lens
Extractor
Electron Impact Ionizer
Grid Supply 200V 2-8mA
Filament Supply 2.5V 4.0A
Scalar A
Scalar B
Timing Gating Module
From Tuning Fork

before striking the grid and being collected. The grid itself would normally have been taken from an electron tube, however, with the passing of the "electron tube era" it was impossible to find a suitable grid and one had to be constructed. The ionizer is situated such that the product beam passes through the ionizer and the electric field of the electrons. A small fraction of the beam is ionized and the ions drawn out of the ionizer by an extracting lens located downstream. The ions are accelerated by the potential difference between the grid (which floats at +70 V above ground) and the differential vacuum chamber wall and are then focused before entering the Extranuclear Laboratories quadrupole mass filter. The quadrupole ejects all ions except those with the selected mass-to-charge ratio leaving only the species of interest. Upon leaving the quadrupole, the ions are once again focused and pass into the Daly type ion detector.[39] In the ion detector, the ions are accelerated transverse to the beam axis by an aluminum coated electrode held at -27 kV. As the ions strike the electrode they eject 6 to 8 electons which are accelerated in the -27 kV field and strike an aluminum coated plastic scintillator (the aluminum coating reduces stray light and prevents sublimation of the scintillator material while still transmitting the electrons and providing electrical conductivity). The scintillator produces 3 to 6 photons per incident electron and the photons are detected by an external photomultiplier. Pulses from the photomultiplier are then discriminated to eliminate the single photon event (from stray light and dark current) before being counted. The actual counting procedure and hardware will be discussed in the next section.

1.4 Experimental Method and Analysis

Now that both the theoretical aspects of elastic (and inelastic) scattering and the apparatus used to measure scattering intensities have been discussed, all that remains is the actual measurement of the laboratory differential cross section and its use to determine the intermolecular potential. In this section the method of measurement is reported (Subsection 1.4.1) and the procedure for determination of the potential from the laboratory differential cross section is examined (Subsection 1.4.2).

1.4.1 Determination of Laboratory Angular Distributions

The measurement of the laboratory angular distribution involves many factors. For instance, at each collision energy:

1) the speed distribution of each beam must be determined and optimized,
2) the directional quality of each beam must be verified,
3) the angular distribution is measured while accounting for any possible drift in detection sensitivity, and also for any angle dependent background, and
4) some estimation of the uncertainty in each data point must be made.

The determination of the magnitude of the beam velocities and the distribution of those velocities was done using the time-of-flight technique discussed in the previous section. An attempt was made to optimize the beam velocity distributions, *i.e.*, make them narrower, by increasing the stagnation pressure of the precursor gas. Two factors limited the ultimate distribution that could be achieved. At some pressure, p_{tp}, the throughput of the nozzle would become so great that the beam source chamber vacuum pumps would "choke," of

course this effect could be eliminated by going to a smaller beam orifice diameter, but since the throughput is proportinal to $d^4_{orifice}p^2$,[40] a fractional change, $\frac{1}{x}$, in the orifice diameter would have to be followed by a x^2 increase in pressure to maintain the same throughput and, to a first approximation, the beam intensity. Since we wanted to operate the low temperature nozzles close to the condensation point of methane (at 1 atmosphere), high pressures were not desirable, and since we wanted to maintain maximum throughput, the nozzles were constructed with 75 μm orifices that could not be varied. The second limiting factor was a necessity to minimize cluster formation in the beam expansion. The presence of clusters in the beam is undesirable since it will degrade the measured angular distributions. The stagnation pressure was adjusted upward until at some pressure, p_c, the dimer signal was .25% of the monomer signal. The final pressure used was just the lesser of p_{tp} and p_c.

The directional quality of the beams was verified by scanning through the beams with a small pinhole placed in front of the detector. Each beam was found to be within a quarter of a degree of its nominal position. In addition, the assumed beam velocities (both magnitude and direction) were checked by measuring the laboratory scattering distribution for neon-methane on either side of the primary beam and transforming those distributions to the center-of-mass, using the assumed velocities, and comparing the results. The two differential cross sections are shown in Figure 8 and can be seen to be equivalent within the accuracy of the measurement. By this method, it can be postulated that the

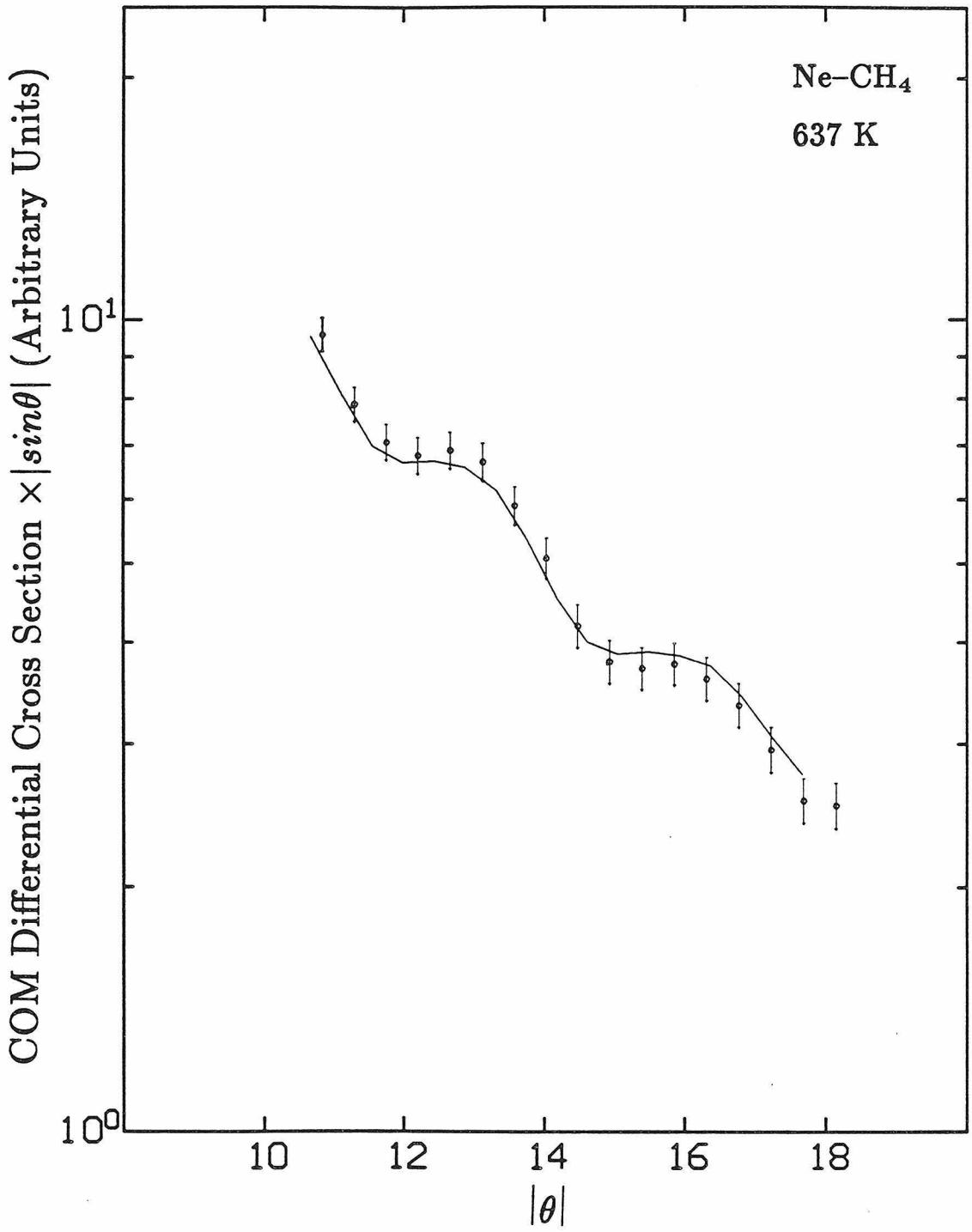

Figure 8. Center-of-mass differential cross sections measured at $-\theta$ (—) and θ (○). The error bars represent the sum of the estimated errors in both measurements. The cross sections have been scaled by the $|sin\theta|$ to enhance the diffraction oscillations.

cumulative error in the laboratory to center-of-mass transformation is less than a quarter of a degree (the distance between successive points).

The scattered intensity at any given angle was measured by detecting the total counts at that angle for a given period of time and subtracting the background counts (by blocking the target beam) for an equal amount of time. This was done automatically by modulating the target beam at 150 Hz with a tuning fork chopper. When the chopper blocked the beam, only ambient background from the primary beam source was detected, and when the chopper swung out of the beam, both background and the scattered signal could be detected. This technique allows the background counts to be unambiguously subtracted out of the total counts leaving only the scattered signal. The total counts for each of these two channels (opened and closed) were accumulated by two CAMAC scalars which were gated synchronously to the tuning fork chopper. The CAMAC modules were interfaced to a laboratory microcomputer which read the data from the scalers and performed all manipulations on the raw data.

To obtain an angular distribution, a reference angle was selected (usually 10°) and then the other angles were scanned while periodically returning to the reference angle. The intermediate angles were then normalized to the reference angles and scaled to reflect any drift in the reference intensity. While this may seem like a crude method for accounting for changes in the beam intensities or detector sensitivies, etc., there was no obvious method which was any less ambiguous for accounting for the drift. In normal operation, the reference intensity drifted by only small amounts (1-2%) and the approximation was

probably adequate. Each angle was measured several (4 to 8) times and any anomolously low or high values were investigated. The values for each angle were then averaged with the averaged values being those used in Chapters 2 and 3.

The estimated uncertainties in the averaged values were calculated in two ways. When counting large numbers of pulses, the theoretical standard deviation of the final number counted is the square root of that number. Since each datum was determined by the difference between two large numbers of counts, the standard deviation of each datum is expected to be the square root of the sum of the two large numbers. By this method, if a datum is determined n times at a given angle then

$$\sigma = \frac{\{\sum_{i=1}^{n}(channel1_i + channel2_i)\}^{1/2}}{n}. \tag{32}$$

Standard deviations were estimated in this manner for both the rare gas-methane scattering of Chapter 2 and the rare gas-chlorine scattering of Chapter 3. However, for the rare gas-chlorine studies, the confidence limit for replicate measurements[41] was also calculated. The two estimated uncertainties were compared and the larger of the two was used for that datum. For laboratory angles less than 5° from the primary beam, the method of Pack *et al.*[42] was used to estimate the error bars.

1.4.2 Data Analysis

The procedure used to fit the data was an iterative "trial and error" fitting method. In this method, an analytical form of the potential is chosen and its

parameters adjusted until the laboratory scattering distribution predicted by the potential are in good agreement with the experimental data. To predict the laboratory scattering distribution, it is necessary to calculate the center-of-mass differential cross section as in Section 1.2.2 then transform that data to the laboratory frame while accounting for the finite resolution of the apparatus. A computer program,[37] supplied by Professor Yuan Lee while at Caltech as a Fairchild Scholar, was used as the basis for the code we would eventually use to perform these calculations. Many errors and inefficiencies were detected in the original code which we have corrected in the present version. Some of the improvements we have made will be discussed where appropriate. The remainder of this section outlines the basic procedures used in the calculation of laboratory scattering distributions.

The number of primary beam particles scattered into an element of laboratory solid angle, $d\Omega$, at center-of-mass angle, θ, per unit time is just the product of the average number of target molecules in some collision volume, V, the flux of the primary beam, the center-of-mass differential cross section, and the proper Jacobian for the center-of-mass to laboratory transformation. In equation form this amounts to

$$I(\Theta) = (n_2 V)(n_1 v_{rel}) \frac{d\sigma}{d\omega}(\theta, E) \left| \frac{d\omega}{d\Omega} \right| , \tag{33}$$

where Θ is the laboratory angle corresponding to θ, n_i is the number density of beam i, and $|\frac{d\omega}{d\Omega}|$ is the Jacobian. It can be shown[43] that the Jacobian for elastic scattering is just

$$J = \left| \frac{d\omega}{d\Omega} \right| = \left| \frac{(v_1')^2}{(u_1')^2 cos\delta} \right| , \tag{34}$$

where v_1', u_1', and δ are defined as in Figure 1 in Section 1.2.1.

However, since the differential cross section is a function of the center-of-mass energy, it is also a function of the velocities of both beams and their collision angle. To account for the spread in beam velocities and the finite resolution of the apparatus we must integrate equation (33) over all possible beam velocities, the volume of the collision region and the solid angle subtended by the detector. Equation (33) then becomes

$$I(\Theta) = \int_{v_1}\int_{v_2}\int_z\int_y\int_x\int_{\Omega_d} n_1(v_1)n_2(v_2)|\vec{v}_1 - \vec{v}_2|\frac{d\sigma}{d\omega}(\theta, E)J\, d\Omega\, dx\, dy\, dz\, dv_2\, dv_1. \tag{35}$$

The multiple integral of Equation (35) may seen formidable, but numerical methods have been developed which greatly simplify the calculation.[44] For instance, the integration over the velocity spreads of both beams can be done using the assumed velocity distribution of the beams (Equation 31 in Section 1.3) and some sort of numerical integration. Because of the $e^{-(v-v_0)^2}$ dependence of the velocity distribution, Gauss-Hermite integration is particularly well suited for this problem. The Gauss-Hermite formula is[25]

$$\int_{-\infty}^{\infty} e^{-x^2} f(x)dx = \sum_{i=1}^{n} w_i f(x_i)\ , \tag{36}$$

where x_i is the i^{th} zero of the Hermite polynomial of degree n, and w_i is the weighting factor associated with x_i. The number of the quadrature points, n, that are used depends on the behavior of the function, $f(x)$, and the accuracy desired.

The collision volume integral is performed in a similar fashion. The first step is to assume a number density distribution across the beam width and height. Since our beams have been collimated to have very small angular divergence, we assume a uniform distribution across their widths and heights. The collision volume integral can then be reduced to a weighted sum over discrete values as in Equation (36), but because there is no exponential dependence, Gauss-Legendre integration is used. The Gauss-Legendre formula is[25]

$$\int_a^b f(y)dy = \frac{b-a}{2}\sum_{i=1}^{n} w_i f(y_i) \ , \tag{37}$$

where $2y_i = (b-a)x_i + (b+a)$, x_i is the i^{th} zero of the Legendre polynomial of degree n, and w_i is the weighting factor associated with x_i.

The integration over the solid angle subtended by the detector is also performed using Gauss-Legendre numerical integration with the detector acceptance function assumed to be constant. The inclusion of this integration scheme was a major improvement over the Simpson's Rule integration routine that was originally in the Berkeley code.[37] For a calculation using only apparatus averaging in the plane defined by the two beams, Gaussian integration with three quadrature points reduced the computation time by a factor of three over the original code while achieving equivalent results. Using less than three quadrature points led to erroneous results.

Incorporating all three of these numerical integration routines reduces the integrals of Equation (35) to the sum of sums expressed in Equation (38),

$$I(\Theta) = \sum_{i=1}^{I(v_1)} \sum_{j=1}^{J(v_2)} \sum_{k=1}^{K(z)} \sum_{l=1}^{L(y)} \sum_{m=1}^{M(x)} \sum_{n=1}^{N(\Omega_d)} W_{ijklmn} |\vec{v}_i - \vec{v}_j| \frac{d\sigma}{d\omega}(\vec{v}_i, \vec{v}_j, \theta) J \ , \tag{38}$$

where W_{ijklmn} is the product of all the individual weights from the various integrations and also includes $f(x_i)$ and $f(x_j)$ from Equation (36). The integrals have thus been replaced by a sum over $I \times J \times K \times L \times M \times N$ center-of-mass differential cross sections. In practice, we have found the laboratory scattering to be relatively insensitive to any integration over the "out of plane" beam ($K(z) = 1$) or the detector height ($N(\Omega_d) = N(\Theta_d)$). Also, for the experiments in this report, the primary beam was so narrow that no integration was required over its width ($M(x) = 1$)). The effect of the summation in Equation (38) is best demonstrated by comparing $I(\Theta)$ for $I = J = K = L = M = N = 1$ and for a reasonable amount of velocity, collision volume and detector averaging. Two laboratory differential cross sections calculated in this manner from the same potential are compared in Figure 9.

Modeling the experimental laboratory scattering intensity has thus been found to be a tractable problem, but it is still necessary to determine the parameters of the potential which produce the best fit to the measured scattering intensity. This was done using an iterative routine which adjusted the parameters of the potential until the overall dimensionless root mean square deviation was minimized. The overall dimensionless rms deviation as defined by Pack *et al.*[42] is

$$\delta = \left[\frac{1}{n} \sum_{j=1}^{n} \delta_j^2 \right]^{1/2} , \tag{39}$$

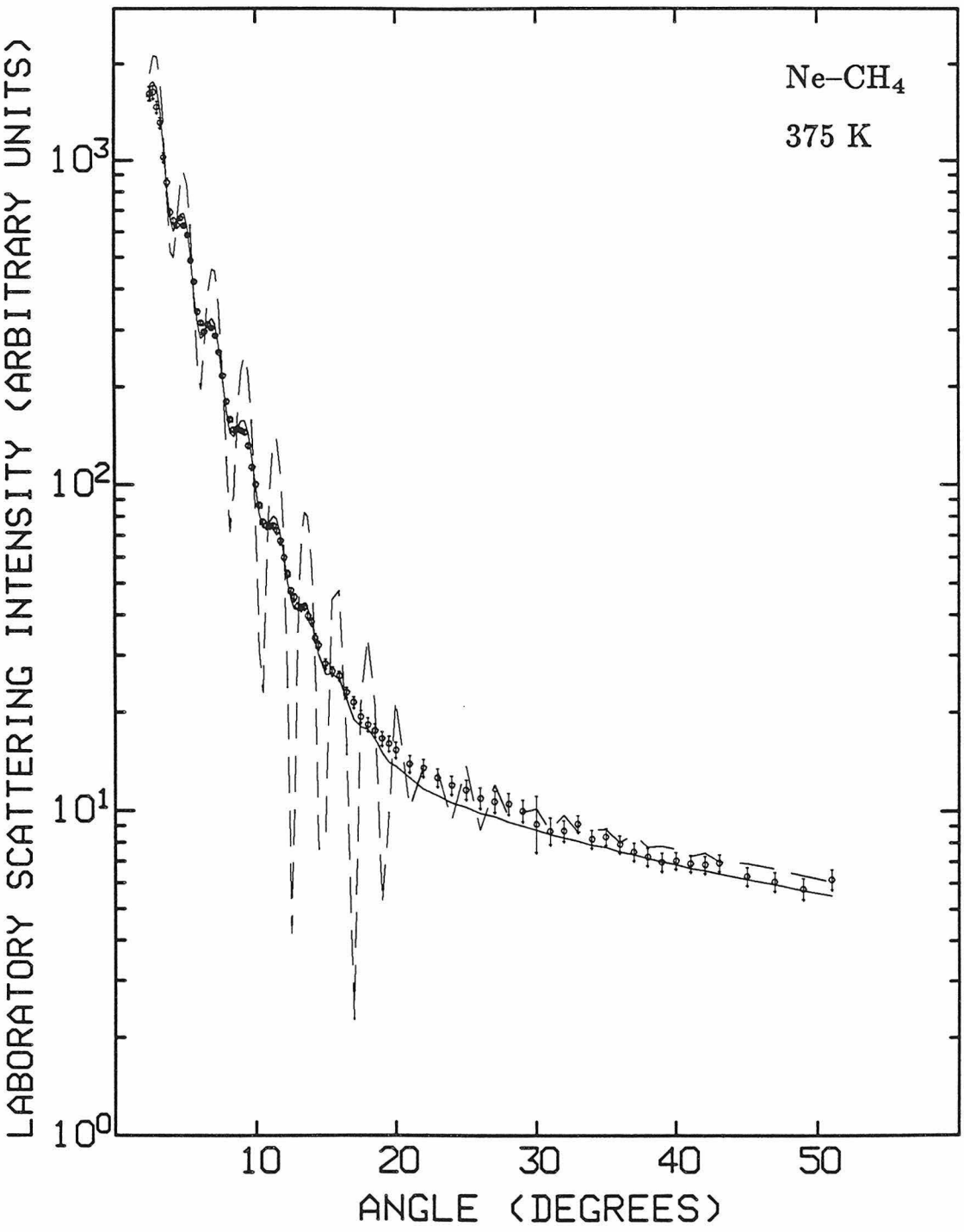

Figure 9. Laboratory scattering intensities as a function of laboratory angle. The ○ are experimental values, - - - indicates the calculated intensity for infinite resolution, and — indicates the intensity calculated from the same potential but accounting for finite resolution.

where n is the number of data sets (collision energies and bulk properties), and δ_j is the dimensionless rms deviation for the j^{th} experiment. δ_j^2 is defined as

$$\delta_j^2 = \frac{1}{n_j} \sum_{i=1}^{n_j} \Delta_{ji}^{-2} (P_{ji} - p_{ji})^2, \tag{40}$$

where n_j is the number of data points for the j^{th} experiment, Δ_{ji} is the experimental uncertainty at the i^{th} datum, and P_{ji} and p_{ji} are the calculated and experimental values of the i^{th} datum. The minimization routine was started with several sets of initial parameters to assure the uniqueness of the determined potential.

With these methods, based on the theory and apparatus described in previous sections, we have measured laboratory scattering intensities as a function of angle and collision energy for several atom-molecule systems. In the next chapter, an isotropic approximation has been used to model the pseudo-spherical interactions of methane with neon and argon, and in the final chapter the infinite order sudden approximation has been utilized to determine anisotropic interaction potentials for chlorine with helium and neon.

References

[1] R.G.J. Fraser and L.F. Broadway, Proc. Roy. Soc. A **141**, 626–633, (1933).

[2] U. Buck, Adv. Chem. Phys. **30**, 313–388, (1975).

[3] G. Scoles, Ann. Rev. Phys. Chem. **31**, 81–96, (1980).

[4] G.C. Maitland, M. Rigby, E.B. Smith and W.A. Wakeham, *Intermolecular Forces: Their Origin and Determination* (Oxford University Press, Oxford, England, 1981).

[5] M.S. Child, *Molecular Collision Theory* (Academic Press, New York, 1974).

[6] H. Pauly, in, *Atom - Molecule Collision Theory: A Guide for the Experimentalist*, edited by R.B. Bernstein (Plenum Press, New York, 1979).

[7] N.L. Allinger, Adv. Phys. Org. Chem. **13**, 1–82, (1976).

[8] H.A. Scheraga, Adv. Phys. Org. Chem. **6**, 103–184, (1968).

[9] G.O. Este, G. Knight and G. Scoles, Chem. Phys. **35**, 421–427, (1978).

[10] J.T. Slankas, M. Keil and A. Kuppermann, J. Chem. Phys. **70**, 1482–1491, (1979).

[11] C.H. Becker, P.W. Teidemann, J.J. Valentini and Y.T. Lee, J. Chem. Phys. **71**, 481–489, (1979).

[12] M. Faubel and J.P. Toennies, Adv. At. Mol. Phys. **13**, 229–314, (1978), and references therein.

[13] R.T Pack, J.J. Valentini, and J.B. Cross, J. Chem. Phys. **77**, 5486–5499, (1982).

[14] J.W. Winneczek, *Ph.D. Thesis* (California Institute of Technology, 1985), and references therein.

[15] U. Buck, J. Schleusener, D.J. Malik and D. Secrest, J. Chem. Phys. **74**, 1707–1717, (1981).

[16] B.P. Reid, M.J. O'Loughlin and R.K. Sparks, J. Chem. Phys., in press.

[17] K.C. Janda, Adv. Chem. Phys. **60**, 201–244, (1985), and references therein.

[18] D.E. Brinza, B.A. Swartz, C.M. Western and K.C. Janda, J. Chem. Phys. **79**, 1541–1542, (1983).

[19] D.E. Brinza, C.M. Western, D.D. Evard, F. Thommen, B.A. Swartz and K.C. Janda, J. Phys. Chem. **88**, 2004–2009, (1984).

[20] J.A. Beswick and J. Jortner, J. Chem. Phys. **69**, 512–518, (1978), and references therein.

[21] G.E. Ewing, J. Chem. Phys. **71**, 3143–3144, (1979).

[22] H.S.W. Massey and C.B.O. Mohr, Proc. Roy. Soc. A **141**, 434–453, (1933).

[23] See, for example, J.S. Cohen, J. Chem. Phys. **68**, 1841–1843, (1978).

[24] R.B. Bernstien, J. Chem. Phys. **33**, 795–804, (1960).

[25] See, for example, M. Abromowitz and I.A. Stegun, editors, *Handbook of Mathematical Functions* (Dover Publication, New York, 1965).

[26] U. Buck and H. Pauly, J. Chem. Phys. **51**, 1662–1664, (1969).

[27] U. Buck, J. Chem. Phys. **54**, 1923–1928, (1971).

[28] U. Buck, Rev. Mod. Phys. **46**, 369–389, (1974).

[29] See, for instance, U. Buck, H. Meyer and R.J. LeRoy, J. Chem. Phys. **80**, 5589–5597, (1984).

[30] G.A. Parker and R.T Pack, J. Chem. Phys. **68**, 1585–1601, (1978), and references therein.

[31] D.J. Kouri, in, *Atom Molecule Collision Theory: A Guide to the Experimentalist*, edited by R.B. Bernstien (Plenum Press, New York, 1979).

[32] D.J. Kouri, T.G. Heil and Y. Shimoni, J. Chem. Phys. **65**, 1462–1473, (1976).

[33] Z.H.Top and D.J. Kouri, Chem. Phys. **37**, 265–270, (1979).

[34] Y.T. Lee, J.D. McDonald, P.R. LeBreton and D.R. Herschbach, Rev. Sci. Instrum. **40**, 1402–1408, (1969).

[35] R.K. Sparks, *Ph.D. Thesis* (University of California, Berkeley, 1979).

[36] See, for instance, J.B. Anderson, R.P. Andres and J.B. Fenn, Adv. Chem. Phys. **10**, 275–317, (1966).

[37] M.F. Vernon, *Ph.D. Thesis* (University of California, Berkeley,1983).

[38] G.O. Brink, Rev. Sci. Instrum. **37**, 857–860, (1966).

[39] N.R. Daly, Rev. Sci. Instrum. **31**, 264–267, (1960).

[40] S.Dushman, *Scientific Foundations of Vacuum Technique* (John Wiley and Sons, New York, 1976).

[41] D.A. Skoog and D.M. West, *Fundamentals of Analytical Chemistry* (Holt, Reinhart and Winston, New York, 1976).

[42] R.T Pack, J.J. Valentini, C.H. Becker, R.J. Buss, and Y.T. Lee, J. Chem. Phys. **77**, 5475–5485, (1982).

[43] G.L. Catchen, J. Husain and R.N. Zare, J. Chem. Phys. **69**, 1737–1741, (1978).

[44] R.T Pack, J. Chem. Phys. **81**, 1841–1850, (1984).

Chapter 2

Neon-Methane and Argon-Methane
Isotropic Interaction Potentials
from
Total Differential Cross Sections

Neon-Methane and Argon-Methane Isotropic Interaction Potentials from Total Differential Cross Sections*

Michael J. O'Loughlin, Brian P. Reid and Randal K. Sparks

The Arthur Amos Noyes Laboratory of Chemical Physics,
California Institute of Technology, Pasadena, California 91125

Accepted for publication in *The Journal of Chemical Physics.*

Abstract

Total differential cross sections have been measured at three collision energies each for Ne–CH_4 and Ar–CH_4 using the crossed molecular beams technique. The differential cross sections were used along with literature viscosity and second virial coefficient data to determine reliable isotropic interaction potentials. The Ne–CH_4 potential has a well depth of 66 ± 4 K and an intermolecular separation of $3.68 \pm .02$ Å at the minimum while the Ar–CH_4 potential has a well depth of 170 ± 8 K and an intermolecular separation of $3.85 \pm .04$ Å at the minimum. The Ne–CH_4 is significantly different from the spherical part of the potential proposed by Buck *et al.* The well depth of that potential is about 16% shallower and the intermolecular separation about 4% larger than in our potential. Their potential does not reproduce our total differential cross sections within reasonable uncertainty limits.

---

* Contribution # 7223

2.1 Introduction

Techniques for determining interatomic potentials from elastic scattering of crossed molecular beams are well developed and many such potentials have been reported.[1] However, applications of atom-atom potentials are somewhat limited and attention has been shifted towards the determination of atom-molecule and molecule-molecule potentials. These potentials and their determination are considerably more complicated because the potential depends not only on the internuclear distance but also on the orientation of the molecules. Exact quantum mechanical scattering calculations on complex anisotropic systems are not as yet practical, and common approximate techniques such as the infinite order sudden approximation are only valid under restricted circumstances. For those molecules for which approximate methods are not well developed, effective isotropic potentials can be determined using the same procedures successfully applied to atom-atom scattering.[2] This spherical approximation is particularly appealing when applied to pseudo-spherical molecules such as methane.

Recently, studies on anisotropic potentials for argon and krypton with SF_6[3] and for several atom-diatom systems[4] have shown that total differential cross sections (DCS) and bulk properties, such as viscosities and interaction second virial coefficients, for these systems can be reproduced by the spherical limit of the true anisotropic potential but not as well by the spherical average of that potential.[5] This implies that a spherical potential fit to an anisotropic system would be closely related to the spherical limit of the true potential. In addition, the work of Buck *et al.* indicates that for argon-methane[6] and helium-methane[7] the difference between

the effective isotropic potential and the spherical average of the anisotropic potential is not significant enough to preclude the use of the isotropic potential as a good first approximation to the spherical average for those systems. These results indicate that the use of a spherical approximation to determine isotropic intermolecular potentials for methane with neon and argon could be quite successful. These potentials would be particularly useful to theoreticians attempting to model inter- and intramolecular interactions of larger molecules containing methyl groups and atomic[8] or molecular[9] species that can be modeled by neon and argon.

In the present study, we have measured total DCS's at three collision energies for methane scattered from neon, argon and methane. The DCS's for all three collision energies were then used along with viscosity[10] and second virial coefficient[11] data to determine the parameters of a Morse-Morse-spline-van der Waals (MMSV) potential for each interacting pair. In addition, each individual collision energy was fit along with the bulk data to determine reasonable bounds on the potential fit to all three energies. Details of the methane-methane potential determination have been presented elsewhere.[12]

The use of DCS's measured at three collision energies should produce a more accurate potential for two reasons. First, data from the different collision energies are sensitive to somewhat different areas of the potential energy surface and therefore are complimentary in the determination of that surface. This is particularly useful for these anisotropic systems where sensitivity to different areas of the potential surface can help to determine the effect of anisotropy on the DCS's.

Second, the use of several data sets minimizes the effects of uncertainties in the determination of the instrumental parameters.

2.2 Experimental

The crossed molecular beams apparatus used in this experiment is nearly identical to the high resolution version[12] of the standard design of Lee *et al.*[13] In the apparatus, two supersonic molecular beams are crossed at 90° and scattered molecules are detected using a quadrupole mass spectrometer with an electron impact ionizer. The detector, with a 1° aperture, rotates in the plane defined by the two beams. Detector aperture dimensions and beam dimensions are described in Figure 1. Methane beams (primary beams) were scattered off target beams of neon and argon (secondary beams) and the intensity of the scattered methane was detected as a function of angle measured with respect to the primary beam. Laboratory scattering distributions were measured at three collision energies each for the neon-methane and argon-methane systems.

The collision energy was altered by adjusting the flow velocity of the molecular beams. This was accomplished by varying the temperature of the gas in the stagnation region of the beam source. Room temperature beams were produced by expansion of the pure gases through quartz nozzles, while lower temperatures were achieved using the liquid nitrogen cooled, temperature controlled beam sources described in Chapter 1. All beam sources had .075 mm diameter orifices and were doubly differentially pumped. Velocity distributions of the beams were measured

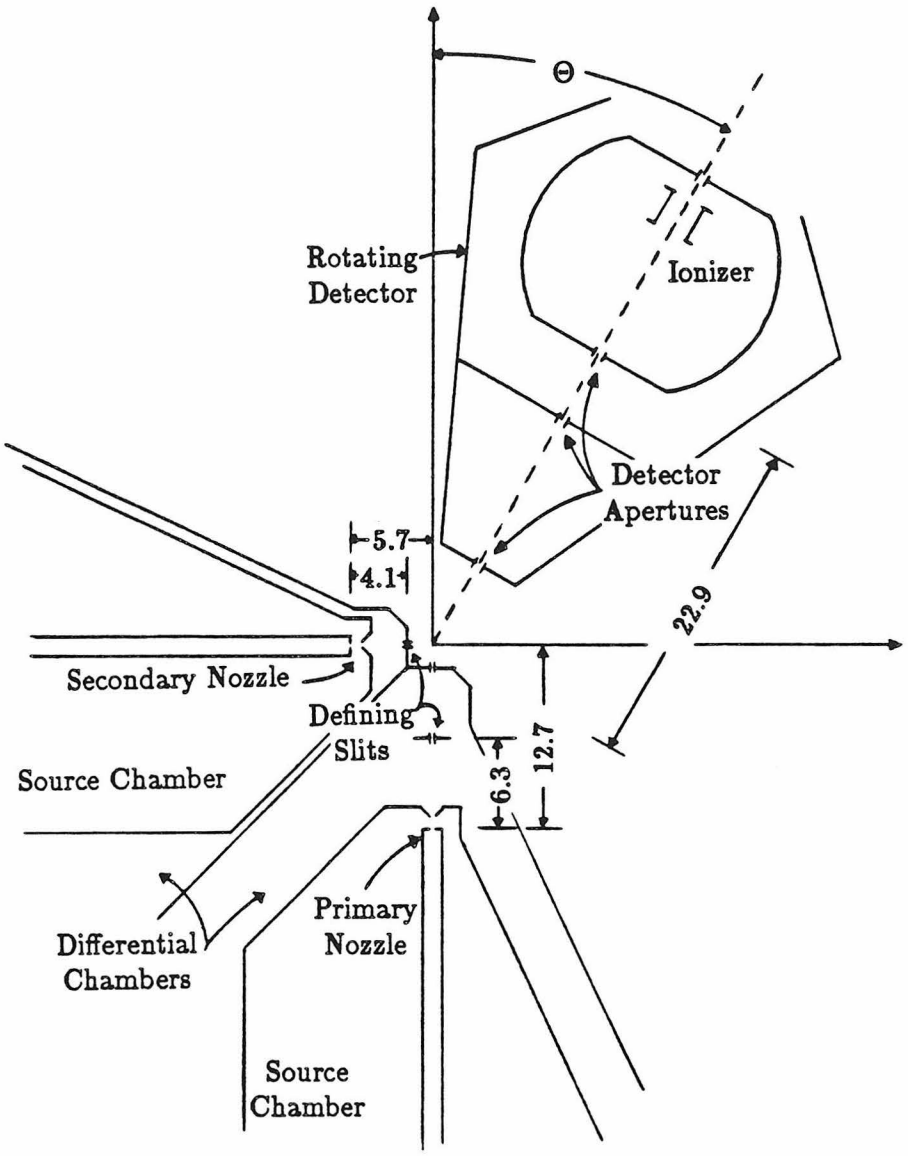

Figure 1. Schematic showing the geometry of the molecular beams apparatus used in the DCS measurements. Dimensions shown are in centimeters. The primary beam collimating slit is 0.38 mm wide (in plane) and 0.89 mm high (out of plane). The secondary beam collimating slit is 1.0 mm wide and 2.0 mm high. All of the detector aperatures are 4.0 mm square.

using time-of-flight techniques. The distributions were then fit to the functional form,

$$P(v) \propto v^2 e^{s^2(v-v_0)^2/v_0^2}, \tag{1}$$

to determine the best values of s, the speed ratio, and v_0, the flow velocity. Convenient beam source temperatures were selected and then gas pressures in the stagnation region were varied to maximize beam intensities while maintaining the signal of van der Waals dimers at less than .25% of the monomer signal. Beam source temperatures, stagnation pressures, velocities and speed ratios for each collision pair and each collision energy are shown in Tables 1 and 2. Laboratory angles of the beams were verified by scanning through the beams with a .150 mm aperture placed in front of the detector. Center of mass scattering distributions on either side of 0° were also compared for the low temperature, well resolved neon-methane data (see Figure 8, Chapter 1). All beams were found to be within $\pm\frac{1}{8}^\circ$ of their nominal positons.

Intensity distributions of the scattered methane were obtained by repeated scans through the angles reported while periodically returning to a fixed reference angle (usually 10°) to account for long term drift in operating conditions. The secondary beam was modulated with a 150 Hz tuning fork chopper to account for background from the primary beam source. Data was collected by high speed pulse counters which were gated synchronously with the tuning fork chopper. The counters were interfaced with a laboratory minicomputer which performed background subtraction and data averaging. Total counting times ranged from six minutes at small angles to seventeen minutes at large angles. The measured

Table 1: Beam source characteristics for neon-methane at three collision energies.

	collision energy		
characteristics	1010 K	637 K	375 K
gas	CH_4‖Ne	CH_4‖Ne	CH_4‖Ne
stagnation pressure(torr)	780‖1530	920‖1400	320‖1000
stagnation temperature(K)	303‖303	199‖199	118‖118
velocity(10^4 cm/sec)	11.25‖7.90	8.84‖6.41	6.79‖4.90
speed ratio	7.6‖20.3	9.8‖20.1	9.4‖17.0

Table 2. Beam source characteristics for argon-methane at three collision energies.

	collision energy		
characteristics	1081 K	678 K	400 K
gas	CH_4‖Ar	CH_4‖Ar	CH_4‖Ar
stagnation pressure(torr)	800‖1430	920‖700	320‖600
stagnation temperature(K)	303‖303	199‖199	118‖118
velocity(10^4 cm/sec)	11.25‖5.58	8.84‖4.55	6.79‖3.50
speed ratio	7.6‖22.0	9.8‖18.5	9.4‖15.2

distributions with estimates of the corresponding uncertainties are tabulated in Appendix B.

2.3 Analysis

Although direct inversion of DCS data to yield a numerical potential is possible for some simple atom-atom scattering pairs,[14] the rare gas–methane DCS's are affected by the anisotropy of the potential and it was felt that a reliable potential could not be determined by inversion. Instead, to determine an effective spherical potential for these systems we chose to use a trial and error method. In this method, an analytical form for the potential is chosen and its parameters are estimated. Laboratory scattering intensities, viscosities, and interaction second virial coefficients are calculated from that potential. The calculated quantities are compared with the experimental results, potential parameters are changed, and the procedure is repeated in order to minimize the deviation of the calculated quantities from the experimental data. The analytical potential form, the details of the calculations using that form, and the fitting procedure are presented in the following sections.

2.3.1 Potential

The potential form used in these calculations is a peicewise analytical Morse-Morse-spline-van der Waals (MMSV) function. The first Morse function is joined to the second at $r = \sigma$, the point at which the potential crosses zero, as in the potential used by Keil *et al.*[15] The MSV portion of the potential is like that used

by Siska *et al.*[16] Written in reduced form ($x = r/r_m$, $f(x) = U(x)/\epsilon$, where r_m is the radius of the potential minimum and ϵ its depth), the potential used is

$$f(x) = \begin{cases} \omega^{-1} e^{\beta_1 - x\beta_2\omega}[e^{\beta_1 - x\beta_2\omega} - 2] & \text{if } x < 1 - \beta_2^{-1}\ln 2 \\ e^{\beta_2(1-x)}[e^{\beta_2(1-x)} - 2] & \text{if } 1 - \beta_2^{-1}\ln 2 \le x \le x_1 \\ b_1 + (x - x_1)\{b_2 + (x - x_2)[b_3 + (x - x_1)b_4]\} & \text{if } x_1 < x < x_2 \\ -c_6 x^{-6} - c_8 x^{-8} & \text{if } x_2 \le x \end{cases}, \tag{2}$$

where $\omega = (\beta_1 - \ln 2)/(\beta_2 - \ln 2)$, and $c_i = C_i/\epsilon r_m^i$. The C_i are the long range van der Waals dispersion coefficients. The spline coefficients, b_i, are determined by the constraints that the potential and its first derivative be continuous at x_1 and x_2.

2.3.2 Differential Cross Sections

The laboratory scattering intensities were determined using a previously published computer code[17] which was modified to suit our requirements. In brief, the program calculates the center of mass differential cross sections using the standard formulae for elastic scattering.[18] It then transforms them to the laboratory reference frame accounting for the finite resolution of the experiment by integrating over the velocity and angular spreads of the two molecular beams and the detector width. It was found that inclusion of the scattering out of the plane defined by the two beams produced only minor improvements in the calculated distributions, and thus for computing efficiency, we considered only the "in plane" scattering. The calculated cross sections are then scaled to minimize the sum of the squares of the differences between the experimental and calculated values divided by the experimental uncertainty. For methane scattered from neon, it was necessary to include contributions to the scattering intensity from both ^{20}Ne (91% natural abundance) and ^{22}Ne (8.8%). The computational methods for performing these

simulations of the laboratory scattering intensities have been discussed in detail in Chapter 1 and will only be briefly reviewed below.

Averaging over the velocity spreads of both beams was accomplished by using Gauss-Hermite quadrature. The functional form of the velocity distribution that was used in the quadrature scheme was already presented in Equation (1). The number of quadrature points varied depending on the velocity and the speed ratio of the beam. In general, 6 or 7 quadrature points were used for the methane beams, and 4 or 5 for the rare gas beams.

The angular spread of the beams was accounted for by assuming a flat density distribution across the width of the beams and using Gauss-Legendre quadrature to sample the collision area. Three point quadrature was used across the secondary beam width (0.174 cm in the collision region) while the narrow width of the primary beam (0.075 cm) made the use of more than one point integration unnecessary.

The JWKB approximation and eight point Gauss-Mehler quadrature were used to calculate the phase shifts for the partial wave analysis.[19] The phase shifts were calculated at each collision energy determined by the velocity quadrature points from the velocity averaging routine. Since the velocity spreads of the beams were in general larger than the angular spreads, the phase shifts were not recalculated at each collision area quadrature point. At each collision energy, 200(300) partial waves were used in the neon(argon)-methane calculations. It was found that calculating the phase shifts at only ten energies and using four point Lagrange polynomial interpolation to determine the phase shifts at the desired energies produced almost equivalent results and this procedure was used in some of the fitting.

Finally, the detector width averaging was accounted for by assuming a flat detection sensitivity across the entire width and using Gauss-Legendre quadrature to integrate the intensity. Even for the highly structured neon-methane data, three point quadrature was found to be sufficient.

2.3.2 Viscosities

Mixture viscosities were calculated using the first order Chapman-Enskog approximation.[20] The necessary calculation of phase shifts, generalized cross sections and collision integrals were carried out following the procedures of Parker and Pack.[21] Specifically, phase shifts were calculated at 20 energies logarithmically spaced between 50 and 10,000 K. (K has been chosen as the unit of energy throughout this paper. By multipling by k_B, the Boltzmann constant, one can easily convert to any unit of energy.) Below 100 K an exact quantum routine was used while above this energy JWKB phase shifts were employed. The maximum partial wave used was given by $50+12k$ where k is the wave number in atomic units. The generalized cross sections obtained at the 20 energies were used along with four point Lagrange interpolation and ten point Gauss-Laguerre quadrature to calculate the necessary collision integrals. The calculated viscosities were compared with data reported by Kestin and Ro at four mole fractions and five temperatures for both the neon and argon systems.[10] The necessary viscosities of pure methane, argon and neon where taken from a critical compilation of viscosities by Maitland and Smith.[22] The uncertainties used for the mixture data were those given by Kestin and Ro plus the uncertainties in the calculation introduced by the uncertainties in the viscosities of the pure components.

2.3.3 Second Virial Coefficients

Interaction second virial coefficients (ISVC) were calculated from the reduced form of the intermolecular potential using the formula:[20a]

$$B_{12}(T) = B_{cl}(T) + \frac{h^2}{2\mu} B_{q1}(T) \ , \tag{3}$$

where $B_{cl}(T)$ is the classical value of the ISVC,

$$B_{cl}(T) = -2\pi N_A \int_0^\infty [e^{-U(x)/k_B T} - 1] r^2 \, dr \ ,$$

$B_{q1}(T)$ is the first order quantum correction to the classical ISVC,

$$B_{q1}(T) = +2\pi N_A \left(\frac{1}{48\pi^2 {k_B}^3 T^3}\right) \int_0^\infty e^{-U(x)/k_B T} [U'(x)]^2 r^2 \, dr \ ,$$

N_A is Avagadro's constant, h is Planck's constant, μ the reduced mass, and $x = r/r_m$ is the reduced intermolecular distance. The analysis of these integrals and the sensitivity of the ISVC to the intermolecular potential are reviewed in great detail in Appendix A. An outline of the analysis is presented in the following paragraphs.

Integration over the classical integral was performed using the method outlined by Pack *et al.*[23] except that the regions over which analytical integration was performed were $x = 0$ to x_a and from $x = x_b$ to ∞, where x_a is the point at which $U(x) \approx 1.0 \times 10^4$ K and x_b is the largest value of x such that $U(x) \approx -1.0$ K. The quantum correction integral was divided into four parts. At small values of reduced internuclear distance ($x \leq .6$) the value of the integrand is typically fifty or more orders of magnitude less than the average value in the region of the

potential well and can therefore be neglected. Similarly, at large values of reduced internuclear distance the integrand once again approaches zero and can be neglected. The intermediate region is divided in two at $x = 1.0$ and the integral evaluated using ten point Gaussian integration for $x < 1.0$ and thirty two point Gaussian integration for $x > 1.0$.

Experimental values for $B_{12}(T)$ for argon-methane were obtained from a compilation of individual data sets of other authors by Dymond and Smith.[11] The large discrepancies in the reported argon-methane coefficients made it necessary to increase the error in their estimated accuracies. Error bars used were $\pm$ 10 cm^3/mol for $T <$ 110 K, $\pm$ 8 cm^3/mol for 110 K$\leq T <$ 145 K, $\pm$ 6 cm^3/mol for 145 K$\leq T <$ 400 K, and $\pm$ 4 cm^3/mol for $T \geq$ 400 K. No virial coefficient data was used for neon-methane.

2.3.5 Fitting and Uncertainties

The potential parameters were chosen as those that gave the "best" fit to the experimental data. This "best" fit was taken to be that which minimized the dimensionless mean square deviation as defined by Pack *et al.*[23] (see Equation 39, Chapter 1). For each scattering pair, this was done simultaneously for all three sets of scattering data, the viscosity data and the second virial coefficient data. In addition, each set of scattering data was fit individually with the bulk data in order to determine a range for the uncertainty in the potential.

The fit was performed by allowing all potential parameters to vary in a least squares fitting program with the following exceptions. The spline parameters, x_1 and x_2, were restricted so that there were no oscillations in the potential in the

spline region. In the argon-methane analysis, C_6 and C_8 were initially chosen as those values used by Buck *et al.*[6] and only allowed to vary after the other parameters had been optimized. For neon-methane, the value of C_6 was initially chosen as that of Dalgarno[24] and the value of C_8 was chosen such that the C_8 to C_6 ratio was the same as for argon-methane. As with argon-methane, these van der Waals coefficients were only allowed to vary after the other parameters had been optimized.

2.4 Results

The potential parameters determined from the least squares fit to the data are presented in Table 3 for neon-methane and Table 4 for argon-methane. In both tables, the parameters for the best fit to all the data (Potential A) are shown along with parameters for the best fit to each individual collision energy with the bulk property data (Potentials B-D). Potential A_{Ne} is shown in Figure 2 and Potential A_{Ar} is shown in Figure 3 along with estimated limits of uncertainty. The upper and lower bounds of the uncertainty were chosen such that for each system, Potentials A-D would lie completely within those limits.

The dimensionless rms deviations of each data set for each potential along with the overall dimensionless rms deviation for each potential are presented in Table 5 for neon-methane and Table 6 for argon-methane. Tables 5 and 6 also include those deviations calculated using the spherical potentials of Buck *et al.* for neon-methane[25] (Potential E_{Ne}) and argon-methane[6] (Potential E_{Ar}). From inspection of these tables it is clear that all of the potentials with the exception of those of Buck *et al.* reproduce the viscosity data very well. The anomolous behavior of the Buck *et al.* potentials is understandable since no viscosity data were used in their

Table 3. MMSV potential parameters for neon-methane overall best fit and best fit to each individual collision energy. Parameters are in reduced units unless specified otherwise.

parameters	Pot A_{Ne} overall	Pot B_{Ne} 375K	Pot C_{Ne} 637K	Pot D_{Ne} 1010K
ϵ(K)	65.9	66.4	61.9	64.9
r_m(Å)	3.676	3.676	3.694	3.670
x_1	1.026	1.022	1.062	1.070
x_2	1.32	1.32	1.42	1.58
β_1	4.00	4.00	4.65	6.70
β_2	7.42	7.42	7.18	6.50
c_6	1.228	1.219	1.270	1.260
c_8	.475	.471	.487	.489

Table 4. MMSV potential parameters for argon-methane overall best fit and best fit to each individual collision energy. Parameters are in reduced units unless specified otherwise.

parameters	Pot A_{Ar} overall	Pot B_{Ar} 400K	Pot C_{Ar} 678K	Pot D_{Ar} 1081K
ϵ(K)	169.6	162.5	170.6	177.6
r_m(Å)	3.850	3.815	3.815	3.815
x_1	1.05	1.04	1.05	1.07
x_2	1.59	1.77	1.42	1.52
β_1	4.15	6.75	4.30	4.10
β_2	7.50	7.60	7.61	7.40
c_6	1.182	1.358	1.327	1.192
c_8	.4456	.4305	.4831	.4690

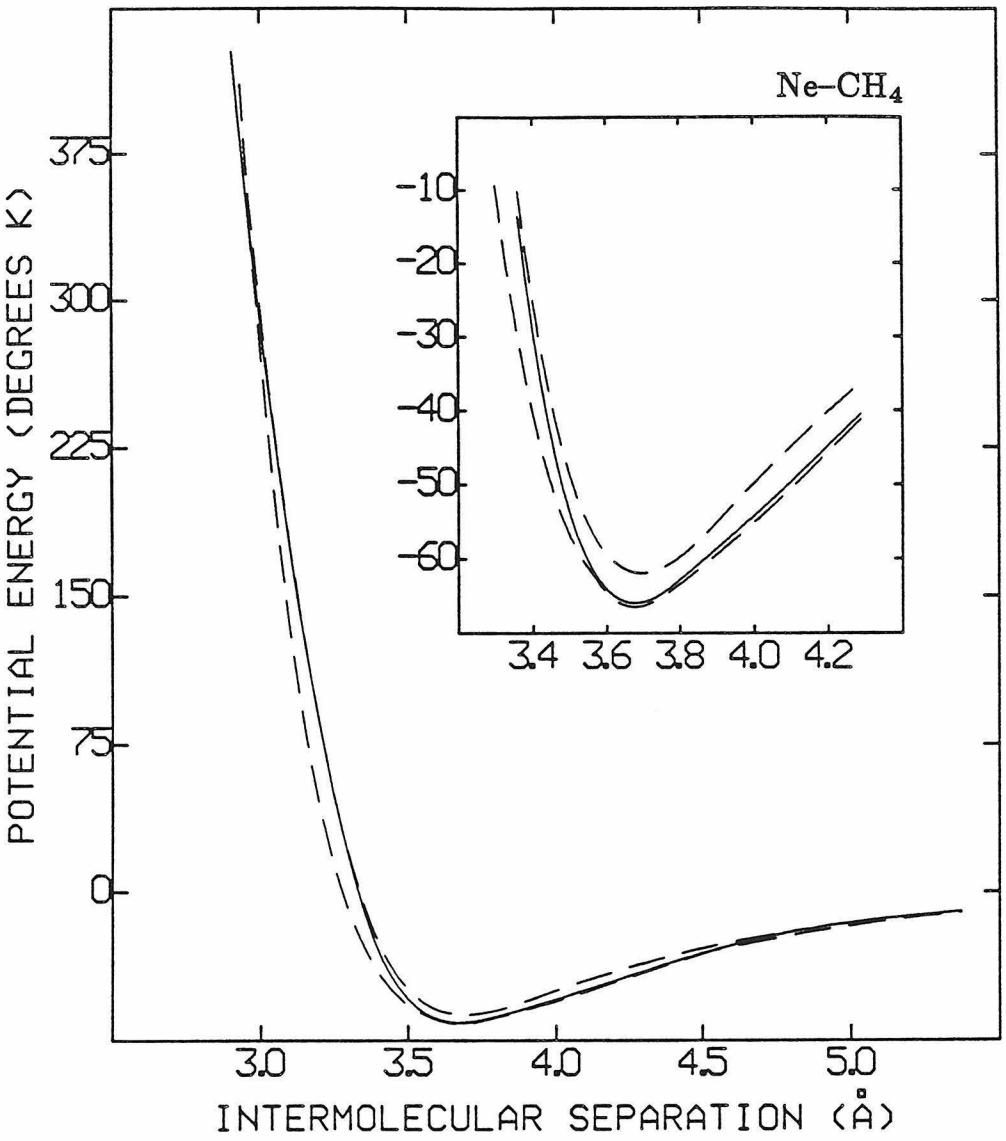

Figure 2. Potential A_{Ne} as a function of intermolecular separation. Dashed lines indicate the maximum and minimum values of all the potentials determined for this system.

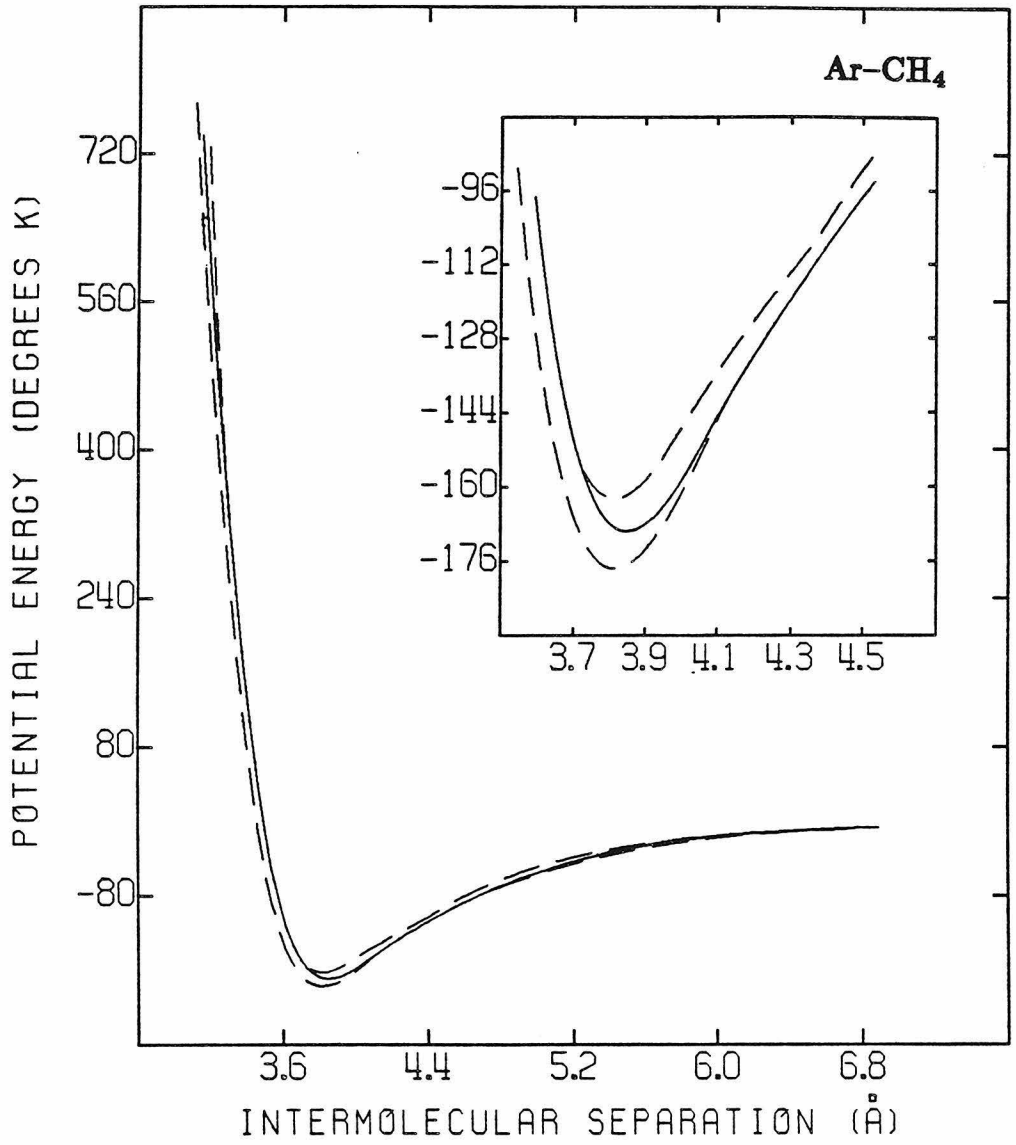

Figure 3. Potential A_{Ar} as a function of intermolecular separation. Dashed lines indicate the maximum and minimum values of all the potentials determined for this system.

Table 5. Comparison of calculated and experimental properties of neon-methane. Rms deviations for data sets with potentials from Table 3 and potential of Buck *et al.* (Pot E_{Ne}).

Data Set	Pot A_{Ne}	Pot B_{Ne}	Pot C_{Ne}	Pot D_{Ne}	Pot E_{Ne}
1010K	2.01	1.88	3.46	1.30	5.29
637K	4.44	4.68	3.94	5.53	7.62
375K	3.71	3.55	6.88	6.78	12.0
Vis.	0.48	0.52	0.26	0.30	5.84
Total	3.07	3.10	4.33	4.43	8.13

Table 6. Comparison of calculated and experimental properties of argon-methane. Rms deviations for data sets with potentials from Table 4 and potential of Buck *et al.* (Pot E_{Ar}).

Data Set	Pot A_{Ar}	Pot B_{Ar}	Pot C_{Ar}	Pot D_{Ar}	Pot E_{Ar}
1081K	3.95	8.83	4.20	1.09	3.18
678K	1.87	6.79	1.28	5.82	2.54
400K	4.72	2.63	5.50	8.56	7.69
Vir.	0.85	0.94	0.87	0.80	0.90
Vis.	0.88	0.32	0.26	0.29	1.56
Total	2.93	5.13	3.17	4.67	3.97

determination, however, this does indicate a deficiency in those potentials. The virial data is fit well by all the potentials, but this is not surprising given the large uncertainties involved in the data (see Appendix A). Considering the total neglect of anisotropy in the potential surface, the scattering data is also reproduced well by the potentials fit to all of the data sets.

The bulk properties predicted by our best overall potentials (Potentials A_{Ne} and A_{Ar}) are presented in Figures 4 to 6 along with the literature values for those properties. The laboratory DCS's calculated from the best overall potentials are shown superimposed on the experimental data in Figures 7 and 8. In addition, the calculated laboratory DCS's corresponding to the best fit to each individual data set of argon-methane are presented in Figure 9. The corresponding figure for neon-methane has been omitted because it was not significantly distinguishable from Figure 7.

For neon-methane, the diffraction (or rapid) oscillations are well resolved for the two lowest collision energies (the staircase like structure in the DCS's of Figure 7) and distinguishable in the 1010 K data, but a complete rainbow maximum was only resolved in the 375 K data (the rainbow maximum, which can be seen by scaling the DCS's by $\theta^{7/3}$, is at approximately $\Theta = 7°$). Both the diffraction oscillations and the rainbow maximum have been reproduced very accurately by Potential A_{Ne}. The uncertainty in the neon-methane potential (see Figure 2) is due almost entirely to the potential derived from the 1010 K data set in which there is no rainbow maximum and the diffraction oscillations are not prominent.

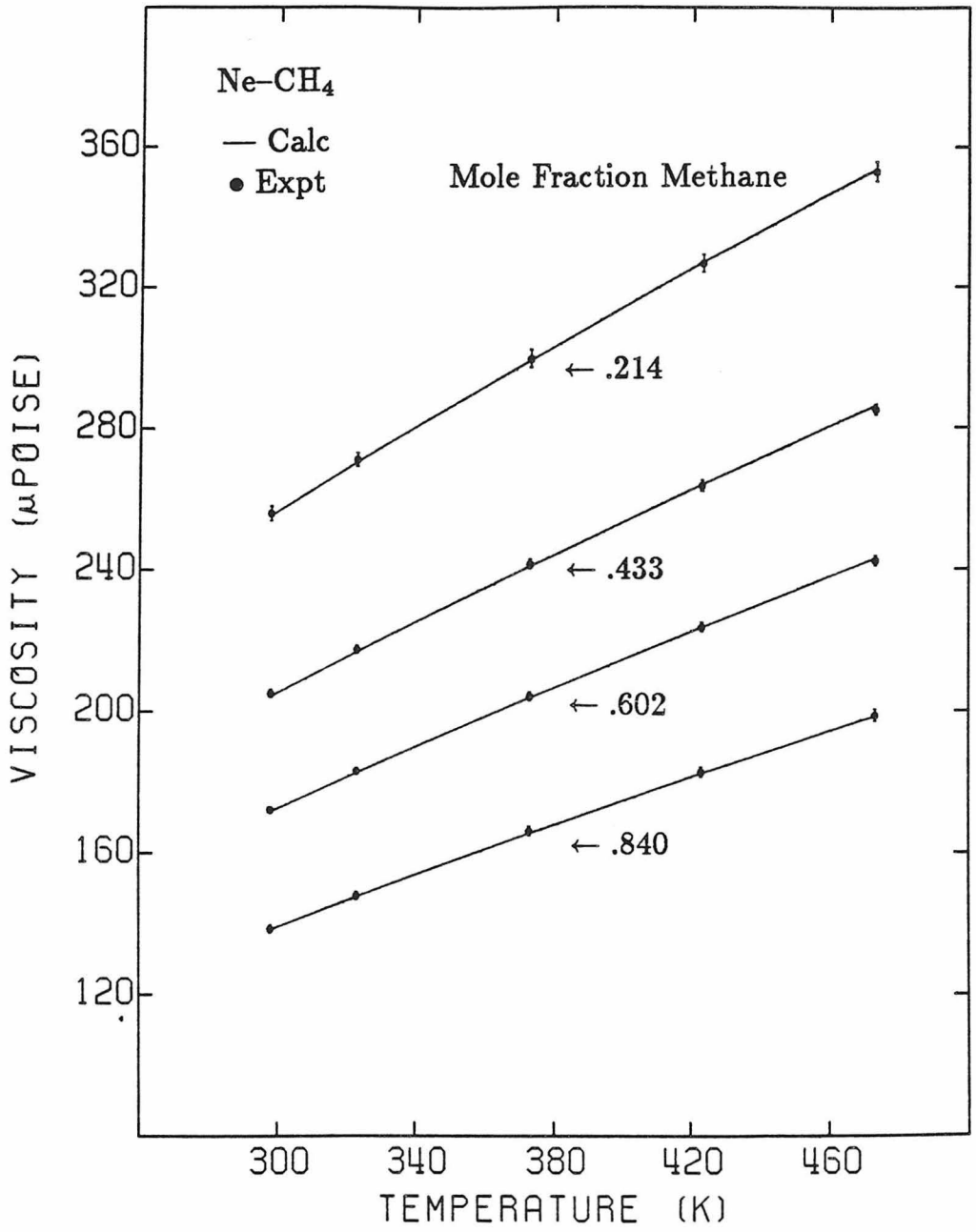

Figure 4. Neon-methane mixture viscosity as a function of temperature for four different mole fractions of methane. The experimental points are from reference 10.

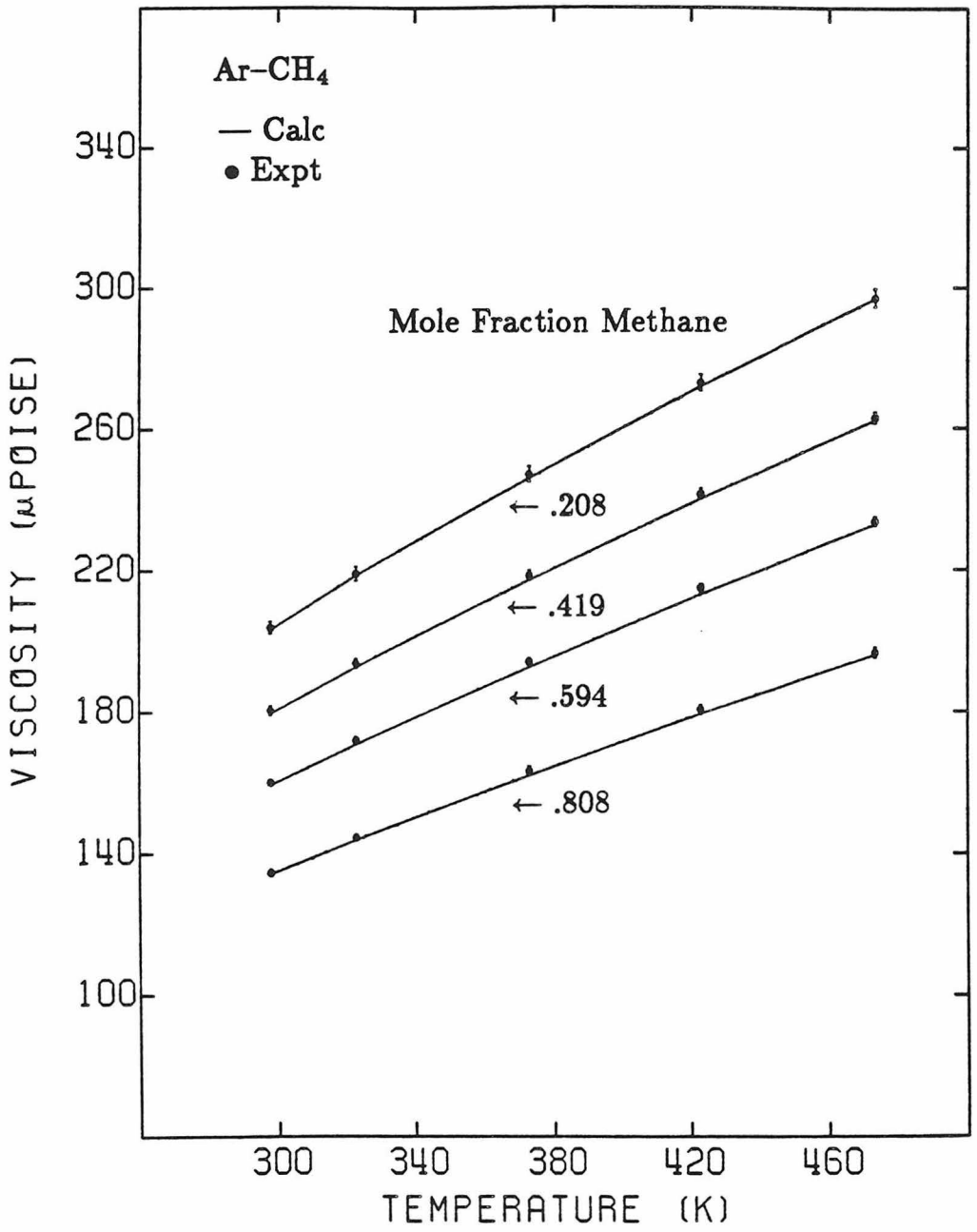

Figure 5. Argon-methane mixture viscosity as a function of temperature for four different mole fractions of methane. The experimental points are from reference 10.

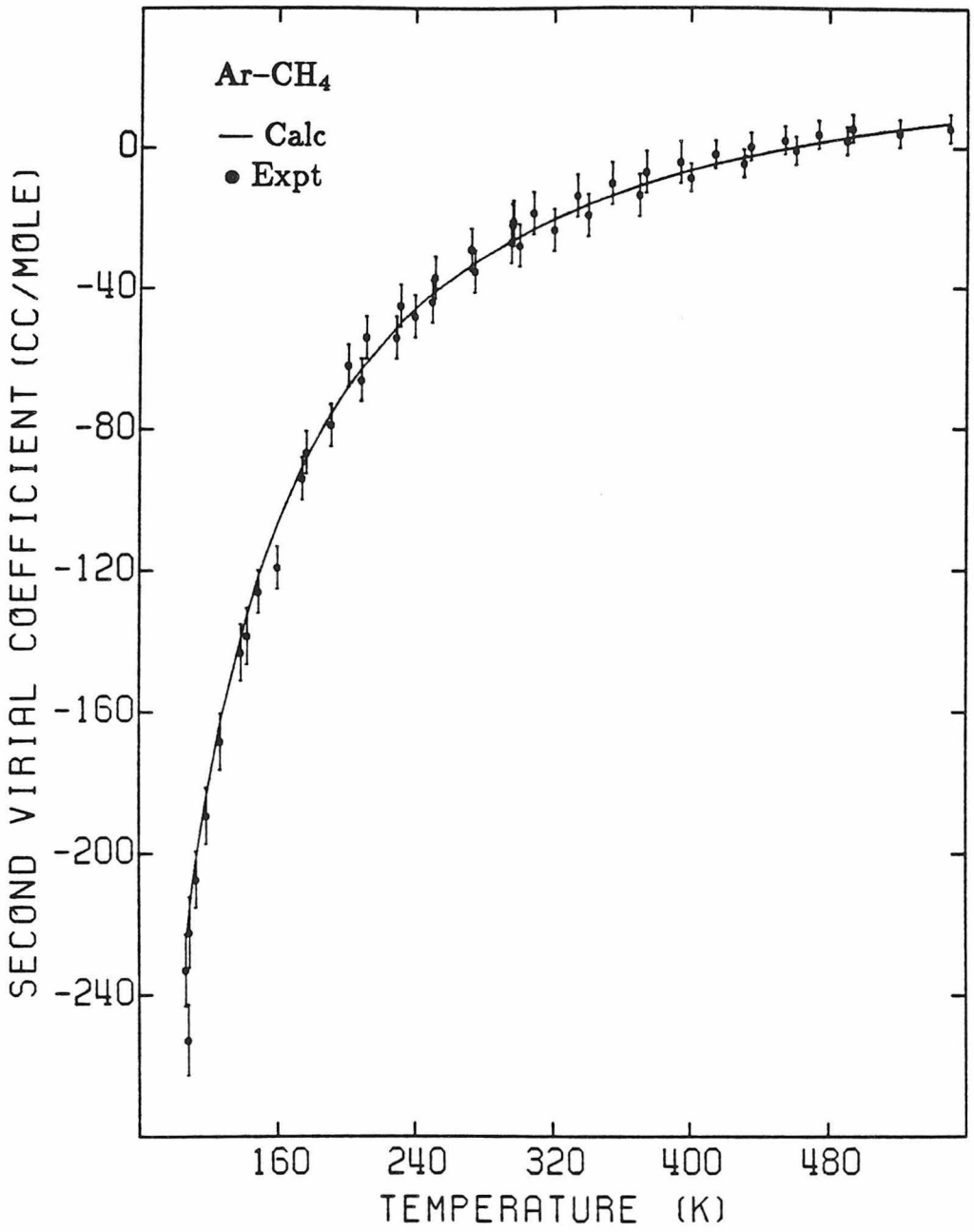

Figure 6. Argon-methane interaction second virial coefficients, $B_{12}(T)$, as a function of temperature. The experimental points are from reference 11.

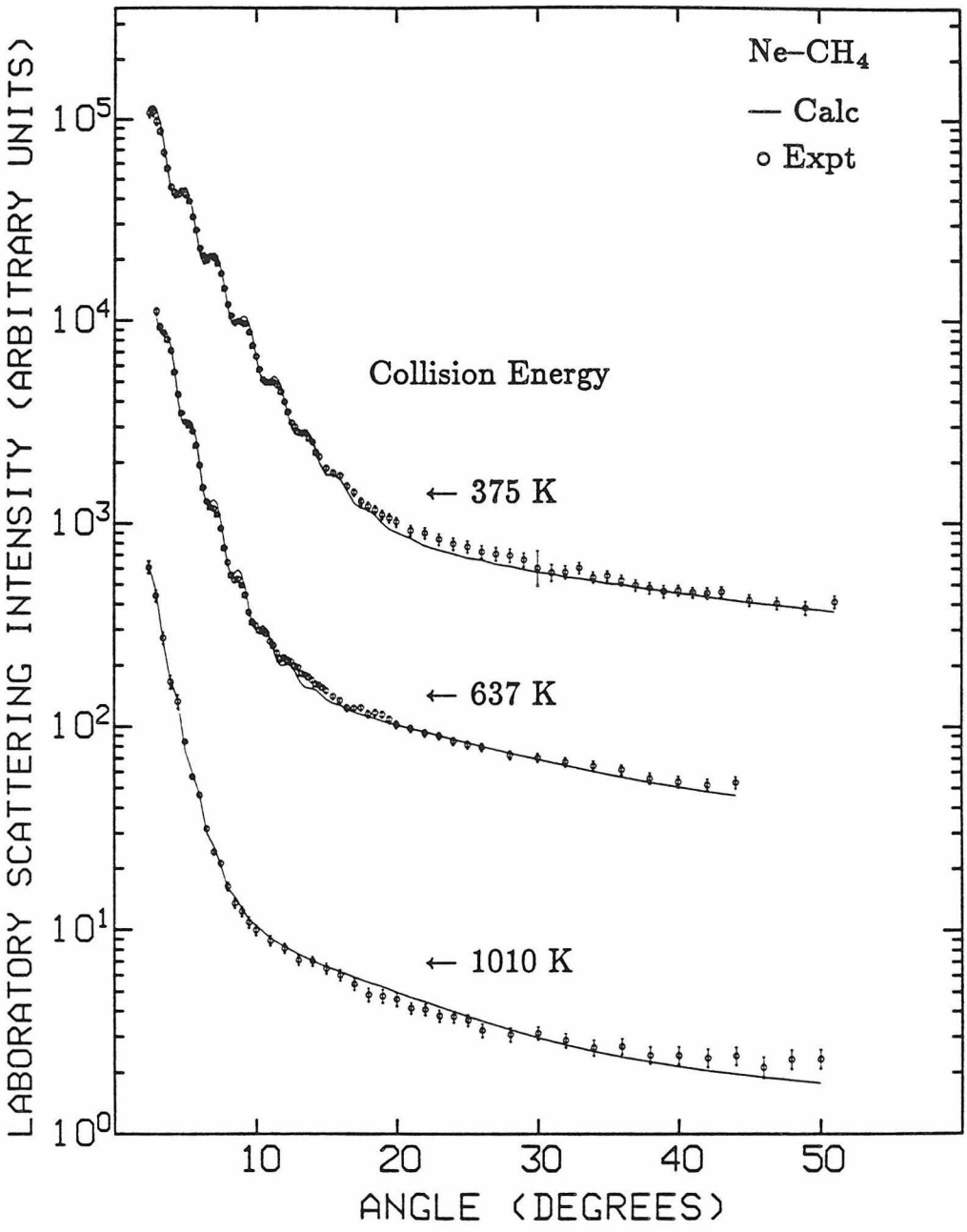

Figure 7. Neon-methane laboratory scattering distributions for all three collision energies as a function of laboratory angle, Θ. Solid lines are calculated using Potential A_{Ne}.

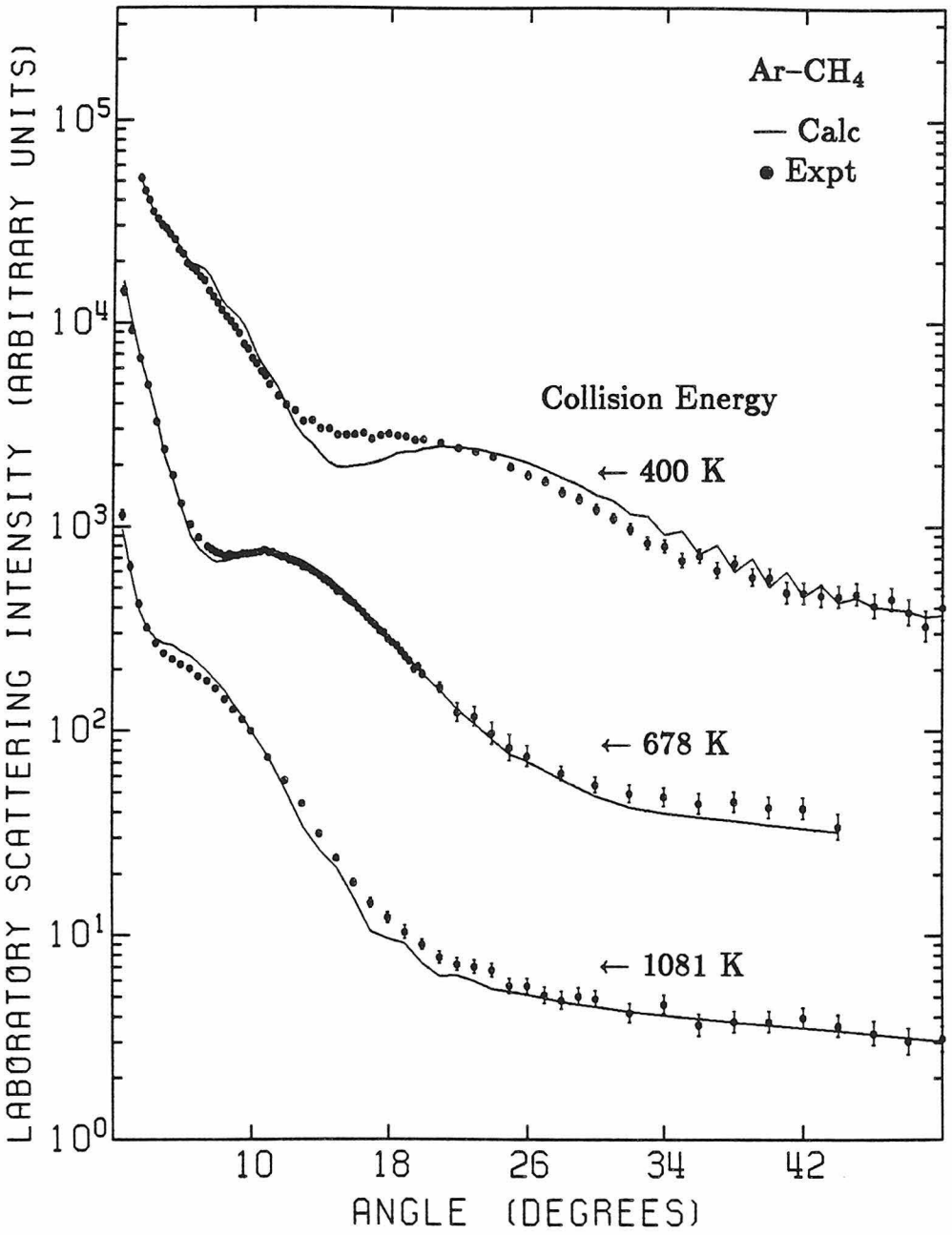

Figure 8. Argon-methane laboratory scattering distributions for all three collision energies as a function of laboratory angle, Θ. Solid lines are calculated using Potential A_{Ar}.

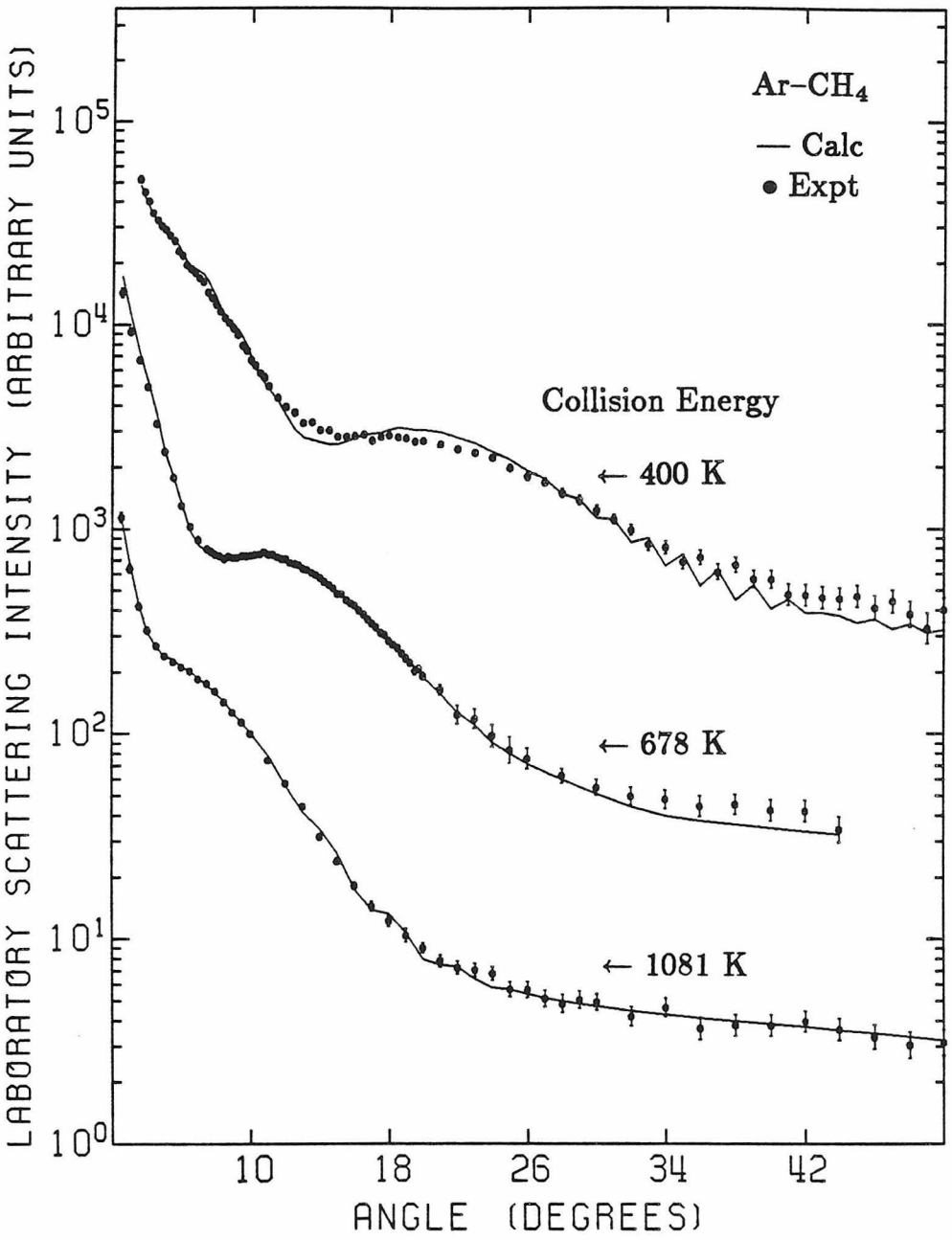

Figure 9. Argon-methane laboratory scattering distributions for all three collision energies as a function of laboratory angle, Θ. Solid lines are calculated using Potentials B_{Ar}, C_{Ar} and D_{Ar} for the 400 K, 678 K and 1081 K collision energies respectively.

In the argon-methane DCS's, diffraction oscillations were only resolved in the 400 K data in the area of the supernumerary rainbow maximum ($\sim$ 8°). The principal rainbow maxima are easily visible, however, at approximately 7°, 12°, and 20° for the 1081, 678, and 400 K scattering data respectively. Each of these features has been reproduced accurately by Potential A_{Ar}.

2.5 Discussion

It is evident from Figure 9 and Table 6 that the scattering from a single collision energy for argon-methane can be reproduced well, but not without sacrificing the fits to the other energies. This is probably caused by the anisotropy of the potential. Anisotropy in intermolecular interactions has been shown to damp the rainbow maxima and diffraction oscillations (these will hereafter be referred to as the "principal features") in the scattering compared to the calculated scattering from the spherical limit of the potential.[4a,26] In fitting each individual DCS we have forced our best spherical potential to fit those damped features, which may not be realistic behavior for either the spherical limit or the spherical average potential. Although we do not know quantitatively how large the well depth anisotropy is, qualitatively we would expect the maximum anisotropic deviations from our spherical potentials to be roughly proportional to the well depth of the potentials. The neon-methane scattering exhibits less damping because the collision energies are large relative to the well depth of the potential (the 375 K neon-methane data has roughly the same ratio of collision energy to well depth as the 1081 K argon-methane data). The relationship between the damping of the principal features and collision energy is easily observed in the argon-methane DCS's. As the collision

energy is decreased, the damping of the principal features is increased and the DCS's become more difficult to fit with a spherical potential. This implies that there is significant information about the anisotropy of the potential in this data, especially the 400 K argon-methane DCS. By using three DCS's to determine the potentials, we have avoided trying to fit the damped features of each individual DCS and concentrated on the correct positioning of the principal features of all three DCS's. We believe that this treatment gives a more accurate representation of the effective isotropic potential along with realistic estimates of the error involved.

The validity of the use of a spherical approximation for these systems has not been completely resolved. In the neon-methane case, the determined spherical potential reproduces all the data sets very accurately and therefore we feel that the spherical approximation is valid for this system. The fits to the DCS data of argon-methane are somewhat less pleasing, but the purpose of this paper is not to present a new isotropic argon-methane potential since an anisotropic potential has already been determined for this system.[6] Instead, the argon-methane result is presented mainly for comparison with the neon-methane, methane-methane,[5] and helium-methane[2] potentials. However, if the spherical approximation is adequate for a particular application, we feel that the argon-methane potential presented here is more accurate than previous isotropic potentials for the reasons to discussed above.

The improved accuracy of our potentials is evidenced by the deviations listed in Tables 5 and 6 for the previous best argon-methane potential and the neon-methane potential which has been determined by Buck *et al.* since the conclusion of

this study. The laboratory DCS's calculated using the spherical potentials of Buck *et al.* have also been presented in Figures 10 and 11 for neon-methane and argon-methane respectively. While the argon-methane data is represented reasonably well by the Buck *et al.* potential, major discrepancies are visible in the predictions of their neon-methane potential. These discrepancies cannot be attributed to the use of only the spherical part of their potential. The spherical part of their helium-methane and argon-methane potentials agree well with the effective spherical potential of Slankas *et al.*[2] for helium-methane and the effective spherical potential determined for argon-methane in this study. These potentials have been summarized in Table 7. It is clear that the Buck *et al.* value of ϵ for neon-methane is underestimated by roughly 16%. Considering that their data were all measured at energies of approximately 1000 K, this is not surprising since at that high an energy they could not resolve the rainbow maximum. However, their value of r_{min} is also significantly different from ours even though they have resolved diffraction oscillations. The period of the diffraction oscillations at that collision energy is such that a small error in r_{min} does not produce significant error in the positioning of the oscillations. In addition, the steep slope of the DCS caused by the underestimated well depth affects the diffraction oscillations by making their apparent maxima and minima shift to higher angles. This can be seen very clearly in Figure 10 in which their potential adequately reproduces the diffraction oscillations of the high energy data, but fails miserably as the period of those oscillations increases in the lower energy DCS's. A smaller value of r_{min} would increase the period of the oscillations predicted by their potential and align those oscillations with our experimental data.

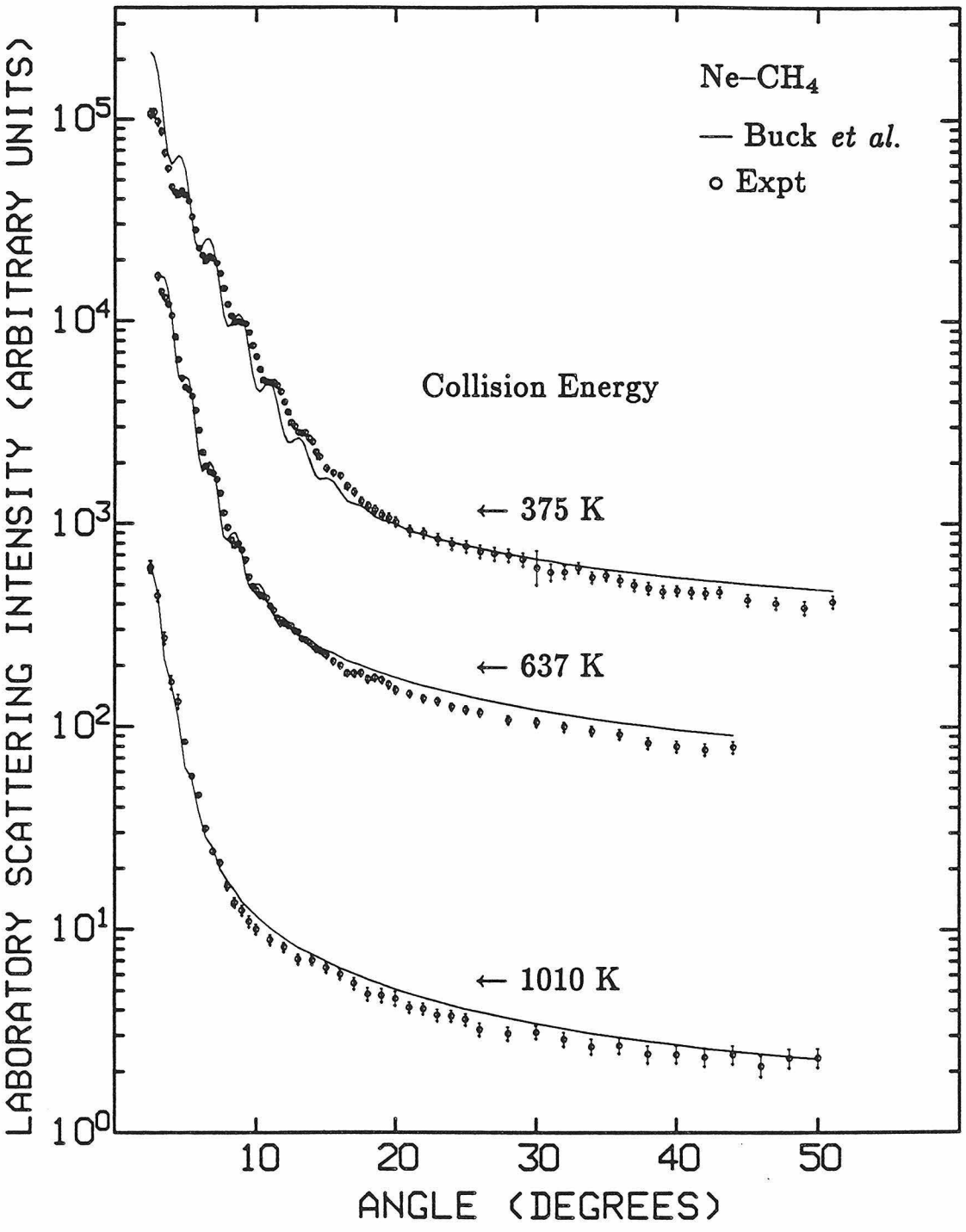

Figure 10. Neon-methane laboratory scattering distributions for all three collision energies as a function of laboratory angle, Θ. Solid lines calculated using the potential of Buck *et al.*[6]

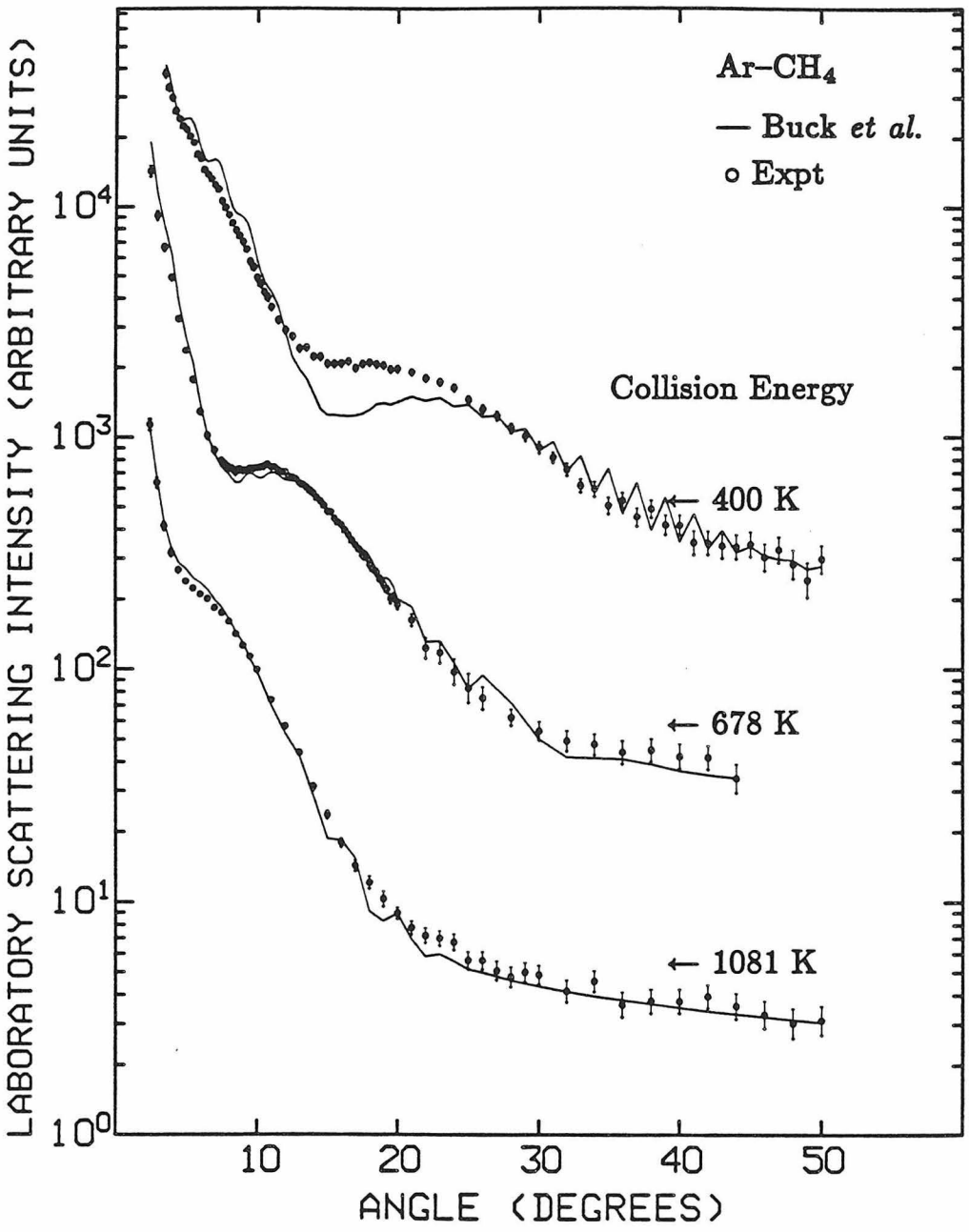

Figure 11. Argon-methane laboratory scattering distributions for all three collision energies as a function of laboratory angle, Θ. Solid lines calculated using the potential of Buck *et al.*[6]

Table 7. Comparison of helium-, neon- and argon-methane.

	effective spherical potential		spherical part of anisotropic potential	
	r_{min} (Å)	ϵ (K)	r_{min} (Å)	ϵ (K)
He–CH_4	$3.85 \pm .05$[a]	25.5 ± 2.3[a]	3.84[b]	25.5[b]
Ne–CH_4	$3.68 \pm .02$[c]	66 ± 4[c]	3.83[d]	55.7[d]
Ar–CH_4	$3.85 \pm .04$[c]	170 ± 8[c]	3.85[e]	170.6[e]

[a] Reference 2

[b] Reference 7

[c] This study

[d] Reference 25

[e] Reference 6

Thus, we feel that our potential is a more reliable estimate of the spherical part of the isotropic potential, and that our potential should be incorporated into their anisotropic potential for further study.

2.6 Conclusions

In this paper we have reported total differential cross sections determined at three collision energies each for the neon-methane and argon-methane systems. We have used these data along with literature data for viscosities and second virial coefficients to determine effective isotropic potentials for those systems. The neon-methane data is accurately reproduced by our spherical potential although poorly fit by the spherical part of the anisotropic potential reported by Buck *et al.* The argon-methane data, although affected by the anisotropy of the potential, is also well fit by a spherical potential. The deviation of the calculated scattering from the experimental scattering gives some indication of the anisotropy of the potential. This could eventually be used along with the energy loss spectra of Buck *et al.* to better determine the complete anisotropic potential, but until then, we present accurate isotropic potentials to use in modeling other, more complex interactions.

Acknowledgements

The authors wish to acknowledge Professor Yuan Lee of the University of California, Berkeley for providing inspiration, an elastic scattering program, and some equipment vital to the success of the experiment. We also wish to thank Professor Udo Buck of the Max Planck *Institut für Strömungsforschung* for providing preprints of his helium-methane and neon-methane papers.

References

[1] See, for example, G. Scoles, Ann. Rev. Phys. Chem. **31**, 81–96, (1980).

[2] See, for example, J.T. Slankas, M. Keil and A. Kuppermann, J. Chem. Phys. **70**, 1482–1491, (1979).

[3] R.T Pack, J.J. Valentini, and J.B. Cross, J. Chem. Phys. **77**, 5486–5499, (1982).

[4] (a) R.T Pack, Chem. Phys. Lett. **55**, 197–201, (1978);
(b) G. Rotzol and A. Lübbert, J. Chem. Phys. **71**, 2275–2281, (1979).

[5] B.P. Reid, M.J. O'Loughlin, and R.K. Sparks, J. Chem. Phys., in press.

[6] U. Buck, J. Schleusener, D.J. Malik, and D. Secrest, J. Chem. Phys. **74**, 1707–1717, (1981).

[7] U. Buck, M. Faubel, K.H. Kohl, A. Kohlase, V. Staemmler, Mol. Phys., in press.

[8] See, for example, N.L. Allinger, Adv. Phys. Org. Chem. **13**, 1–82, (1976).

[9] See, for example, R.P. Bell, J. Chem. Soc. Faraday Trans. II **76**, 954–960, (1980).

[10] J. Kestin and S.T. Ro, Ber. Bunsenges. Phys. Chem. **78**, 20–24, (1974).

[11] J.H. Dymond and E.B. Smith, *The Virial Coefficients of Pure Gases and Mixtures* (Oxford University Press, Oxford, England, 1980).

[12] R.K. Sparks, *Ph.D. Thesis* (University of California, Berkeley, 1979).

[13] Y.T. Lee, J.D. McDonald, P.R. LeBreton, and D.R. Herschbach, Rev. Sci. Instrum. **40**, 1402–1408, (1969).

[14] U. Buck, Rev. Mod. Phys. **46**, 369–389, (1974).

[15] M. Keil, J.T. Slankas, and A. Kuppermann, J. Chem. Phys. **70**, 482–503, (1979).

[16] P.E. Siska, J.M. Parson, T.P. Schafer, and Y.T. Lee, J. Chem. Phys. **55**, 5762–5770, (1971).

[17] M.F. Vernon, *Ph.D. Thesis* (University of California, Berkeley, 1983).

[18] See, for example, M.S. Child, *Molecular Collision Theory* (Academic Press, New York, 1974).

[19] J.S. Cohen, J. Chem. Phys. **68**, 1841–1843, (1978).

[20] (a) J.O. Hirschfelder, C.F. Curtis, and R.B. Bird, *Molecular Theory of Gases and Liquids* (John Wiley and Sons, New York, 1954);
(b) S. Chapman and T.G. Cowling, *The Mathematical Theory of Non-Uniform Gases* (Cambridge University Press, New York, 1952).

[21] G.A. Parker and R.T Pack, J. Chem. Phys. **68**, 1585–1601, (1978).

[22] G.C. Maitland and E.B. Smith, J. Chem. Eng. Data **17**, 150–156, (1972).

[23] R.T Pack, J.J. Valentini, C.H. Becker, R.J. Buss, and Y.T. Lee, J. Chem. Phys. **77**, 5475–5485, (1982).

[24] A. Dalgarno, Adv. Chem. Phys. **12**, 143–166, (1967).

[25] U. Buck, A. Kohlase, D. Secrest, T. Phillips, G. Scoles, and F. Grein, Mol. Phys., in press.

[26] R.J. Cross, Jr., J. Chem. Phys. **52**, 5703–5707, (1970).

Chapter 3

Helium-Chlorine and Neon-Chlorine
Anisotropic Interaction Potentials
from
Total Differential Cross Sections

3.1 Introduction

One of the ultimate goals of Chemical Physicists is the understanding of the processes by which energy is redistributed within a molecule. Knowledge of these processes is important if techniques such as laser selective chemistry are ever to become viable. The nature of chemical bonds is such that the amount of energy required to rupture one bond in a molecule is normally in a regime in which the number and density of available internal states is too large for the actual dynamics of the dissociation to be theoretically treatable or even experimentally discernable. More mechanistic information can be gained by observing the dissociation of very weak bonds such as those found in van der Waals molecules.

A simple model system used in recent years to study intramolecular energy redistribution is the photodissociation of molecular complexes comprised of a rare gas atom bound to a diatomic molecule.[1] In particular, the rare gas-halogen van der Waals molecules have received much attention because of their rich visible and near-UV absorption spectra. The original studies on helium-iodine[2] and the successful prediction of many of the observed phenomena by the "energy gap"[3] and "momentum gap"[4] theories imply that investigations of energy redistribution in these systems is tractable and can be fruitful. One of the major predictions of these theories is that some van der Waals species should have unusually long lifetimes with internal energies well in excess of the van der Waals bond strength.[3,4] Recently, Brinza *et al.*[5] have confirmed this prediction with the observation of the long-lived metastable neon-chlorine van

der Waals molecule. This qualitative agreement between experiment and theory suggests that more quantitative treatments should be attempted. Unfortunately, quantitative treatments are hindered by the lack of knowledge about either the ground or the excited state potential energy surfaces of these species.

To assist in the complete understanding of these systems, we have used crossed molecular beams total differential cross sections and the infinite order sudden (IOS) approximation to determine anisotropic potential energy surfaces for ground state chlorine ($^1\Sigma_{g^+}$) with helium and neon. These total differential cross sections have been shown to be sensitive to the anisotropy of the potential through the damping of the quantum oscillations.[6] The observed damping was considerably more extensive than the amount of damping which could be attributed to finite apparatus resolution. Thus, we expect our data to place significant constraints on the complete potential surface.

The IOS approximation and conditions for its validity have been discussed in Chapter 1. For the IOS approximation to be acceptable, the conditions of validity for both the energy sudden (ES) and centrifugal sudden (CS) approximations should be met. At the collision energies used in this study, the CS approximation will be valid for $\Delta j \leq 32$ for neon-chlorine collisions and $\Delta j \leq 29$ for helium-chlorine collisions. The validity of the ES approximation can be tested using Equation (26) of Chapter 1. For the worst case, neon-chlorine at 464 K collision energy, Δj is restricted to be less than about 30. Since we have only sampled the total differential cross section at relatively small center-of-mass angles, these

conditions are expected to be maintained although perhaps only marginally at the wider angles.

3.2 Experimental

Total differential cross sections for neon-chlorine and helium-chlorine were measured using the crossed molecular beams apparatus described extensively in the previous chapters. The detector aperture, the beam collimating apertures and the overall layout of the beam sources was left unaltered from the previous experiment and are summarized in Figure 1 of Chapter 2. The total differential cross sections were measured at two collision energies for each scattering pair.

The chlorine beam was produced by the expansion of pure chlorine (UHP) through a quartz nozzle with a 75 μm orifice. The forelines of both the beam source and differential chambers required in-line liquid nitrogen traps to prevent contamination of the mechanical pump oil. The stagnation pressure of the chlorine within the nozzle was adjusted until the percentage of dimers (mass 142 ± 2 amu) in the beam was less than .25.

The rare gas beams were produced by utilizing the liquid nitrogen cooled beam source described in Chapter 1. For both helium and neon, two stagnation temperatures were used to create different collision conditions. The velocity distributions of both the rare gas and the chlorine beams were measured using the time-of-flight technique. Experimental velocity distributions were then fit to the functional form,

$$P(v) \propto v^2 e^{-s^2(v-v_0)^2/v_0^2}, \qquad (1)$$

to determine the best values of s, the speed ratio, and v_0, the flow velocity. The values of s and v_0 determined in this manner, along with the known values of the stagnation temperature and pressures, are summarized in Tables 1 and 2 for helium-chlorine and neon-chlorine respectively.

Laboratory angular intensity distributions were measured by detecting the scattered rare gas beam. For neon-chlorine, the quadrupole mass filter was set to pass only ^{20}Ne obviating the need to account for ^{22}Ne in the calculations. The intensity at each angle was measured relative to a chosen reference angle. By returning to that reference angle after 5 to 10 other angles have been measured, any possible long term drift in intensity can be accounted for. The reference angle normalized scattering intensity was measured 4 to 8 times at each angle and the resulting normalized intensities were averaged. The measured distributions with estimates of the corresponding uncertainties are tabulated in Appendix C.

3.3 Analysis

The determination of an anisotropic potential energy surface from total differential cross sections can only be accomplished using a trial and error fitting procedure. This entails selection of a functional form for the potential which has several adjustable parameters and the calculation of the center-of-mass differential cross sections that would result from that potential. The center-of-mass differential cross sections are then transformed to the laboratory reference frame, while accounting for the finite resolution of the apparatus, so that they can be compared directly with the experimentally measured laboratory scattering intensities. The potential parameters are then adjusted until good agreement

Table 1: Beam source characteristics for helium-chlorine at two collision energies.

	collision energy	
characteristics	340 K	511 K
gas	$He \| \| Cl_2$	$He \| \| Cl_2$
stagnation pressure(torr)	1225||1120	1225||1100
stagnation temperature(K)	119||303	195||303
velocity(10^4 cm/sec)	11.14||5.02	14.12||5.02
speed ratio	15.1||7.0	11.7||7.0

Table 2: Beam source characteristics for neon-chlorine at two collision energies.

	collision energy	
characteristics	464 K	612 K
gas	$Ne \| \| Cl_2$	$Ne \| \| Cl_2$
stagnation pressure(torr)	1225||1120	1225||1100
stagnation temperature(K)	119||303	195||303
velocity(10^4 cm/sec)	4.92||5.02	6.33||5.02
speed ratio	16.4||7.0	16.8||7.0

is found between the calculated and experimental quantities. Where possible, parameters which have been determined by some other means are not adjusted in the fitting procedure. For instance, the van der Waals dispersion terms were fixed at their theoretical estimates. The formulation of the anisotropic potential, the calculation of the dispersion constants, the details of the calculation of laboratory total differential cross sections from an anisotropic potential, and the procedure used to determine the potential parameters are presented in the following sections.

3.3.1 Potential

The exact form of the complete anisotropic potential energy surface is not understood, but a cut through that surface at any given angle, γ, is expected to produce a potential function similar in form to those for central field potentials. Therefore, it is not unreasonable to assume that the anisotropic surfaces can be approximated by a linear combination or expansion in terms of central field potential forms. Many such potentials have been proposed[7] including multicenter potentials, Legendre expansions of isotropic potentials, *i.e.*, $V(r,\gamma) = \sum_{n=0}^{\infty} V_n(r) P_n(cos\gamma)$ and Legendre expansions of the parameters of isotropic potentials.

Multicenter potentials, in which equivalent isotropic potentials are centered on each of the two chlorine atoms were tried initially because the number of parameters used in this form is invitingly small (equivalent to one isotropic potential). However, these two center potentials were not flexible enough to reproduce the scattering results and it became clear that a third center, located

on the bond, would have to be added. Unfortunately, the third center would double the number of adjustable parameters, and it was decided that other more convenient and flexible forms should be tried first. The Legendre parameter expansion was thought to be the most flexible (for the same number of adjustable parameters) of the remaining two forms and was used exclusively in the remainder of the investigation.

In the Legendre parameter expansion, an analytical form of a central potential is selected and its parameters are then expanded in terms of the Legendre polynomials for the cosine of the orientation angle between the atom and the diatom (γ in Figure 4 of Chapter 1). For example, the well depth, ϵ, is expanded as

$$\epsilon(\gamma) = \epsilon_0 + \epsilon_2 P_2(cos\gamma), \tag{1}$$

where the expansion has been truncated after P_2, and only the even terms are included because of the symmetry of the potential. The analytical form of the isotropic potential was initially chosen to be the Morse-Morse-spline-van der Waals (MMSV) potential form discussed in the previous chapter. However, since there were no bulk property data to fit simultaneously, and it was found that the laboratory scattering intensities were insensitive to the repulsive wall Morse function, the form was reduced to an MSV Potential.[8]

Although the MSV works well for isotropic potentials, the introduction of anisotropy often produced unphysical undulations in the spline at some values of γ. To avoid these undulations, we introduced an alternative formulation which replaced the spline with a damped average of the Morse and van der Waals

functions. Written in reduced form ($x = r/r_m$, $f(x) = U(x)/\epsilon$, and $\beta = \alpha r_m$), the Morse potential is

$$f_m(x) = e^{\beta(1-x)}\left[e^{\beta(1-x)} - 2\right], \tag{2}$$

the van der Waals dispersion potential is

$$f_v(x) = -c_6 x^{-6} - c_8 x^{-8}, \tag{3}$$

and the Morse-damped average-van der Waals (MDV) piecewise potential is

$$f(x) = \begin{cases} f_m(x) & \text{if } x \leq x_i \\ f_v(x) + [f_m(x) - f_v(x)]\, e^{-\rho(x_i - x)^2} & \text{if } x > x_i \end{cases}, \tag{4}$$

in which ρ is the damping factor usually kept at 3 or 4, and $x_i = 1 + \beta^{-1} \ln 2$ is the inflection point of the Morse potential. In Equation (3), $c_i = C_i/\epsilon r_m^i$ where the C_i are the long range van der Waals dispersion coefficients whose estimation is described in the next subsection. Each of the parameters, $\epsilon(\gamma)$, $r_m(\gamma)$, $\beta(\gamma)$, $C_6(\gamma)$ and $C_8(\gamma)$ have been expanded as in Equation (1). In some potentials, an additional $r_4 P_4(cos\gamma)$ term was included in the expansion of $r_m(\gamma)$.

3.3.2 Estimation of Anisotropic Dispersion Terms

The long range dispersion forces between molecules are well understood and can be calculated rather accurately. This is fortunate because most laboratory differential cross sections are measured in energy regimes in which they are relatively insensitive to the long range dispersion forces. Accurate calculation of the dispersion forces requires knowledge of the energies of transition from the ground to all excited electronic states for both particles and the oscillator

strengths for those transitions.[9] In practice, approximate methods are generally used to estimate these numbers.

An estimate of $C_6(\gamma)$ for an atom-diatom interaction can be derived using the Drude oscillater model and is found to be,[10]

$$C_6(\gamma) = \frac{1}{6}\left[3(B_{\|} - B_{\perp})cos^2(\gamma) + 5B_{\perp} + B_{\|}\right] \ , \tag{5}$$

where

$$B_{\perp} = \frac{3}{2}\frac{e\hbar}{m_e^{1/2}}\frac{\alpha_R\alpha_{\perp}}{(\alpha_R/N_R)^{1/2} + (\alpha_{\perp}/N_{Cl})^{1/2}} \ , \tag{6}$$

and

$$B_{\|} = \frac{3}{2}\frac{e\hbar}{m_e^{1/2}}\frac{\alpha_R\alpha_{\|}}{(\alpha_R/N_R)^{1/2} + (\alpha_{\|}/N_{Cl})^{1/2}} \ . \tag{7}$$

In Equations (6) and (7), $\alpha_{\perp}$ and $\alpha_{\|}$ are the perpendicular and parallel polarizabilities of the diatom, α_R is the polarizability of the atom, and N_i is the number of valence shell electrons for species i. The similarity of Equation (5) to the Legendre parameter expansion,

$$C_6(\gamma) = C_{6_0} + C_{6_2}(\frac{3}{2}cos^2\gamma - \frac{1}{2}), \tag{8}$$

allows us to determine C_{6_0} and C_{6_2} by equating the coefficients of $cos^2\gamma$ in Equations (5) and (8). The result is that

$$C_{6_0} = \frac{1}{3}(2B_{\perp} + B_{\|}), \text{ and } C_{6_2} = \frac{1}{3}(B_{\|} - B_{\perp}). \tag{9}$$

The values of C_{6_0} and C_{6_2} calculated in this manner are tabulated in Table 3 along with the α_i, N_i and B_i used in their determination.

Table 3: Anisotropic dispersion terms: C_6

	He-Cl_2	Ne-Cl_2
$\alpha_R^{\dagger}$ (Å^3)	.205	.395
N_R	2	8
$\alpha_{\perp}^{\star}$ (Å^3)	3.62	3.62
$\alpha_{\parallel}^{\star}$ (Å^3)	6.60	6.60
N_{Cl_2}	14	14
B_1 (kcal/mol Å^6)	324.5	663.7
B_2 (kcal/mol Å^6)	487.0	1039
C_{6_0} (kcal/mol Å^6)	379	789
C_{6_2} (kcal/mol Å^6)	54	125

† Reference 11

⋆ Reference 12

Formulas for the approximation of $C_8(\gamma)$ are not nearly as well developed, but fortunately the measured scattering intensities are virtually unaffected by the value chosen for C_{8_0} or C_{8_2}.[13] Thus, since any reasonable estimate would suffice, the simplistic two-level oscillator formula has been used;[12]

$$C_8 = \frac{45}{8}\frac{IP_a IP_b}{e^2}\alpha_a\alpha_b\left[\frac{\alpha_a IP_a}{2IP_a + IP_b} + \frac{\alpha_b IP_b}{IP_a + 2IP_b}\right] \tag{10}$$

in which IP_i is the ionization potential for particle i. Values of $C_{8_\perp}$ and $C_{8_\parallel}$ were calculated from Equation (10) using $\alpha_\perp$ and $\alpha_\parallel$ respectively. Those values were then used to estimate an effective C_{8_0} and an upperbound on C_{8_2}. By comparison with the more accurate C_6 terms, C_{8_2} was felt to be overestimated by this procedure and was reduced by the ratio of the C_{6_i} term, determined as before, to the C_{6_i} term determined using a similar two-level oscillator formula. The values of C_{8_0} and C_{8_2} calculated using this model are tabulated in Table 4 along with the ionization potentials and the actual C_{8_2} used in the differential cross section calculations.

3.3.3 Total Differential Cross Sections

Laboratory scattering intensities were calculated using the computer program described in Chapter 1 which was modified to utilize the IOS approximation for anisotropic potentials. The IOS formula for total differential cross sections is

$$I(\theta) = \frac{1}{2}\int_{-1}^{1} I(\gamma,\theta)dcos\gamma \ , \tag{11}$$

Table 4: Anisotropic dispersion terms: C_8

	$He\text{-}Cl_2$	$Ne\text{-}Cl_2$
IP_{Rg} † (kcal/mol)	565	497
IP_{Cl_2} ‡ (kcal/mol)	265	265
$C_{8_\perp}$ (kcal/mol Å^8)	1810	3480
$C_{8_\parallel}$ (kcal/mol Å^8)	5774	10820
C_{8_0} (kcal/mol Å^8)	3131	5927
C_{8_2} (kcal/mol Å^8)	2643	4893
C_{8_2} ⋆ (kcal/mol Å^8)	900	3000

† Reference 14

‡ Reference 15

⋆ Value selected for use.

in which $I(\gamma,\theta)$ is the differential cross section for an isotropic potential formed by taking a section through $U(r,\gamma)$ at angle γ. This integral can be evaluated efficiently using Gauss-Legendre quadrature, *i.e.*,

$$I(\theta) \approx \frac{1}{2}\sum_{i=1}^{n} w_i I(\gamma_i,\theta) \tag{12}$$

in which $\gamma_i = cos^{-1}x_i$ and x_i and w_i are the usual quadrature points and weights for Gauss-Legendre integration.[16] The number of quadrature points used in Equation (12) was varied until an increase in n produced no change in I(θ). Convergence was found to occur at 12 quadrature points. Because of the symmetry of the diatomic, it was only necessary to calculate the center-of-mass differential cross sections at 6 values of γ. The only modification to our existing simulation program was the addition of a "do loop" over the angular quadrature points in which first $U(r,\gamma_i)$ was determined and then the laboratory scattering intensities were calculated for that potential as in Chapter 1.

Since the sensitivity of the total differential cross section to the anisotropy of the potential is in the form of damping of the rainbow and diffraction oscillations,[6] great care was taken to assure that we could distinguish between the damping due to the apparatus resolution and the damping as a result of the anisotropy. The number of quadrature points in the velocity, collision volume and detector acceptance integrations were all adjusted independently until $I(\theta)$ was converged for each. The number of phase shifts that were used in the partial wave analysis was determined in a similar convergence test. The actual number of phase shifts that were used along with the apparatus resolution quadrature values are tabulated in Table 5.

Table 5: Number of phase shifts and quadrature points.

	$He\text{-}Cl_2$		$Ne\text{-}Cl_2$	
	340 K	511 K	464 K	612 K
η_{max} [a]	150	120	200	200
$I(v_{rg})$ [b]	7	7	5	5
$J(v_{Cl_2})$ [c]	5	5	5	5
$L(y)$ [d]	3	3	3	3
$M(x)$ [e]	1	1	1	1
$N(\Omega_d)$ [f]	3	3	3	3

[a] η_{max} is the number of phase shifts used.

[b] $I(v_{rg})$ is the number of quadrature points for the rare gas velocity distribution.

[c] $J(v_{Cl_2})$ is the number of quadrature points for the chlorine velocity distribution.

[d] $L(y)$ is the number of quadrature points across the width of the chlorine beam.

[e] $M(x)$ is the number of quadrature points across the width of the rare gas beam.

[f] $N(\Omega_d)$ is the number of quadrature points across the detector width.

For each differential cross section, the phase shifts were calculated using the JWKB approximation and eight point Gauss-Mehler quadrature. The phase shifts were calculated at 10 energies equally spaced from the lowest to the highest values of the relative kinetic energy as defined by the beam quadrature points. Four point Legendre interpolation was then used to estimate the phase shifts at the desired values of the relative kinetic energy. For helium-chlorine, the results of this method were compared with the laboratory scattering intensities predicted using an exact quantum mechanical phase shift calculation and found to be equivalent within the experimental uncertainty.

The phase shifts were not recalculated for the different collision volume points. For each collision volume point the phase shifts for the relative kinetic energy of the most probable collision volume point were used. After all the laboratory differential cross sections were calculated and summed, the calculated intensities were scaled to minimize the sum of the squares of the differences between the calculated and experimental values divided by the experimental uncertainty.

3.3.4 Fitting and Uncertainties

One of the major disadvantages of any trial and error cross section fitting routine is that even isotropic potentials determined in this manner are not necessarily unique.[17] This problem is aggravated by the inclusion of anisotropy in the potential form because in the resulting parameterization, the potential parameters are invariably strongly correlated. When using only one kind of information (total differential cross section, etc.) the determined potential may

fit the data very well but not be an accurate representation of the true potential. Thus, it is usually advantageous to force constraints on the potential by including data from other types of measurements.

There are several sources of additional information about the neon-chlorine potential. High resolution spectroscopic studies of the photodissociation of the neon-chlorine van der Waals molcule have determined that the expectation value for $r(90°)$ is 3.565 ± 0.035 Å for the $X,v''=1$ state of chlorine.[18] This expectation value should not be confused with the actual value of $r_m(90°)$ which is expected to be slightly smaller. Preliminary results of a concurrent study on the inelastic scattering, energy loss spectra of neon-chlorine indicate a value of $\Delta r_m = r_m(0°) - r_m(90°)$ of approximately 1.5 Å for a realistic potential function. However, these energy loss spectra are really only sensitive to the difference in r for the anisotropic potential in the region of $U(r)=\frac{1}{2}\mu v_{rel}^2$, and the value of Δr in that region is also affected to some extent by the well depth and shape anisotropy. Indeed, Hoffbauer *et al.*[19] have estimated the anisotropy of the argon-chlorine potential using a purely classical rigid ellipsoid model to be Δr_{re}=.95 Å. At first glance Δr_m=1.5 Å and Δr_{re}=.95 Å may seem inconsistent, but the realistic potential used to determine Δr_m=1.5 Å actually has a Δr value of approximately 1 Å for equipotential contours near the reduced collision energies used in both studies. Also, while one might expect that the anisotropy would be determined by only the chlorine molecule and be independent of the rare gas atom, studies of the anisotropic potential surfaces of methane[20] and sulphur hexafluoride[21] with a series of rare gas atoms indicate that for those systems the anisotropy is

dependent on the rare gas atom. However, in each of those cases the observed trend indicates that the variation in the anisotropy depends on the ability of the atom to "fit" in between the three atoms comprising a face of the molecule. The chlorine molecule is not expected to exhibit a large variation in the anisotropy of its interaction with the various rare gases because it has no size selective sites. Thus, we felt justified in restraining the anisotropy in all of our chlorine potentials to remain close to $\Delta r_m \approx 1.5$ Å.

With both $r_m(0°)$ and $r_m(90°)$ (through Δr_m) both fixed, we introduced an additional $r_4 P_4(cos\gamma)$ term in the parameter expansion of $r(\gamma)$. This allowed the potential to be more flexible at those value of γ between 0° and 90°. For the initial fits, only r_2 was allowed to vary independently with r_4 being determined by the values of Δr_m and r_2, *e.g.*,

$$r_4 = (\Delta r_m - \frac{3}{2} r_2)\frac{8}{5}. \tag{13}$$

With these constraints on $r(\gamma)$, the parameters ϵ, ϵ_2, r_2, α $(= \beta/r_m)$ and α_2 $(= \beta_2/r_m)$ were adjusted in a least squares fitting program until the dimensionless mean square deviation as defined in Chapter 1 had been minimized. The values of $r_m(0°)$ and Δr_m were then fine tuned by allowing one, the other, or both to vary along with the other parameters. The dispersion terms remained fixed at their theoretical estimates at all times.

For helium-chlorine, the constraints were somewhat more tenuous. Low resolution spectroscopic studies are reproduced equally well by expectation values of $r(90°)$ anywhere from 3.4 Å to 4.0 Å.[22] Also, no energy loss spectra are

available to obtain a value of Δr_m. However, as discussed above, the anisotropy in r is expected to be similar to neon-chlorine. Thus, $r_m(90°)$ and Δr_m were initially constrained to be 3.6 Å and 1.5 Å respectively. The remaining parameters with the exception of the dispersion terms were optimized before allowing $r_m(90°)$ to vary.

In addition, the standard method was employed to determine another estimate of the potential. This "standard" method involves using the parameters from an isotropic potential fit to the total differential cross sections as a first approximation of the zero order terms of the Legendre parameter expansion. The anisotropy parameters, ϵ_2, r_2, and β_2, are then allowed to vary until the dimensionless deviation has been minimized. Finally, all of the parameters are allowed to vary to produce the best fit. This method essentially constrains the potential parameters to find a minimum in the χ^2 hypersurface in the vicinity of the isotropic potential. In the absence of any other information about the potential surface, *e.g.*, energy loss spectra, state-to-state cross sections, etc., this method is the only acceptable way to determine an anisotropic potential from total differential cross sections.

3.4 Results

3.4.1 Isotropic Potentials

In order to obtain qualitative estimates of the zero order terms in the Legendre parameter expansion, the total differential cross sections were initially fit using an isotropic MDV potential. In these fits, the C_{i_0} dispersion terms were

kept fixed at their theoretical values, the C_{i_2} terms were set to zero, and ρ was held at 4. The potential parameters which produced the minimum dimensionless deviations were:

1) ϵ=54.9 K, r_m=4.113 Å, and α=2.90 Å^{-1} for helium-chlorine, and

2) ϵ=77.5 K, r_m=4.156 Å, and α=2.19 Å^{-1} for neon-chlorine.

The laboratory scattering intensities calculated using these potentials are shown in Figures 1 and 2. Although the periods of the calculated diffraction oscillations are correct in each data set, the amplitude of those oscillations is significantly larger than the experimentally observed amplitude. The principal rainbow maxima are well positioned in the fit to the neon-chlorine data, but no rainbow maxima have been resolved and for helium-chlorine and the well depth appears to be too deep in comparison to the neon-chlorine well depth. Neither set of experimental cross sections is fit well by the isotropic potentials. To improve the fit it is necessary to introduce anisotropy into the potential.

3.4.2 Neon-Chlorine

The anisotropic MDV potential parameters, including a three-term expansion of $r(\gamma)$ (see Equation 13), are presented in Table 6 for the four potentials which best fit the data within the constraints outlined in 3.3.4. In each case, those parameters which were not allowed to vary in the least squares fit are highlighted by stars. The rms dimensionless deviations which resulted from these potentials are tabulated in Table 7. Potential D_{Ne} produced the lowest overall rms deviation and is therefore assumed to be our most accurate representation of the complete anisotropic potential. A contour plot of Potential

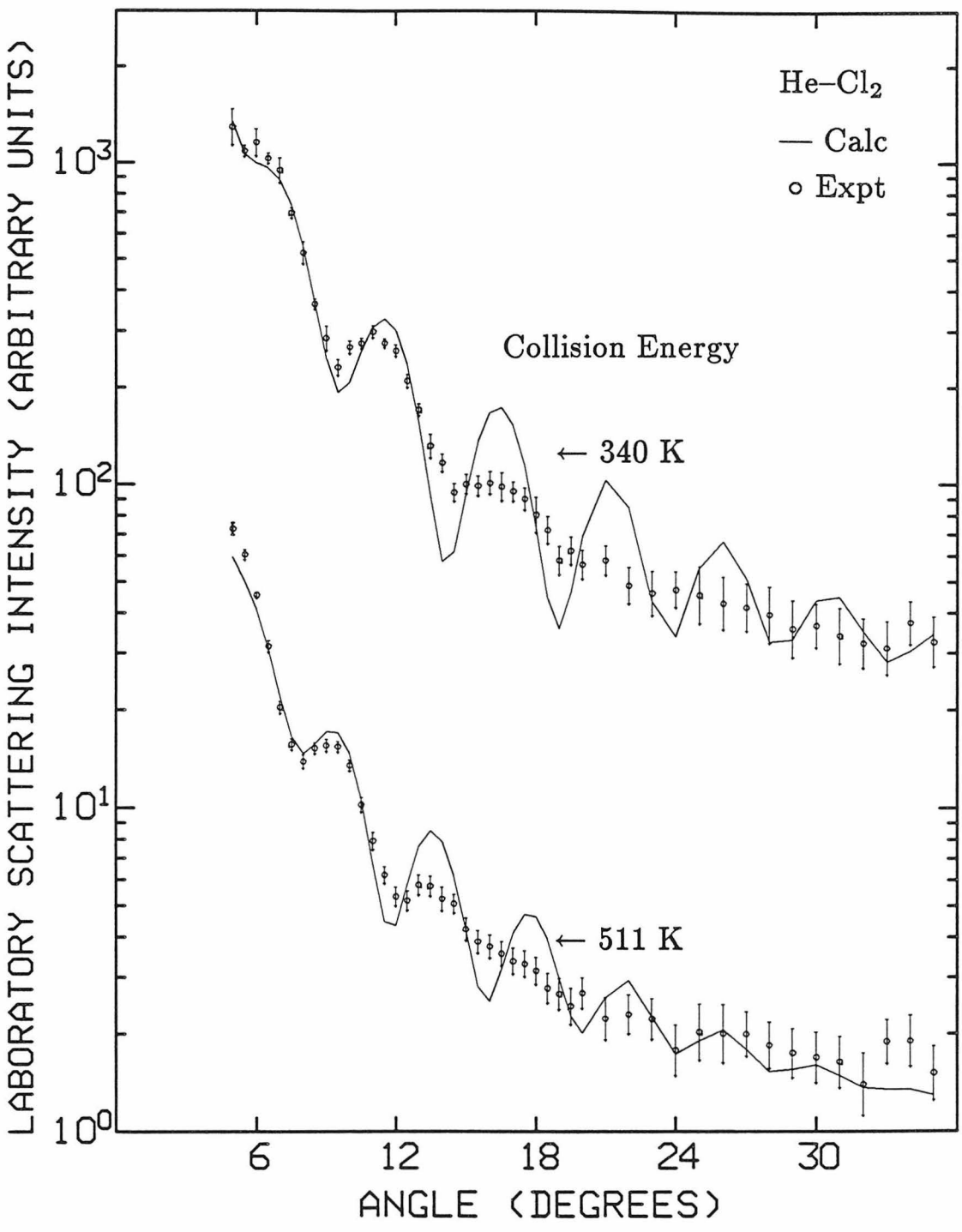

Figure 1. Helium-chlorine laboratory scattering distributions for both collision energies as a function of laboratory angle, Θ. Solid lines are calculated using the best isotropic potential.

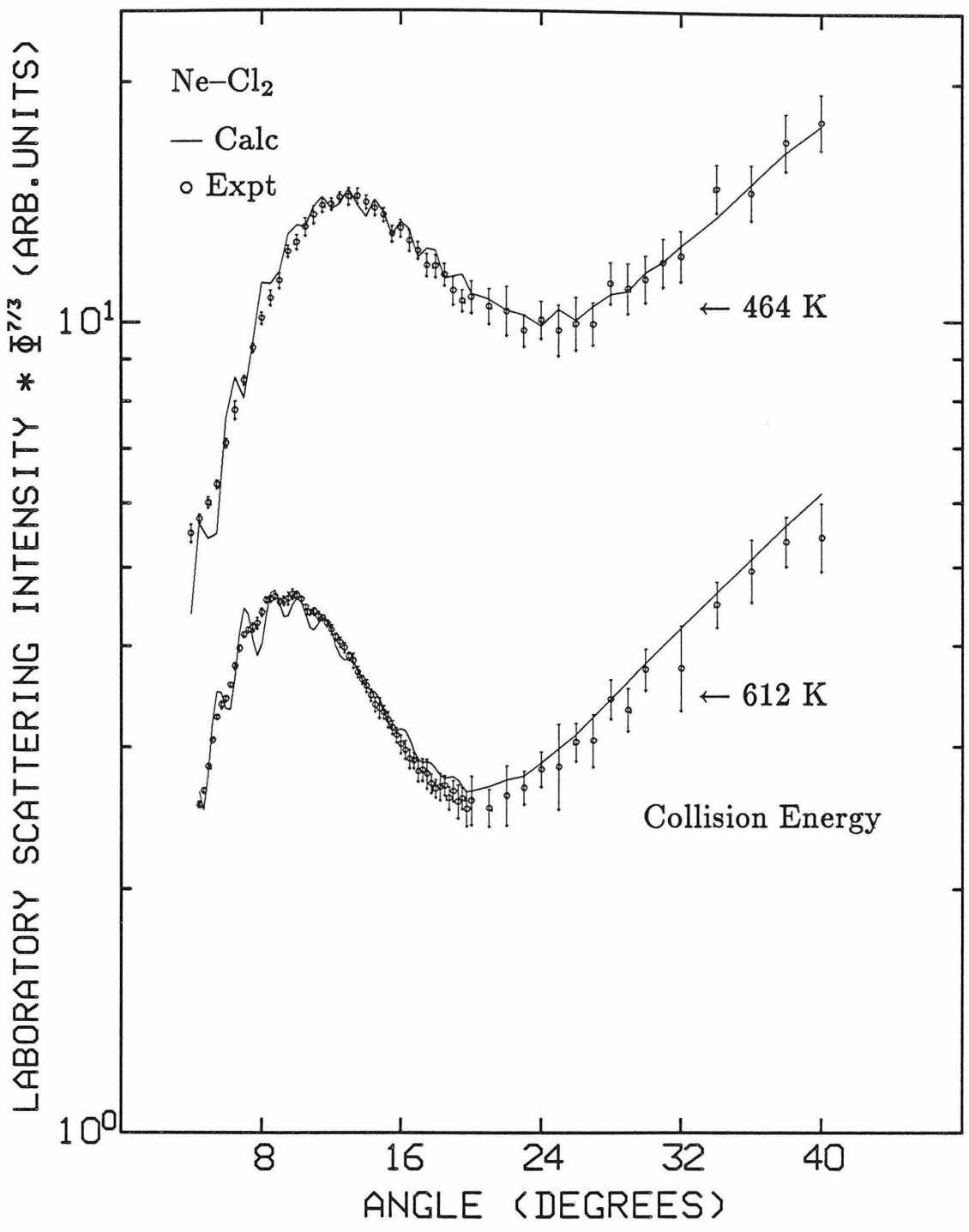

Figure 2. Neon-chlorine laboratory scattering distributions times $\Theta^{7/3}$ for both collision energies as a function of laboratory angle, Θ. Solid lines are calculated using the best isotropic potential.

Table 6. MDV potential parameters determined for neon-chlorine.

	Pot A_{Ne}	Pot B_{Ne}	Pot C_{Ne}	Pot D_{Ne}
ϵ_0 (K)	71.5	72.3	76.0	77.4
ϵ_2 (K)	-56.9	-55.4	-50.3	-48.8
$r_m(90°)$ (Å)	3.54*	3.54*	3.488	3.484
r_2 (Å)	1.43	1.50	1.49	1.61
Δr (Å)	1.50*	1.64	1.50*	1.76
α_0 (Å^{-1})	1.72	1.72	1.66	1.66
α_2 (Å^{-1})	—	—	-.325	-.383
ρ	4	4	4	4

⋆ Parameter not allowed to change from initial estimate.

Table 7. Rms dimensionless deviations for the neon-chlorine potentials of Table 6.

	Pot A_{Ne}	Pot B_{Ne}	Pot C_{Ne}	Pot D_{Ne}
δ (464 K)	1.37	1.37	1.16	1.12
δ (612 K)	0.87	0.87	0.87	0.85
δ Total	1.15	1.15	1.01	0.99

D_{Ne} is shown in Figure 3, and sections through that potential at 0° and 90° are shown in Figure 4 along with the best fit isotropic potential. The laboratory total differential cross sections calculated using this potential are shown with the experimental data in Figure 5. Each has been scaled by $\Theta^{7/3}$ to accentuate the rainbow maxima and the diffraction oscillations.

All of the best fit potentials accurately reproduce the rainbow maximum at each collision energy and the diffraction oscillations which are only well resolved in the 612 K collision energy data. The only real difference is in the quality of the fit to the large angle ($\Theta \geq 20°$) scattering. However, those angles are the most affected by the velocity defect from the inelastic processes and probably should not be used to differentiate between potentials. Also, the comparison of contour plots for each of the potentials indicates that the differences in the potentials are mainly in the region of small γ. In this region, the total differential cross sections are nearly insensitive to changes in the potential.

3.4.3 Helium-Chlorine

The anisotropic MDV potential parameters, including a three-term expansion of $r(\gamma)$, are presented in Table 8 for the three potentials which best fit the data within the following constraints. Potential A_{He} was formed by keeping Δr_m fixed at the value of 1.5 Å. Since the potential which produced the lowest deviation for neon-chlorine had Δr_m= 1.76 Å, this value was fixed while the other parameters varied to produce Potential B_{He}. In Potential C_{He} all the parameters were allowed to vary from their values in Potential B_{He}. Also included in Table 8 is Potential D_{He} which was determined with the initial constraint that the zero

Figure 3. Neon-chlorine intermolecular potential. Equipotential contours of Potential D_{Ne} in units of K.

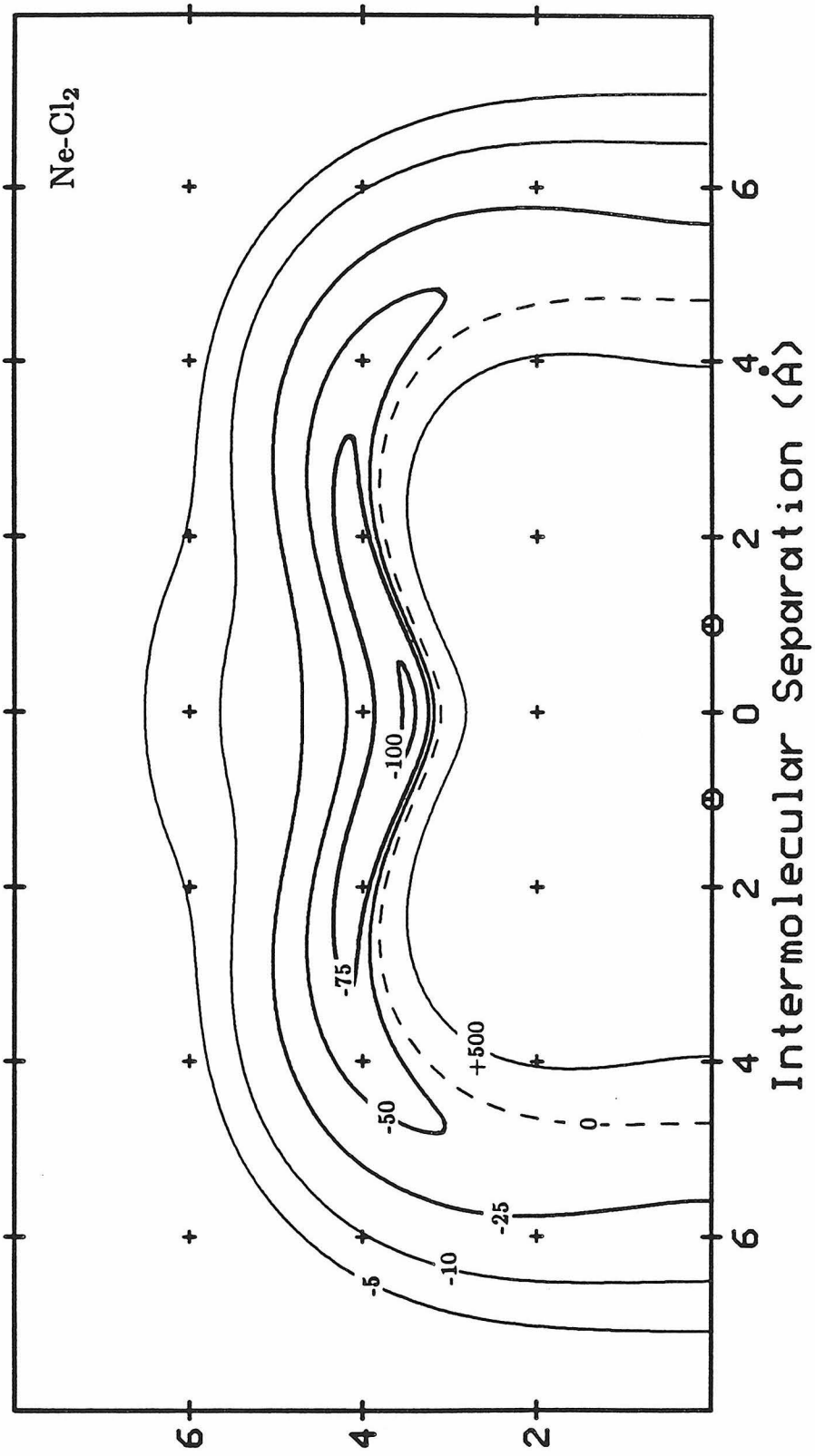
Ne-Cl2
-5
-10
-25
-50
-75
-100
+500
0
6
4
2
0
2
4
6
Intermolecular Separation (Å)

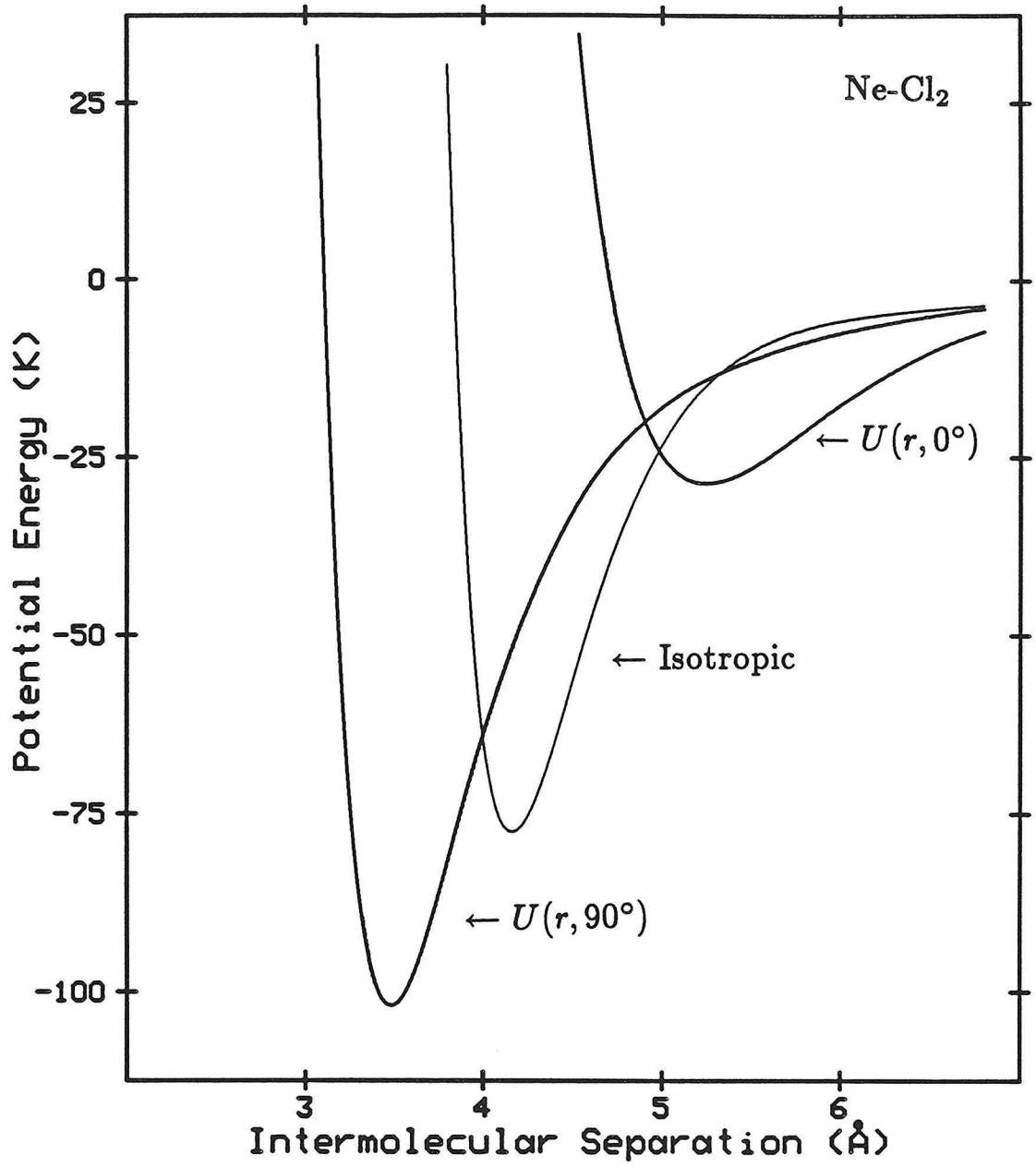

Figure 4. Neon-chlorine intermolecular potential. Sections through Potential D_{Ne} at $\gamma = 0°$ and 90°. The best isotropic potential is also shown.

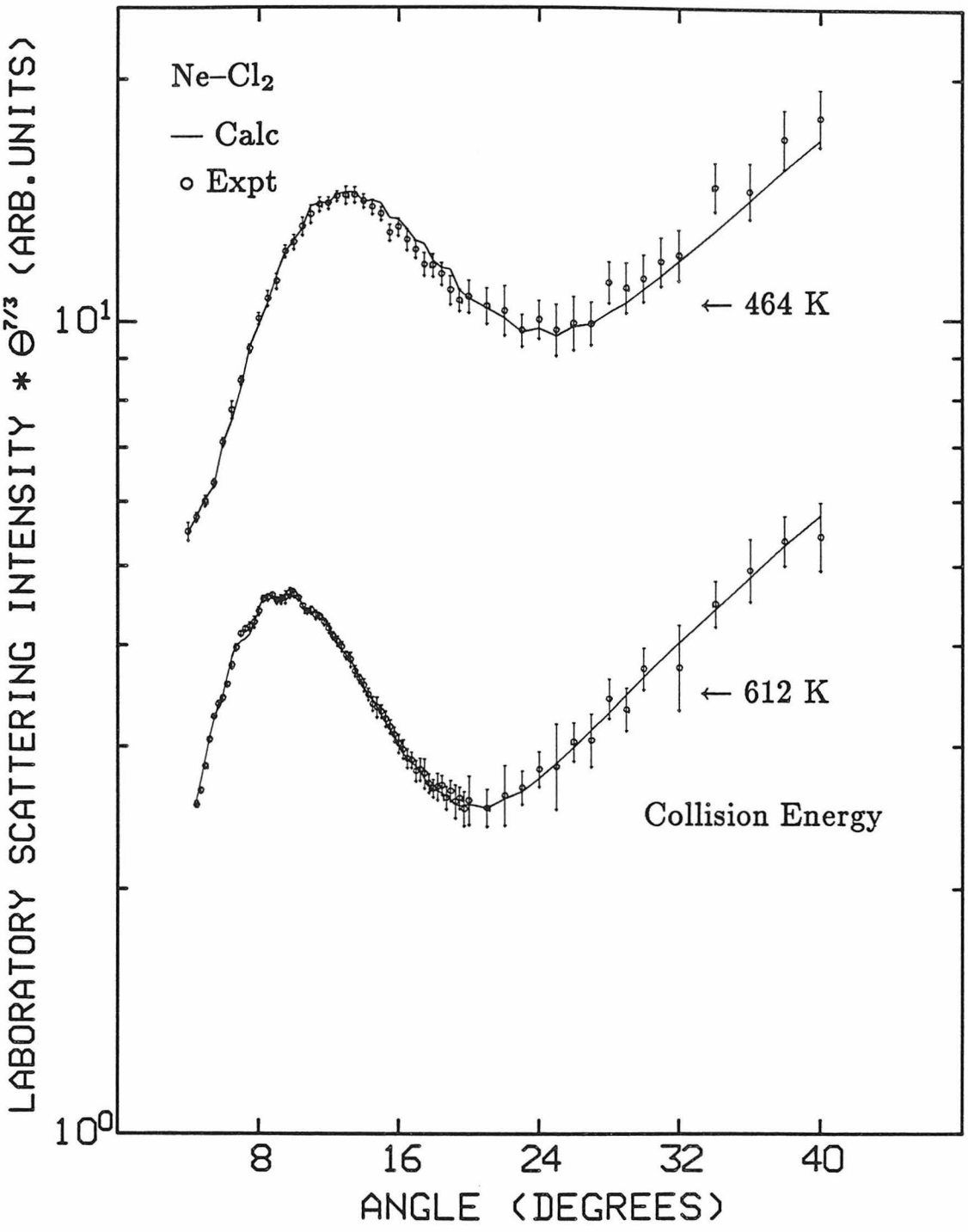

Figure 5. Neon-chlorine laboratory scattering distributions times $\Theta^{7/3}$ for both collision energies as a function of laboratory angle, Θ. Solid lines are calculated using Potential D_{Ne}.

Table 8. MDV potential parameters determined for helium-chlorine.

	Pot A_{He}	Pot B_{He}	Pot C_{He}	Pot D_{He}
ϵ_0 (K)	32.7	33.2	33.7	59.9
ϵ_2 (K)	-7.0	-5.0	-11.6	-7.5
$r_m(90°)$ (Å)	3.806	3.845	3.838	3.612
r_2 (Å)	1.070	1.235	1.803	0.656
Δr (Å)	1.50*	1.76*	2.737	$1.5r_2$
α_0 ($Å^{-1}$)	2.13	2.19	2.283	11.04†
α_2 ($Å^{-1}$)	1.35	1.46	1.448	-4.55†
ρ	4	4	4	4

⋆ Parameter not allowed to change from initial estimate.

† These values are dimensionless, *i.e.*, $\beta(\gamma) = \alpha(\gamma)r_m(\gamma)$.

Table 9. Rms dimensionless deviations for the helium-chlorine potentials of Table 8.

	Pot A_{He}	Pot B_{He}	Pot C_{He}	Pot D_{He}
δ (464 K)	1.03	0.93	0.74	1.52
δ (612 K)	1.09	0.92	0.81	0.99
δ Total	1.06	0.92	0.77	1.29

order terms be equivalent to the parameters of the best isotropic potential. The rms dimensionless deviations which resulted from these potentials are tabulated in Table 9.

Although Potential C_{He} had the lowest rms dimensionless deviation, the value of Δr_m for that potential is not reasonably close to the value from the energy loss experiments. Potentials A_{He} and B_{He} also have unphysical behavior at the wide angles caused by the large positive values of α_2. The value of $\alpha(90°)$ becomes much larger than is reasonable and although Δr_m has the expected value, Δr for an equipotential curve at higher energy actually becomes larger than Δr_m. This is illustrated in Figure 6 by the sections through Potential B_{He} at $\gamma = 0°$ and $\gamma = 90°$. A contour plot of Potential B_{He} is also presented in Figure 7. Conversely, Potential D_{He} would appear to underestimate the value of Δr_m. Sections through Potential D_{He} at $\gamma = 0°$ and $\gamma = 90°$ are shown in Figure 8 and a contour plot is presented in Figure 9.

In can be seen that Potential D_{He} is consistent with the best isotropic potential while Potential B_{He} (Figure 6) has a significantly shallower average well depth. Both potentials accurately reproduce the data from both collision energies. The laboratory total differential cross sections calculated using both potentials are displayed in Figure 10 along with the experimental data. The major difference in the quality of fit is found at the large angles ($\Theta > 20°$). The calculated cross sections are expected to be a little low at these angles because of neglect of contributions from inelastic scattering processes to the measured cross sections. Although the IOS approximation accounts for the inelastic transitions

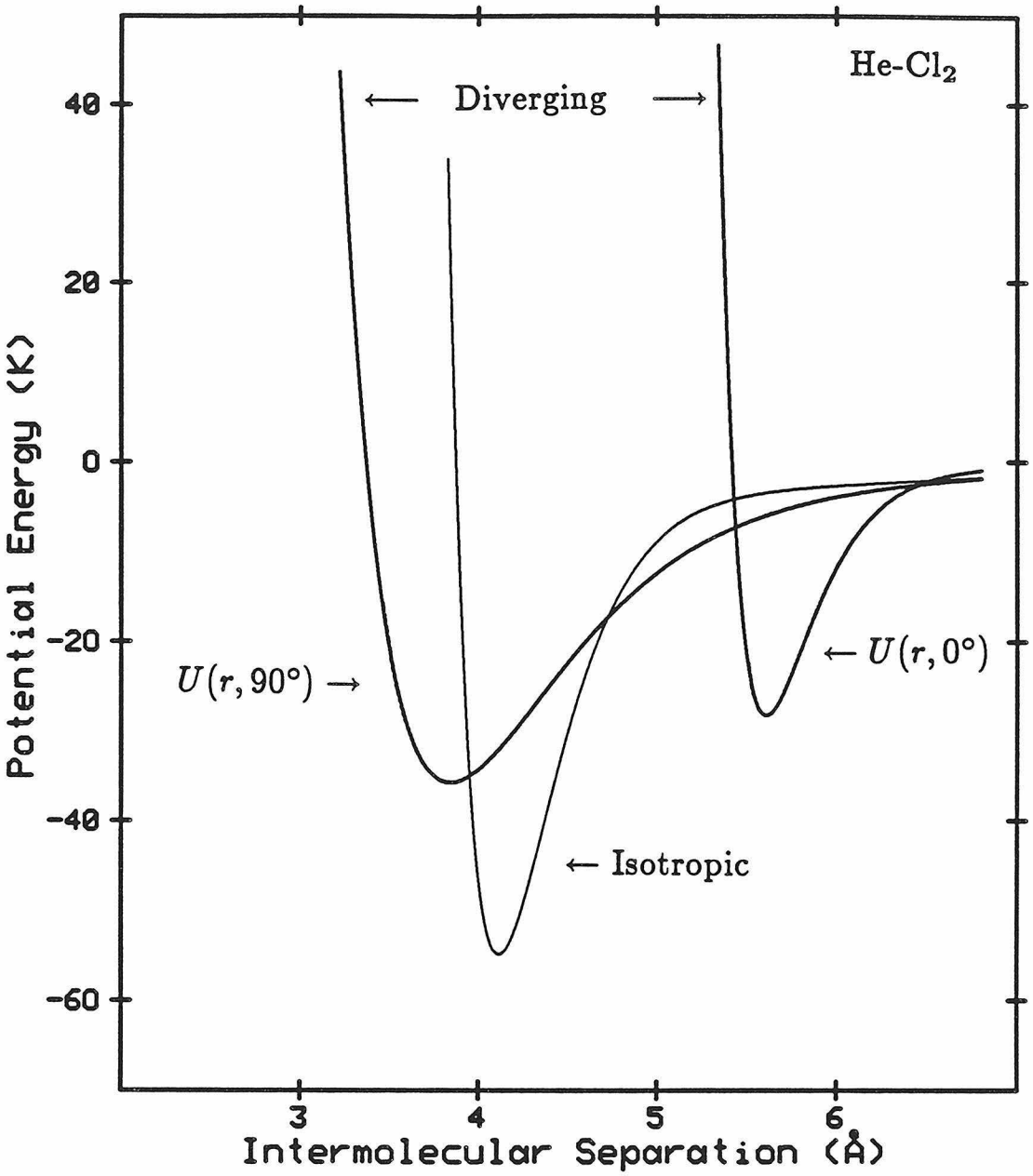

Figure 6. Helium-chlorine intermolecular potential. Sections through Potential B_{He} at $\gamma = 0°$ and 90°. The best isotropic potential is also shown.

Figure 7. Helium-chlorine intermolecular potential. Equipotential contours of Potential B_{He} in units of K.

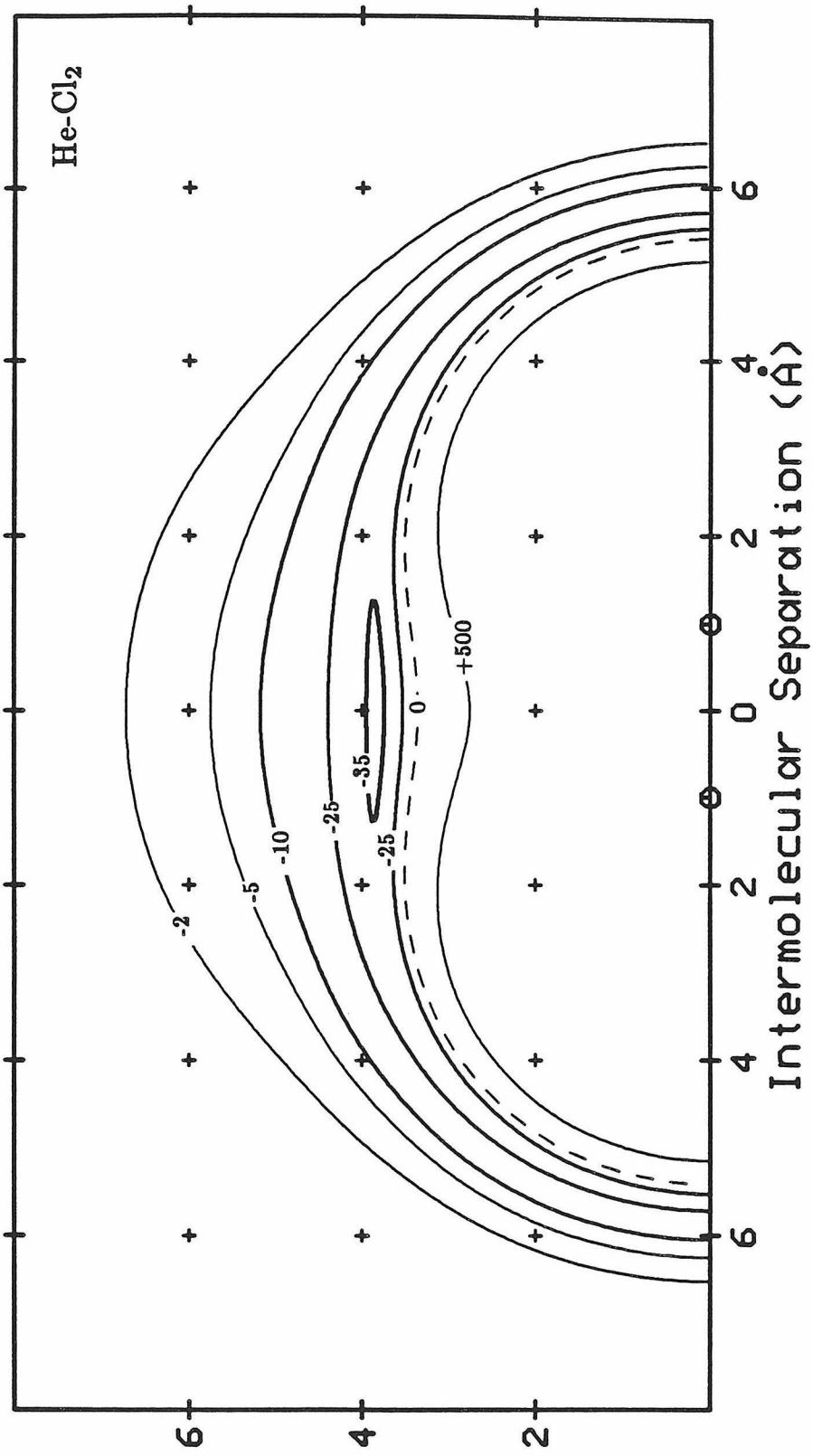
He-Cl2
-2
-5
-10
-25
-35
-25
0
+500
6
4
2
0
2
4
6
Intermolecular Separation (Å)

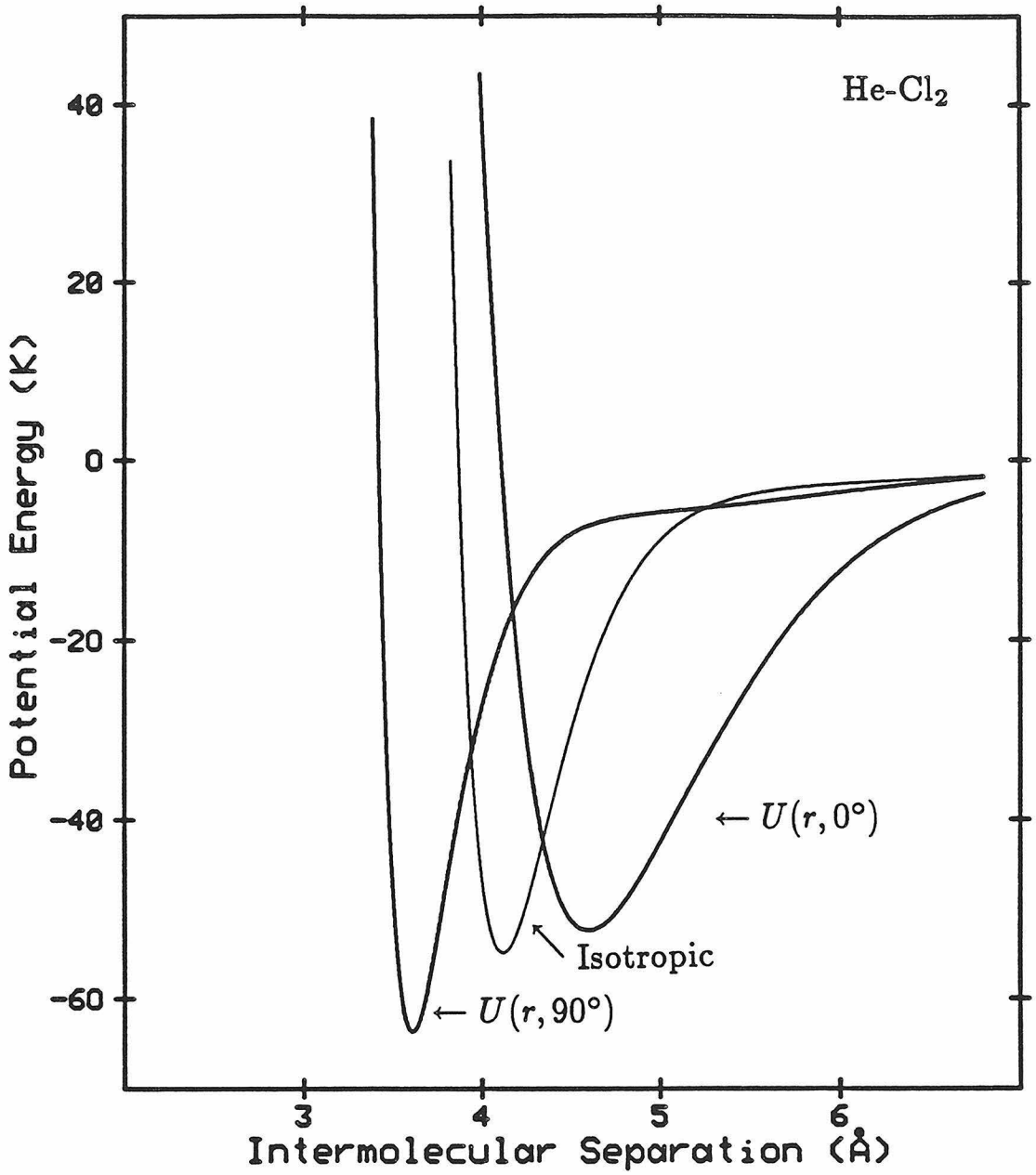

Figure 8. Helium-chlorine intermolecular potential. Sections through Potential D_{He} at $\gamma = 0°$ and 90°. The best isotropic potential is also shown.

Figure 9. Helium-chlorine intermolecular potential. Equipotential contours of Potential D_{He} in units of K.

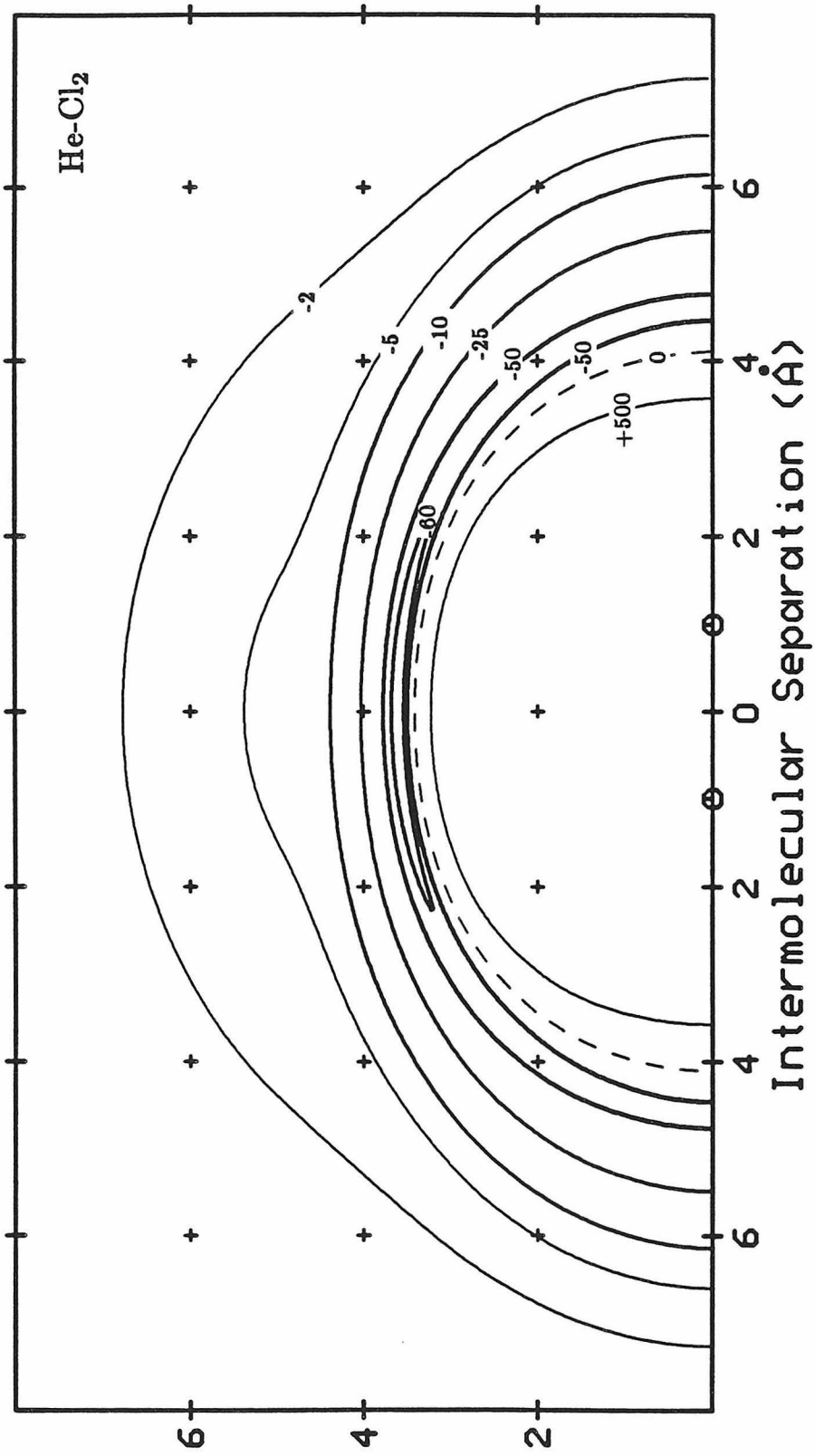
He-Cl2
-2
-5
-10
-25
-50
-50
0
+500
-60
6
4
2
0
2
4
6
Intermolecular Separation (Å)

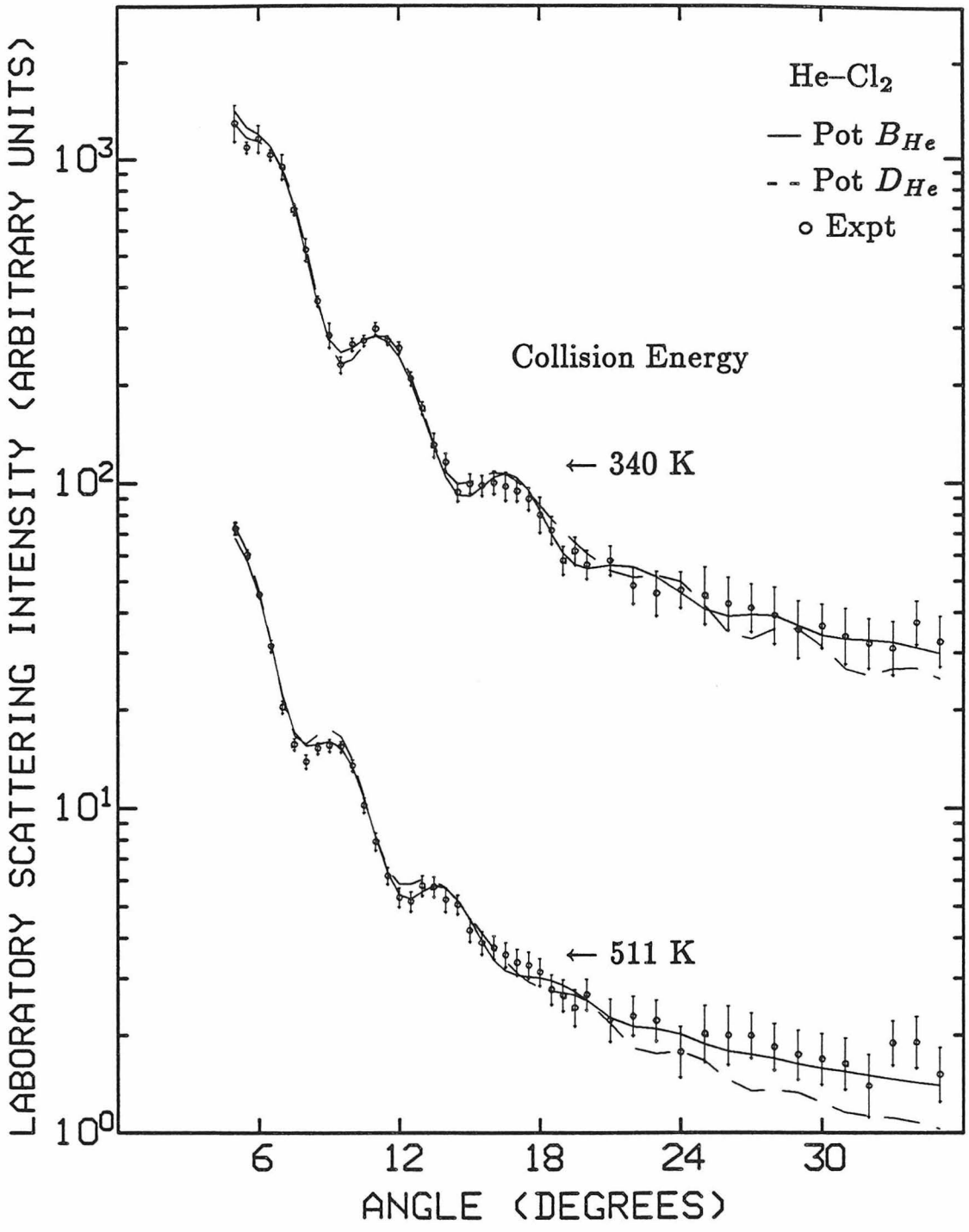

Figure 10. Helium-chlorine laboratory scattering distributions for both collision energies as a function of laboratory angle, Θ. Solid lines are calculated using Potential B_{He} (—) and Potential D_{He} (- - -).

in general, the error arises in the transformation of the center-of-mass differential cross sections to the laboratory reference frame as elastic scattering cross sections. Since the calculated scattering is expected to be slightly in error, it is not clear that there can be any distinction between these potentials on the basis of the dimensionless deviations alone.

3.5 Discussion

3.5.1 Neon-Chlorine

One of the important facets of the IOS total differential cross section formula in Equation (11) is that the cross sections for the individual γ are effectively weighted by $sin\gamma$ (since $dcos\gamma = -sin\gamma d\gamma$). Thus, the differential cross section for $\gamma = 0°$ has no effect at all on the total differential cross section. In fact, 50% of the contribution to the total differential cross section is from $60° \leq \gamma \leq 90°$. Our only knowledge of the potential at small γ is from extrapolation of the assumed potential form fit essentially to the large γ. A true representation of the potential surface would require a larger number of Legendre parameter expansion terms, but there is not enough information in the data to justify using more than 5 or 6 adjustable parameters. As a result, $U(r,\gamma)$ for small γ is never well defined by this type of experiment alone.

The differences in the potentials listed in Tables 6 are largely a result of variations in the small γ region of the potentials. For instance, although the values of ϵ_0 and ϵ_2 for neon-chlorine vary by as much 6 K and 8 K respectively, the value of $\epsilon(90°) = \epsilon_0 - \frac{1}{2}\epsilon_2$ is constant within 2 K. Thus, as long as the use of these

potentials is restricted to the area about $\gamma = 90°$, the neon-chlorine potentials should be reasonably accurate. Since this is the region of the potential surface which is assumed to be the most important in the photodissociation studies, the neon-chlorine potential determined in this study should make a significant contribution to the elucidation of the dynamics involved in that dissociation.

Of the potentials listed in Table 6, Potentials C_{Ne} and D_{Ne} probably have the most accurate values of $r_m(90°)$. The initial guess of $r_m(90°) = 3.54$ Å significantly underestimated the difference between the actual expectation value of r for $v = 0$ and the position of the well minimum. A one-dimensional Schrödinger equation solver was used to calculate a hypothetical vibrational wavefunction along $U(r, 90°)$. This approximation gives a value of $\langle r \rangle_{v=0}$ of 3.585 Å for Potential D_{Ne} and $\langle r \rangle_{v=0}$ of 3.642 Å for Potential A_{Ne}. The value of $\langle r \rangle_{v=0}$ for Potential D_{Ne} agrees very well with the measured value of Evard *et al*,[18] 3.565 ± .035 Å.

The well depths of the potentials are also in good agreement with what is known about similar potentials from spectroscopic studies. Blazy *et al.*[23] measured the binding energy of neon-iodine($^3\Pi_{0^+_u}$) van der Waals molecules by observing the closing of the I_2 $\Delta v = -1$ dissociation channel, *i.e.*, at which value of v the energy of one vibrational quantum in the iodine bond is smaller than the van der Waals bond energy. They then used other features of their spectra and many assumptions to estimate the binding energy, D_0, and the well depth, D_e, of the ground state complex at $\gamma = 90°$. The values they reported are 73.5 ± 1.2 cm^{-1}(106 ± 3 K) for D_0 and 85.5 ± 1.0 cm^{-1} (123 ± 2 K) for

D_e. In a similar manner, Swartz *et al.*[24] estimated D_0 for neon-bromine($^3\Pi_{0_u^+}$) and used that value to estimate D_0 for the ground state complex. The binding energy of neon-bromine($^1\Sigma_{0_g^+}$) was found to be nearly identical to that of neon-iodine although no estimate of the well depth could be made. These values are compared with the well depth determined in this study for $\gamma = 90°$ in Table 10. Also included in Table 10 are the known well depths for the interaction of neon with the rare gases, Ar, Kr, and Xe, which, to a first approximation, correspond to the halogen atoms, Cl, Br, and I, respectively. It has been popular to assume that the potential for $R-X_2$ could be approximated by the two center sum of the corresponding $R-R_X$ potential, where R is the rare gas atom, X_2 is the halogen diatom, and R_X is the rare gas atom which corresponds to the halogen atoms. Table 10 clearly shows that this procedure would lead to well depths which would be much too large for all of the neon-halogen van der Waals molecules with the well depth for neon-chlorine being overestimated by as much as 40%. However, the overall trend in well depth as a function of atomic number does follow the corresponding rare gas-rare gas trend.

3.5.2 Helium-Chlorine

Unlike the neon-chlorine potentials, the helium-chlorine potentials are not all similar at $\gamma = 90°$. In fact, $\epsilon(90°)$ is almost a factor of two larger for Potential D_{He} than for Potential B_{He}. The range of these two potentials are also quite different, with Potential B_{He} having a $r_m(90°)$ of 3.845 Å and a Δr_m of 1.76 Å and Potential D_{He} having a $r_m(90°)$ of 3.612 Å and a Δr_m of 0.984 Å. Both of these values of $r_m(90°)$ are in qualitative agreement with the spectroscopic value

Table 10. Comparison of neon-halogen well depths ($\gamma = 90°$) in units of K.

	D_0†	D_e‡	ϵ_{rg}♭
Ne–I_2	106[a]	123[a]	75.0[b]
Ne–Br_2	105[c]	—	74.5[b]
Ne–Cl_2	—	101.5[d]	72.0[b]

† Well depth minus zero point energy.

‡ Well depth at $\gamma = 90°$ ($\epsilon(90°)$).

♭ Well depth for neon with Xe, Kr, and Ar corresponding to I_2, Br_2, and Cl_2.

a Reference 23

b Reference 25

c Reference 24

d This study

of Cline *et al.*,[22] with the smaller value being more centrally located within the range of values they have determined. However, it should be noted that their values were determined assuming that the helium-chlorine van der Waals molecule is a rigid rotor with the helium located on the perpendicular bisector of the chlorine bond. The small amount of anisotropy in the well depth of either of our potentials (see Figures 7 and 9) indicates that there should be significant freedom of motion for the helium atom and a rigid rotor is probably not a very good model. Thus, the range of values of Cline *et al.* should not be used to differentiate between these potentials.

The correct value of Δr_m is equally ambiguous. In Potential B_{He}, Δr_m was fixed at the same value of Δr_m as the best neon-chlorine potential, but the value of α_2 makes that potential have too large an anisotropy at higher energies on the potential surface. Potential D_{He} has a value of Δr_m which is 37% smaller than the original value estimated from the neon-chlorine energy loss spectra and this value becomes much smaller at higher energy (see the +500 K contour of Figure 9). Thus, neither potential has a similar range anisotropy to the neon-chlorine potential, but as was stated in the neon-chlorine discussion, the total differential cross sections are insensitive to the potential in the region about $\gamma = 0°$ so either potential could still be accurate about $\gamma = 90°$.

Similarly, the disparate values for the well depth are difficult to explain. The well depth of the helium-chlorine potential is impossible to determine conclusively from the experimental data because a well defined rainbow maximum (like those in the neon-chlorine data of Figure 5) cannot be resolved at these energies. One

possible way to differentiate between the two values is by comparison with other potentials. A comparison of our potentials at $\gamma = 90°$ with the helium-iodine results of Blazy *et al.*[23] and the helium-nitrogen and helium-oxygen potentials of Keil *et al.*[26] yields mixed results. The well depths at $\gamma = 90°$ for helium with nitrogen, oxygen, and iodine are 31.3, 37.5, and 31.9 K respectively. The $\epsilon(90°)$ values of Kiel *et al.* would seem to be in better agreement with the well depth of Potential D_{He} (63.7 K). This can be seen by scaling $\epsilon(90°)$ for the potentials of Keil *et al.* by the ratio of the well depth of helium-argon (24.2 K)[27] to the well depth of helium-neon (14.3 K).[27] The value of the well depths scaled in this manner would be 52.9 K and 63.5 K for nitrogen and oxygen respectively. This qualitative agreement is not all that surprising since these potentials were determined using a procedure that was similar to that used to determine Potential D_{He}.

Conversely, in relation to the well depth reported by Blazy *et al.*, even our shallower well depth is too large. However, the ϵ (D_e) values for the iodine complexes are only estimates and there may be significant error in their assignment. For instance, the Morse range parameter that Blazy *et al.* used to determine D_e from their experimental value of D_0 yields a potential in which even at 2 Å intermolecular separation, $U(r)$ is only a factor of 3 greater than the well depth, D_e. This type of behavior is unparalleled in any interatomic or intermolecular potential ever determined. Recently, Schwenke and Truhlar[28] calculated the short and long range forces for the helium-iodine potential and combined them using a suitable damping function to obtain a more reasonable

intermolecular potential for $\gamma = 90°$. Their results confirmed that the range parameter used by Blazy *et al.* was much too small. Unfortunately, they chose their damping function such that it would reproduce the value of D_e of Blazy *et al.* It would have been more appropriate to try to match the experimental value of D_0. Thus, we know that the value of D_e for helium-iodine is not accurate, but the value of D_0 (27.3 K) is probably accurate and would suggest that the well depth of Potential B_{He} is closer to the correct value.

3.6 Conclusions

Anisotropic potential energy surfaces have been determined for helium-chlorine and neon-chlorine using total differential cross sections and the IOS approximation. The neon-chlorine potential is felt to be accurate within the region of $\gamma = 90° \pm 50°$. This angular range should be increased by the inclusion of the inelastic scattering energy loss spectra into the potential determination process. In the region of $\gamma = 90°$, this potential is found to agree fairly well with what little information is known about the potential surface from photodissociation experiments.

Two distinctly different helium-chlorine potentials have been determined which both reproduce the experimental data. There is some indication that Potential B_{He} is more appropriate even though the value of ϵ_0 for that potential is only about 60% of the well depth of the best isotropic potential for this system. However, the level of agreement between this experiment, intuition and results from similar systems is insufficient to justify any claims of accuracy for either

proposed helium-chlorine potential. Both of these systems, neon-chlorine and helium-chlorine, merit further investigation.

References

[1] K.C. Janda, Adv. Chem. Phys. **60**, 201–244, (1985).

[2] D.H. Levy, Adv. Chem. Phys. **47**, 323–362, (1981).

[3] J.A. Beswick and J. Jortner, Adv. Chem. Phys. **47**, 363–506, (1981).

[4] G.E. Ewing, J. Chem. Phys. **71**, 3143–3144, (1979).

[5] (a) D.E. Brinza, B.A. Swartz, C.M. Western and K.C. Janda, J. Chem. Phys. **79**, 1541–1542, (1983);
(b) D.E. Brinza, C.M. Western, D.D. Evard, F. Thommen, B.A. Swartz and K.C. Janda, J. Phys. Chem. **88**, 2004–2009, (1984).

[6] (a) R.T Pack, Chem. Phys. Lett. **55**, 197–201, (1978);
(b) R.J. Cross, Jr., J. Chem. Phys. **52**, 5703–5707, (1970).

[7] See, for example, G.A. Parker, M. Keil and A. Kuppermann, J. Chem. Phys. **78**, 1145–1162, (1983).

[8] P.E. Siska, J.M. Parson, T.P. Schafer and Y.T. Lee, J. Chem. Phys. **55**, 5762–5770, (1971).

[9] See, for example, R.T Pack, J. Chem. Phys. **64**, 1659–67, (1976).

[10] S. Stolte and J. Reuss, in, *Atom - Molecule Collision Theory: A Guide for the Experimentalist*, edited by R.B. Bernstein (Plenum Press, New York, 1979).

[11] T.M. Miller and B. Bederson, Adv. At. Mol. Phys. **13**, 1–55, (1977).

[12] J.O. Hirschfelder, C.F. Curtiss and R.B. Bird, *Molecular Theory of Gases and Liquids* (John Wiley and Sons, New York, 1954).

[13] J.W. Winneczek, *Ph.D. Thesis* (California Institute of Technology, 1985).

[14] R.C. Weast, editor, *Handbook of Chemistry and Physics,* 59^{th} edit. (CRC Press, West Palm Beach, Florida, 1978).

[15] K.P. Huber and G. Herzberg, *Molecular Spectra and Molecular Structure: IV. Constants of Diatomic Molecules* (Van Nostrand Reinhold, New York, 1979).

[16] See, for example, M. Abromowitz and I.A. Stegun, editors, *Handbook of Mathematical Functions* (Dover Publication, New York, 1965).

[17] T.J.P. O'Brien and R.B. Bernstien, J. Chem. Phys. **51**, 5112–5117, (1969).

[18] D.D. Evard, F. Thommen and K.C. Janda, manuscript in preparation.

[19] M.A. Hoffbauer, S. Burdenski, C.F. Giese and W.R. Gentry, J. Chem. Phys. **78**, 3832–3837, (1983).

[20] U. Buck, A. Kohlase, D. Secrest, T. Phillips, G. Scoles and F. Grein, Mol. Phys., in press.

[21] R.T Pack, E. Piper, G.A. Pfeffer and J.P. Toennies, J. Chem. Phys. **80**, 4940–4950, (1984).

[22] J.I. Cline, D.D. Evard, F. Thommen and K.C. Janda, manuscript in preparation.

[23] J.A. Blazy, B.M. Dekoven, T.D. Russell and D.H. Levy, J. Chem. Phys. **72**, 2439–2444, (1980).

[24] B.A. Swartz, D.E. Brinza, C.M. Western and K.C. Janda, J. Phys. Chem. **88**, 6272–6277, (1984).

[25] C.Y. Ng, Y.T. Lee and J.A. Barker, J. Chem. Phys. **61**, 1996–2002, (1974).

[26] M. Keil, J.T. Slankas and A. Kuppermann, J. Chem. Phys. **70**, 541–551, (1979).

[27] C.H. Chen, P.E. Siska and Y.T. Lee, J. Chem. Phys. **59**, 601–610, (1973).

[28] D.W. Schwenke and D.G. Truhlar, Chem. Phys. Lett. **98**, 217–220, (1983).

Appendix A

Second Virial Coefficients

A.1 Introduction

Before molecular beams were used to probe the forces of interaction between molecules, scientists had determined the relationships between certain macroscopic observables and the intermolecular potential. Potentials determined from macroscopic properties were not unique however, and great uncertainty persisted about the quantitative values of these potentials. As the use of differential cross sections measurements for potential determination matured, it was found to be desirable to include the macroscopic observables in the potential determination as they were often sensitive to different areas of the potential energy surface. Among the macroscopic observables used in this way are properties such as viscosity, thermal conductivity, diffusion, and the deviations of a gas from ideal behavior.[1,2] The deviations from ideal behavior, or imperfections, are the focus of this appendix.

Many equations of state have been proposed to account for gas imperfections, but none is more generally applicable or closely related to the intermolecular potential than the virial equation of state.

$$\frac{P\tilde{V}}{RT} = 1 + \frac{B(T)}{\tilde{V}} + \frac{C(T)}{\tilde{V}^2} + \cdots \tag{1}$$

This equation, generally attributed to Kammerlingh Onnes, is relatively easily derived from statistical mechanics via either the canonical partition function[3] or the grand canonical partition function.[4] The coefficients in the power series in density $(\frac{1}{\tilde{V}})$ in Equation (1), $B(T), C(T)$, etc., are known as the second, third, etc., virial coefficients. The terms, and thus the coefficients, in the power

series are related to the interactions between two ($B(T)$), three ($C(T)$), etc. molecules in the gas. Each of the virial coefficients can be explicitly related to the intermolecular potential, but only the second virial coefficient can be readily determined experimentally with the kind of accuracy necessary for estimation of an intermolecular potential.

Experimentally, virial coefficients can be determined by simultaneously measuring the temperature and density of a gas at several pressures. The compressibility factor ($\frac{P\tilde{V}}{RT}$) can then be fit to a polynomial in density ($\frac{1}{\tilde{V}}$) with the coefficients of the polynomial approximating the virial coefficients (evaluating a polynomial of infinite order would be necessary for equality between the coefficients). The second virial coefficient, $B(T)$, can normally be determined in this manner over a broad temperature range of approximately $k_BT/\epsilon = 0.5$ to $k_BT/\epsilon = 5.0$ where ϵ is the well depth of the interaction.

In the following section, the relationship of the second virial coefficient to the intermolecular potential will be examined, and the details of the calculation of second virial coefficients from a given potential discussed. In the final section, the FORTRAN subroutine for calculating second virial coefficients which was used in the determination of the argon-, and methane-methane potentials will be presented.

A.2 Calculation

A.2.1 The Classical Second Virial Coefficient

The classical form of the second virial coefficient can be shown[2] to be related

to the intermolecular potential by the following equation.

$$B_{cl}(T) = -2\pi N_A \int_0^\infty [e^{-U(r)/k_BT} - 1] r^2 \, dr \tag{2}$$

The part of the integrand in Equation (2) which is dependent on r only through the intermolecular potential, namely $e^{-U(r)/k_BT} - 1$, is commonly called the Mayer function. For clarity of the discussion which follows, the Mayer function (multiplied by $-2\pi N_A r_{min}^3$) is plotted as a function of the reduced internuclear distance ($\frac{r}{r_{min}}$) for several temperatures in Figure 1. It is evident from Figure 1 that the Mayer function is essentially constant at both small and large values of the internuclear distance. In both of these regions, Equation (2) can be evaluated analytically (as in the discussion that follows).

At small internuclear separations, $U(r) \gg k_BT$ and the exponential term in Equation (2) becomes many orders of magnitude less than unity. Neglecting the exponential, the integral can be performed analytically.

$$\int_0^{r_a} [e^{-U(r)/k_BT} - 1] r^2 \, dr \approx \int_0^{r_a} -r^2 \, dr = -\frac{1}{3} r_a^3 \tag{3}$$

In Equation (3), r_a is chosen such that $e^{-U(r_a)/k_BT} \ll 1$. In the calculations used for our methane studies, r_a was chosen as the point at which $U(r_a) = 20$ kcal/mol which in the worst case, the highest temperature datum (600 K), makes $e^{-U(r_a)/k_BT} \approx 5 \times 10^{-8}$.

At large internuclear distances, $U(r) \ll k_BT$ and the exponential can be expanded in a power series.

$$e^{-U(r)/k_BT} \approx 1 - \frac{U(r)}{k_BT} + \frac{1}{2}\left(\frac{U(r)}{k_BT}\right)^2 + \cdots \tag{4}$$

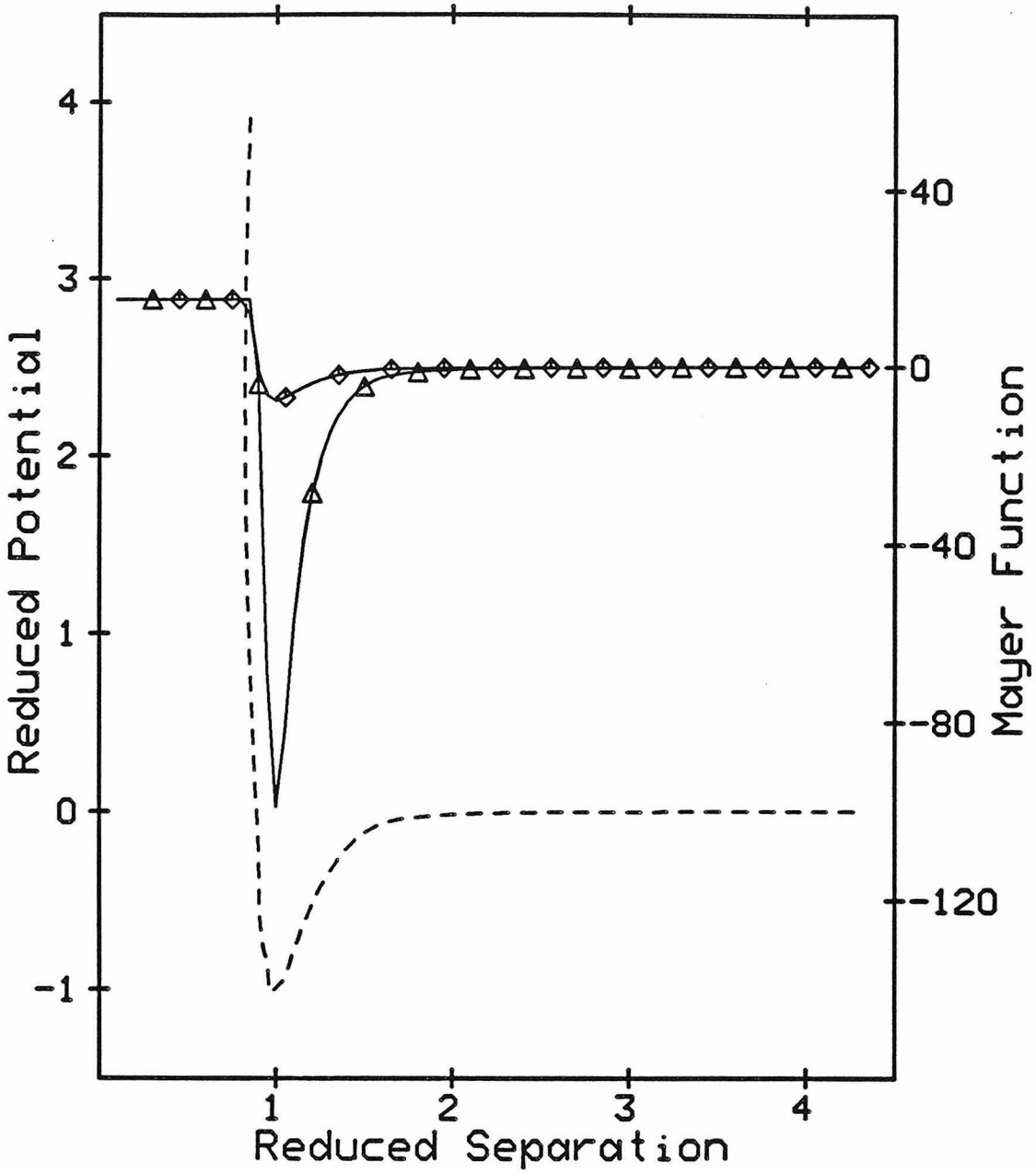

Figure 1. The Mayer function, $e^{-U(r)/kT} - 1$, is plotted as a function of reduced separation (r/r_{min}) for two temperatures: △ – 100 K, ◇ – 500 K. The reduced intermolecular potential (- - -) from which the functions were calculated is also shown to illustrate the sensitivity of the Mayer function to the potential.

Since in this region only the van der Waals dispersion terms ($C_n r^{-n}, n = 6, 8, \ldots$) contribute to the potential, the integral can once again be performed analytically.

$$\int_{r_b}^{\infty} \left[\left(1 - \frac{U(r)}{k_B T} \right) - 1 \right] r^2 \, dr = \frac{1}{k_B T} \left\{ \frac{C_6}{3} r_b^{-3} + \frac{C_8}{5} r_b^{-5} + \cdots \right\} \qquad (5)$$

In Equation (5), r_b is chosen such that Equation (4) is valid and can be approximated by its first two terms. This point was selected to be the maximum value of r at which $U(r) \geq -.002$ kcal/mol. At that value of $U(r)$, the lowest temperature datum (100 K) would have the third term of the expansion in Equation (4) less than .5% of the second term.

The remainder of the integral, from r_a to r_b was performed using Gaussian integration for an arbitrary interval:[5]

$$\int_a^b f(y) \, dy = \frac{b-a}{2} \sum_{i=1}^{n} w_i f(y_i) \, , \qquad (6)$$

where $y_i = (\frac{b-a}{2}) x_i + \frac{b+a}{2}$. Equation (6) transforms the integral, which cannot normally be performed analytically, into a sum in which the integrand is evaluated at standard quadrature points ($x_i \equiv$ the i^{th} zero of the Legendre polynomial of degree n, $P_n(x)$) and multiplied by a weighting factor ($w_i = 2/(1 - x_i^2)[P_n'(x_i)]^2$). The number of quadrature points used depends on the nature of the function and the degree of accuracy desired. For these calculations we have used 10 point quadrature for $r < r_{min}$ and 32 point quadrature for $r > r_{min}$. This amount of quadrature was found to be more than sufficient but was not decreased because the overall elastic scattering program spent a negligible amount of time in the virial subroutine.

A.2.2 The Quantum Correction

In order to fully quantify the second virial coefficient, the quantum mechanical nature of the interacting particles must be considered. This is normally accomplished using the semi-classical approach of Wigner[6] and Kirkwood[7] in which $B(T)$ is expanded in a power series in $\frac{h^2}{m}$.

$$B = B_{cl} + \left\{ \frac{h^2}{m} B_{q1} + \left(\frac{h^2}{m}\right)^2 B_{q2} + \cdots \right\} \mp \left(\frac{h^2}{m}\right)^{3/2} B_{perfect} \qquad (7)$$

The term $B_{perfect}$ is a statistical correction for either Bose-Einstien(−) or Fermi-Dirac(+) particles; however, this symmetry correction has been shown to lead to erroneous results[8] and should not be used. In fact, exact phase shift calculations have shown that even for very low molecular weight Bose-Einstien or Fermi-Dirac gases such as ^{3}He or ^{4}He the deviation in B from Boltzman statistics ($B_{perfect} = 0$) is insignificant above $\sim$ 7 K (it is the dominant term at 0 K as would be expected)[8] although the actual value of $B_{perfect}$ might not be insignificant.

The coefficients, B_{qi}, in the expansion in Equation (7) are each related to the potential and its derivatives. For the gases of interest here, all but the first quantum correction term are negligible at all temperatures for which second virial coefficient data were available. The first quantum correction represents $\sim$ 3% of the total second virial coefficient for methane at low temperature and must be included in the calculation. Figure 2 illustrates the difference between the classical values and the two term Wigner-Kirkwood values of the second virial coefficient of methane. Equation (8) shows the relationship between B_{q1} and the

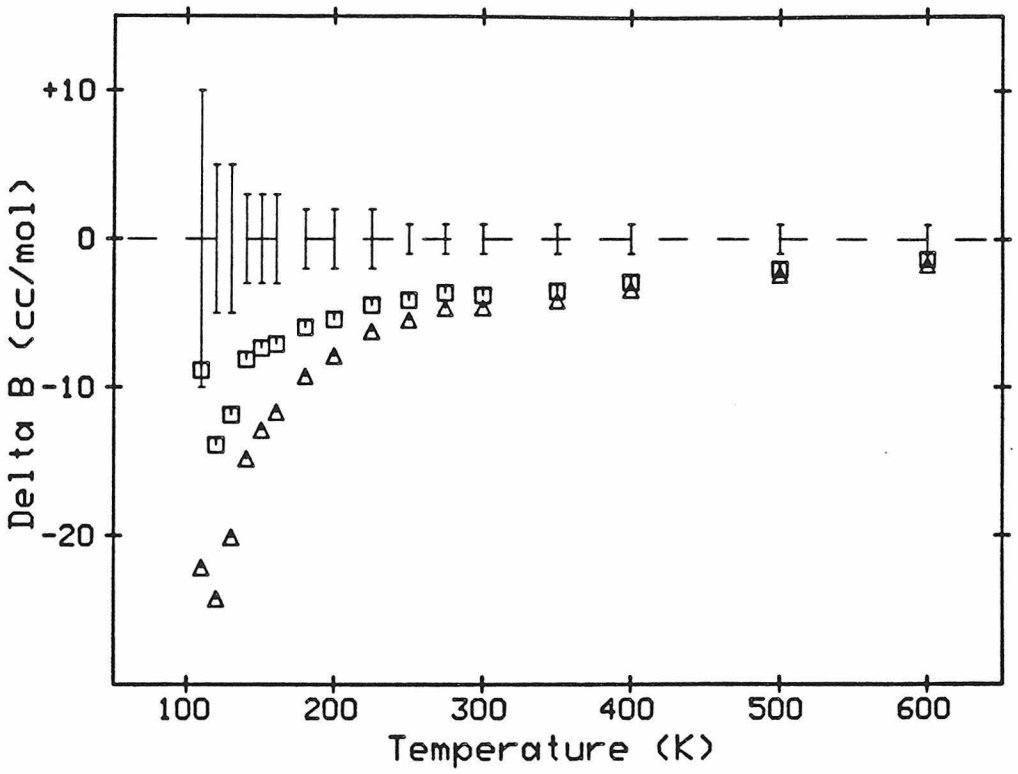

Figure 2. Delta $B = B_{expt} - B_{calc}$ is shown for both the classical second virial coefficient (△) and the semi-classical second virial coefficient (□). Each is calculated from the methane-methane "Potential A" of Reid *et al.*[9] The experimental values with error bars are from Dymond and Smith.[11]

intermolecular potential.

$$B_{q1}(T) = \frac{N_A}{24\pi(k_BT)^3}\int_0^\infty e^{-U(r)/k_BT}U'^2r^2\,dr \tag{8}$$

This correction can be evaluated in a manner similar to the classical second virial coefficient. In regions of small and large internuclear separations the integrand is many orders of magnitude less than its value in the region of the potential well and can therefore be neglected. This behavior is shown pictorially in Figures 3 a and b in which the logarithm of the integrand of B_{q1} (for the methane-methane potential[9] is plotted as a function of reduced separation ($\frac{r}{r_{min}}$). For the smallest value of reduced separation shown in Figure 3 a ($\frac{r}{r_{min}} = .83$) the integrand is already six orders of magnitude below its peak value and decreasing at a rate of approximately 120 orders of magnitude per reduced unit of separation. Similarly, at a reduced distance of 2.2, the integrand is once again six orders of magnitude smaller than its peak value and decreasing four orders of magnitude per reduced unit. Thus, we only need to evaluate the integral from about $\frac{r}{r_{min}} = .6$ to $\frac{r}{r_{min}} = 10$. The actual integral evaluation is done using Gaussian integration (Equation (6)). For simplicity, the same number of quadrature points were used as in the classical calculation.

A.2.3 Sensitivity to the Potential

The second virial coefficient data, while not nearly as sensitive to the intermolecular potential as our differential cross sections,[10] adds more constraints to our multiparameter potentials. In particular, the high temperature data (Figures 1 and 3 b) are almost exclusively influenced by the position and slope

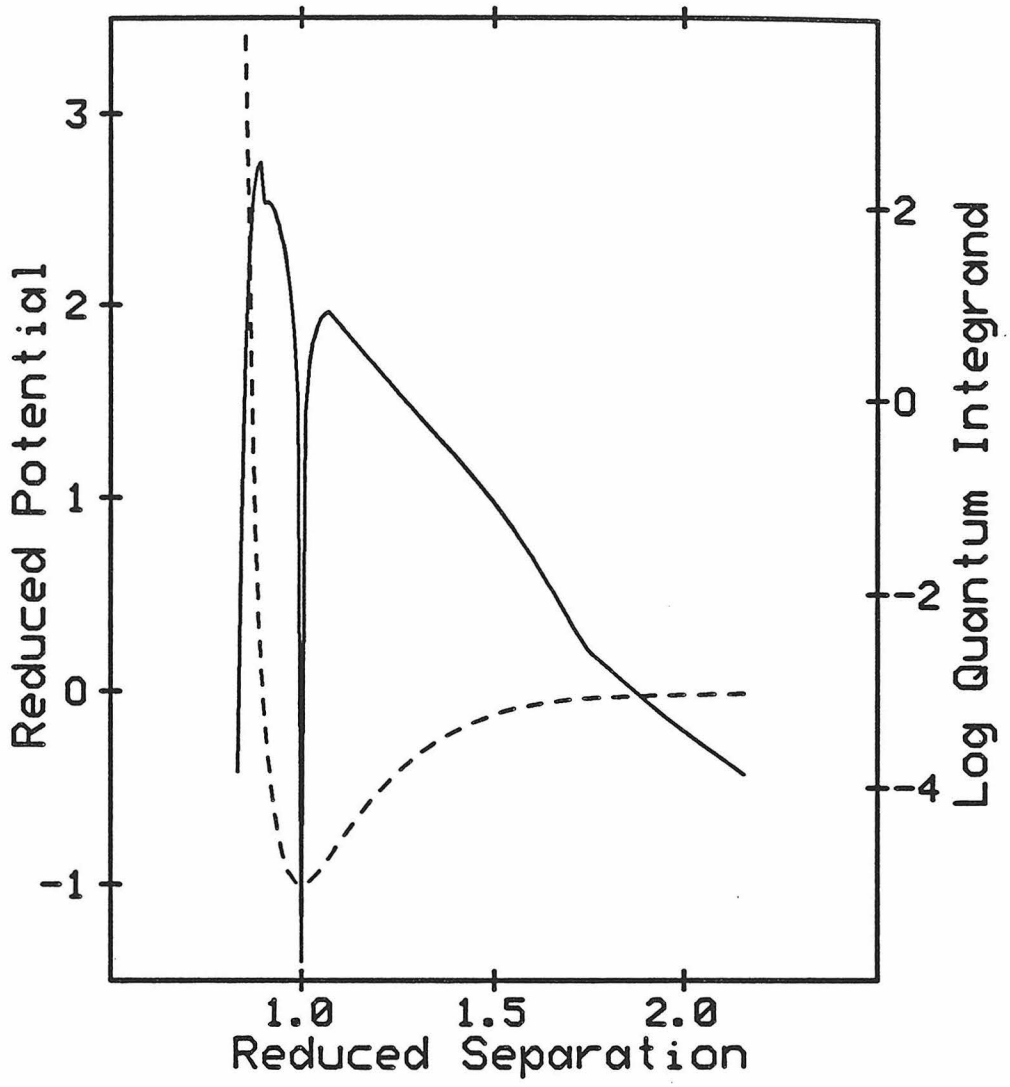

Figure 3a. The logarithm of the integrand of the first quantum correction to the classical second virial coefficient as a function of reduced intermolecular separation is displayed for a temperature of 100 K. The reduced potential used in the calculation of the integrand is also shown (- - -). Note: the kinks in the integrand are at those values of the reduced separation where the piecewise functions of the MMSV potential are joined together.

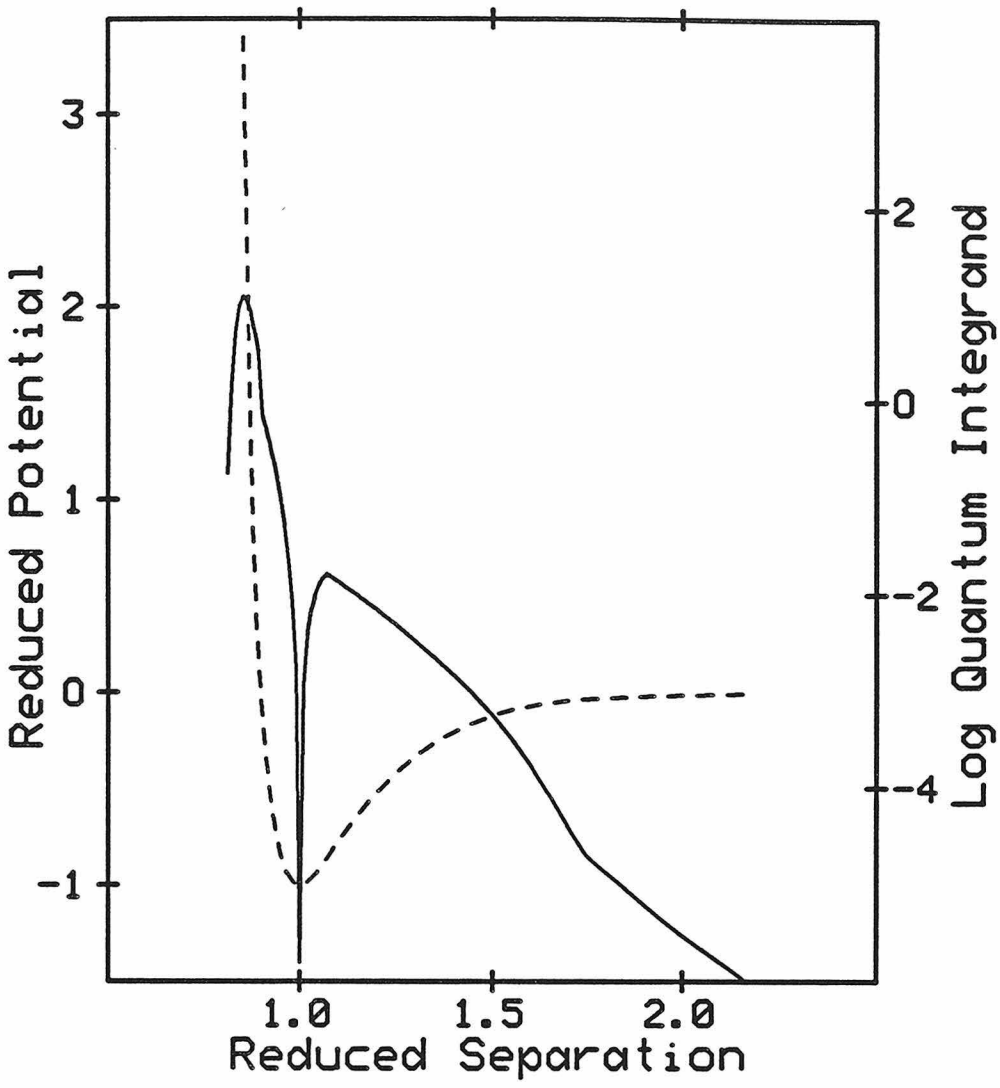

Figure 3b. The logarithm of the integrand of the first quantum correction to the classical second virial coefficient as a function of reduced intermolecular separation is displayed for a temperature of 500 K. The reduced potential used in the calculation of the integrand is also shown (- - -). Note: the kinks in the integrand are at those values of the reduced separation where the piecewise functions of the MMSV potential are joined together.

of the "hard wall" of the potential. In the MMSV potential used in Chapter 2, this data would then affect the value of the Morse wall shape parameter, β_1. The low energy differential cross sections by themselves are not overly sensitive to the value of that parameter and therefore, the second virial coefficient data is necessary to determine a reliable value of that parameter.

The low temperature data (Figures 1 and 3 a) are sensitive to the well width as a function of its depth,[2] and therefore mainly influence the Morse well shape parameter, β_2, since the depth of the well is fixed by the rainbow maxima of the differential cross sections.

A.2.4 Mixtures

Second virial coefficients for mixtures of gases are determined by finding the coefficients of the power series in density (Equation (1)) for a known composition mixture and for those of the pure gases. The interaction second virial coefficient, $B_{12}(T)$, is then determined using the following combination rule,

$$B_{mix} = \sum_{i=1}^{n} \sum_{j=1}^{n} \chi_i \chi_j B_{ij} \ , \tag{9}$$

in which χ_i is the mole fraction of component i. The interaction second virial coefficient for a binary mixture, can then be related to the intermolecular potential between component gases in the same manner as $B(T)$ for pure gases. The only difference in the equations presented earlier is that in Equation (7), 2μ, where μ is the reduced mass, should be substituted for m. There is significantly more uncertainty associated with determining B_{12} since it is affected by the cumulative uncertainties in B_{11} and B_{22} in addition to the uncertainty in B_{mix}.

The effects of this compounded uncertainty are evident in the displacement of the data sets of different investigators[11] in the argon-methane second virial coefficient data used in the potential determination of Chapter 2. These investigators each quoted error bars of 1-2 cc/mol while the agreement between authors was often worse than 20 cc/mol. For this reason, it was necessary to increase the uncertainties used to determine "best fits." The argon-methane interaction second virial coefficients are presented, by investigator, as the difference from the calculated values in Figure 4.

A.3 FORTRAN Subroutine

The following is a FORTRAN subroutine used to calculate second virial coefficients from an intermolecular potential provided by the user. The potential is generated within the program by calls to a subroutine, POT, which is a user supplied subroutine that calculates an analytical potential from parameters passed to the subroutine in array *A(I=1 to 15)*. The input data, such as the experimental values of the second virial coefficient and the associated errors are passed to the subroutine from the calling program through the common block, COMMON/VIR. The calculated second virial coefficients are then passed back to the calling program in that same common block. The units of the second virial coefficients on both input and output are the traditional units of cm^3/mol.

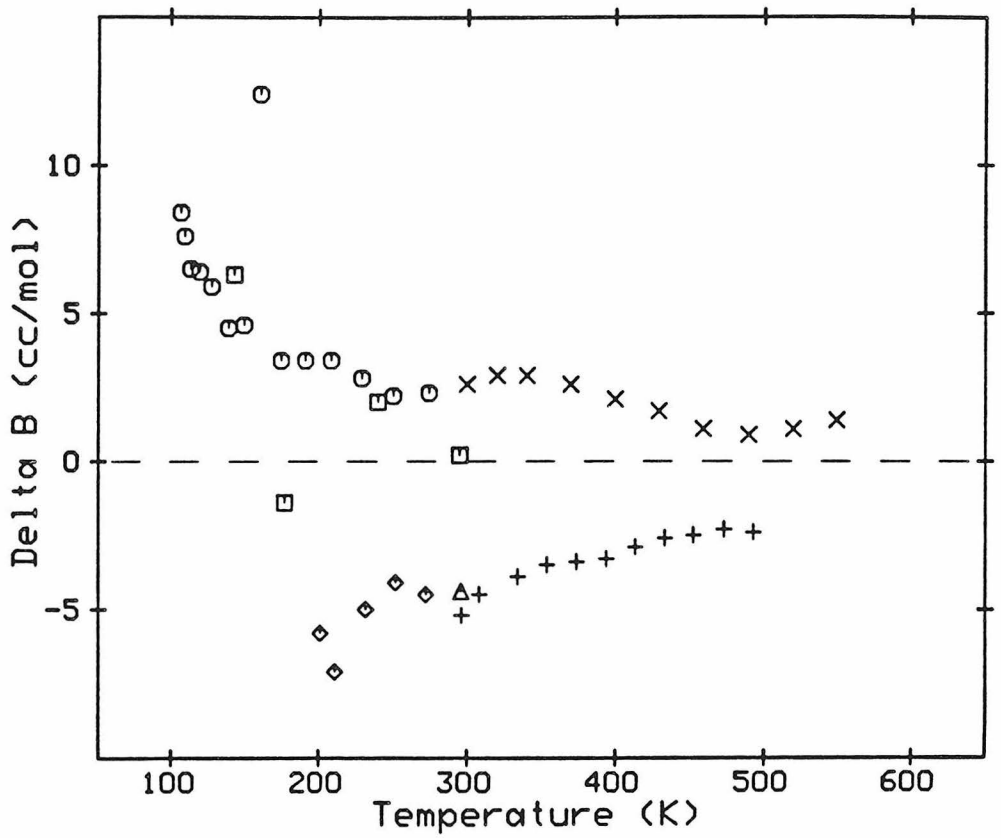

Figure 4. Delta $B = B_{calc} - B_{expt}$ is exhibited for the argon-methane second virial coefficient data used in the argon-methane potential determination of Chapter 2. Delta $B = 0$ would be perfect agreement with the potential from Chapter 2. The experimental data is presented by investigator: □ – Ref. 12, ◯ – Ref. 13, △ – Ref. 14, + – Ref. 15, × – Ref. 16, ◇ – Ref. 17.

```
      SUBROUTINE VIRIAL(A,BTCHI)
C.....
C     SUBROUTINE TO CALCULATE SECOND VIRIAL COEFFICIENTS
C     FROM POTENTIAL SUPPLIED.
C
C     CALCULATION IS SIMILAR TO THAT DISCUSSED IN PACK,et al.
C     JCP,77(11),p.5479.
C
C     QUADRATURE POINTS AND WEIGHTS ARE FROM Handbook of
C     Mathematical Functions ed. by Abromowitz and Stegun,
C     Dover Publications, New York, (1965) pp.887,888,916,917.
C
C     ***** INPUT DATA *****
C     NVIR= # of virial coefficient data points
C     NVFLG=  0 :no virial coefficient data(no calculation)
C             1 :virial coefficient data exists(calculation)
C     DEGK(I)= the temperatures, in degrees Kelvin, to which
C             data corresponds
C     BTDAT(I)= the expt. virial coef. in units of cubic
C             centimeters per mole
C     BTERR(I)= the error associated with BTDAT(I)
C     NC6= the index of the c6 term in array A
C     NC8= the index of the c8 term in array A
C     NC10= the index of the c10 term in array A
C     XI(I)= zeros of the Legendre polynomials(quad points)
C             for integral over r<rmin
C     WI(I)= weights for Gaussian integration at XI(I)
C     X2I(I)= zeros of the Legendre polynomials
C             for integral over r>rmin
C     W2I(I)= weights for Gaussian integration at X2I(I)
C     RM= reduced mass in amu
C     A(I)= potential parameters
C             A(1) is always the well depth in Kcal/mol
C             A(2) is always the position of the well minimum
C                 in Angstroms
C     **********************
C
C     **** OUTPUT DATA *****
C     BTCHI= the normalized chi square error
C     BT(I)= the calculated virial coefficients at the
C             temperature DEGK(I). In cubic cm/mol
C     **********************
```

```
C
C       **** SUBROUTINES *****
C       POT(X,A,V,VP,L,RM)—calculates potential at L values
C                  of the reduced internuclear separation, X(I),
C                  and returns the reduced potential and its
C                  reduced derivative in V(I) and VP(I).
C       **********************
C.....................................................................
        DIMENSION A(15),X(10),V(10),VP(10)
        DIMENSION XI(5),WI(10),YI(10),RI(10),RI2(10),VI(10)
        DIMENSION X2I(16),W2I(32),Y2I(32),R2I(32),R2I2(32),V2I(32),Y2(8)
        DIMENSION QYI(10),QRI(10),QRI2(10),QV(10),QVI(10),QVPI(10)
        DIMENSION QY2I(32),QY2(8),QR2I(32),QR2I2(32)
        DIMENSION QV2I(32),QVP2I(32)
        DATA (XI(I),I=1,5)/.148874,.433395,.679410,.865063,.973907/
        DATA (WI(I),I=1,5)/.295524,.269267,.219086,.149451,.066671/
        DATA (X2I(I),I=1,16)/.04831,.14447,.23929,.33187,.42135,
       & .50690,.58772,.66304,.73218,.79448,.84937,.89632,.93491,
       & .96476,.98561,.99726/
        DATA (W2I(I),I=1,16)/.09654,.09564,.09384,.09117,.08765,
       & .08331,.07819,.07235,.06582,.05868,.05100,.04284,.03427,
       & .02539,.01627,.00701/
        DATA BOLTZ,PI,AVAG/1.98717E-03,3.14159,6.02205E+23/
        DATA CONST,TOPIN/1.9367E+14,3.784E+24/
        COMMON/VIR/NVFLG,NVIR,DEGK(100),BTDAT(100),
       & BTERR(100),BT(100),NC6,NC8,NC10,RM
C.....................................................................
        IF(NVFLG.EQ.0) GOTO 200
        RMIN=A(2)*1.E-08
C       ******* CLASSICAL CALCULATION *******
C       DIVIDE POTENTIAL INTO 3 SEGMENTS. CALCULATION CAN
C         BE PERFORMED ANALYTICALLY AT SMALL(LESS THAN X1)
C         AND LARGE(GREATER THAN X2) VALUES OF REDUCED R.
C         X1 AND X2 ARE CHOOSEN SUCH THAT THE POTENTIAL AT
C         X1 >20 KCAL/MOL AND AT
C         X2 >-.002 KCAL/MOL(V1 & V2).
C
C       ******* QUANTUM CORRECTION *******
C       DIVIDE POTENTIAL INTO 4 SEGMENTS. INTEGRAL CAN BE
C         IGNORED AT X<.6 AND AT X>10. REMAINING VALUES
C         OF X ARE INTEGRATED FOR R<RMIN (TEN POINT
C         QUADRATURE) AND R>RMIN (THIRTY TWO POINT
```

```
C       QUADRATURE). INITIALLY, THE NAT. LOG OF THE
C       VARIOUS COMPONENTS OF THE INTEGRAL ARE
C       CALCULATED TO AVOID OVER(UNDER) FLOWS.
C
      V1=20./A(1)
      V2=-.002/A(1)
C
C     INITIAL QUESS AT X1 AND X2
C
      X1=.6
      X2=2.5
      L=2
      DO 10 M=1,50
      X(1)=X1
      X(2)=X2
      CALL POT(X,A,V,VP,L,RM)
      X1=X(1)+(V1-V(1))/VP(1)
      X2=X(2)+(V2-V(2))/VP(2)
      IF(ABS(X1-X(1)).GT.1.E-02*X1) GOTO 10
      IF(ABS(X2-X(2)).LE.1.E-02*X2) GOTO 20
 10   CONTINUE
C
C     CALCULATE QUAD POINTS (& POTENTIAL AT THOSE PTS.)
C       FOR R<RMIN - TEN POINT QUADRATURE
C       Q*** APPLIES TO QUANTUM CORRECTION
C
 20   DELX=(1.-X1)/2.
      SUMX=(1.+X1)/2.
      DO 30 I=1,5
      YI(I)=DELX*XI(I)+SUMX
      QYI(I)=.2*XI(I)+.8
      J=I+5
      YI(J)=SUMX-DELX*XI(I)
      QYI(J)=.8-.2*XI(I)
      WI(J)=WI(I)
 30   CONTINUE
      L=10
      CALL POT(YI,A,V,VP,L,RM)
      CALL POT(QYI,A,QV,VP,L,RM)
      DO 40 I=1,10
      RI(I)=YI(I)*RMIN
      RI2(I)=RI(I)*RI(I)
```

```
      VI(I)=V(I)*A(1)/BOLTZ
      QRI(I)=QYI(I)*RMIN
      QRI2(I)=2.*ALOG(QRI(I))
      QVI(I)=QV(I)*A(1)/BOLTZ
      QVPI(I)=2.*ALOG(ABS(VP(I)*A(1)/RMIN))
 40   CONTINUE
C
C     CALCULATE QUAD POINTS (& POTENTIAL AT THOSE POINTS)
C      FOR R>RMIN - 32 POINT QUADRATURE
C      Q*** APPLIES TO QUANTUM CORRECTION
C
      DELX2=(X2-1.)/2.
      SUMX2=(X2+1.)/2.
      DO 50 I=1,16
      Y2I(I)=DELX2*X2I(I)+SUMX2
      QY2I(I)=4.5*X2I(I)+5.5
      J=I+16
      Y2I(J)=SUMX2-DELX2*X2I(I)
      QY2I(J)=5.5-4.5*X2I(I)
      W2I(J)=W2I(I)
 50   CONTINUE
      L=8
      DO 80 I=0,3
      DO 60 J=1,8
      Y2(J)=Y2I(J+I*8)
      QY2(J)=QY2I(J+I*8)
 60   CONTINUE
      CALL POT(Y2,A,V,VP,L,RM)
      CALL POT(QY2,A,QV,VP,L,RM)
      DO 70 J=1,8
      K=J+I*8
      R2I(K)=Y2I(K)*RMIN
      R2I2(K)=R2I(K)*R2I(K)
      V2I(K)=V(J)*A(1)/BOLTZ
      QR2I(K)=QY2I(K)*RMIN
      QR2I2(K)=2.*ALOG(QR2I(K))
      QV2I(K)=QV(J)*A(1)/BOLTZ
      QVP2I(K)=2.*ALOG(ABS(VP(J)*A(1)/RMIN))
 70   CONTINUE
 80   CONTINUE
C
C     INTEGRAL OVER REGION 1 - R LESS THAN X1
```

```
C
      R1=X1*RMIN
      BT1=2.*PI*AVAG*R1**3/3.
C
C     PART OF REGION 3 INTEGRAL INDEPENDENT OF TEMP.
C
      R2=X2*A(2)
      C6=A(NC6)
      C8=A(NC8)
      C10=A(NC10)
      PROD=C6/(3.*R2**3)+C8/(5.*R2**5)+C10/(7.*R2**7)
      BT3T=-TOPIN*PROD*1.E-24/BOLTZ
C
C     TEMPERATURE DEPENDENT INTEGRALS
C
      BTCHI=0.
      DO 110 I=1,NVIR
      BT3=BT3T/DEGK(I)
      BT2=0.
      BT22=0.
      QBT1=0.
      QBT2=0.
      DO 90 J=1,10
      BT2=BT2+WI(J)*(EXP(-VI(J)/DEGK(I))-1.)*RI2(J)
      QBT1=QBT1+WI(J)*EXP(QVPI(J)+QRI2(J)-QVI(J)/DEGK(I))
90    CONTINUE
      DO 100 J=1,32
      BT22=BT22+W2I(J)*(EXP(-V2I(J)/DEGK(I))-1.)*R2I2(J)
      QBT2=QBT2+W2I(J)*EXP(QVP2I(J)+QR2I2(J)-QV2I(J)/DEGK(I))
100   CONTINUE
      BT2=(BT2*DELX+BT22*DELX2)*RMIN*(-TOPIN)
      QBT=(CONST/DEGK(I)**3/RM)*RMIN*(.2*QBT1+4.5*QBT2)
      CBT=BT1+BT2+BT3
      BT(I)=QBT+CBT
      BTCHI=BTCHI+((BT(I)-BTDAT(I))/BTERR(I))**2
110   CONTINUE
      BTCHI=BTCHI/NVIR
200   CONTINUE
      RETURN
      END
```

References

[1] J.O. Hirschfelder, C.F. Curtis, and R.B. Bird, *Molecular Theory of Gases and Liquids* (John Wiley and Sons, New York, 1954).

[2] G.C. Maitland, M.Rigby, E.B. Smith and W.A. Wakeham, *Intermolecular Forces: Their Origin and Determination* (Oxford University Press, Oxford, England, 1981).

[3] J.E. Mayer and M.G. Mayer, *Statistical Mechanics* (J. Wiley, New York, New York, 1977).

[4] T.L. Hill, *Introduction to Statistical Thermodynamics* (Addison-Wesley, Reading, Massachusetts, 1960).

[5] See for example, M. Abromowitz and I.A. Stegun, editors, *Handbook of Mathematical Functions* (Dover Publications, New York, New York, 1965).

[6] E. Wigner, Phys. Rev. **40**, 749–759, (1932).

[7] (a) J.G. Kirkwood, Phys. Rev. **44**, 31–37, (1933);
(b) J.G. Kirkwood, Phys. Rev. **45**, 116–117, (1934).

[8] M.E. Boyd, S.Y. Larsen and J.E. Kilpatrick, J. Chem. Phys. **50**, 4034–4055, (1969).

[9] B.P. Reid, M.J. O'Loughlin and R.K. Sparks, J. Chem. Phys., in press.

[10] For example, as can be seen in Table 12 of Chapter 2, the dimensionless deviation of the second virial coefficient data is nearly insensitive to changes in the potential which produce large changes in the dimensionless deviations of the scattering data.

[11] J.H. Dymond and E.B. Smith, *The Virial Coefficients of Pure Gases and Mixtures* (Oxford University Press, Oxford, England, 1980).

[12] G. Thomaes, R. Van Steenwinkel and W. Stone, Mol. Phys. **5**, 301-306, (1962).

[13] M.A. Byrne, M.R. Jones and L.A.K. Staveley, Trans. Faraday Soc. **64**, 1747-1756, (1968).

[14] R.N. Lichtenthaler and K. Schäfer, Ber. Bunsenges. Phys. Chem. **73**, 42-48, (1969).

[15] K. Strein, R.N. Lichtenthaler, B. Schramm and K. Schäfer, Ber. Bunsenges. Phys. Chem. **75**, 1308-1313, (1971).

[16] J. Bellm, W. Reineke, K. Schäfer and B. Schramm, Ber. Bunsenges. Phys. Chem. **78**, 282-286, (1974).

[17] R. Hahn, K. Schäfer and B. Schramm, Ber. Bunsenges. Phys. Chem. **78**, 287-289, (1974).

Appendix B

Neon-Methane and Argon-Methane
Experimental Data

Neon-Methane and Argon-Methane Data

It has become customary to publish the raw data obtained from scattering experiments. This data can then be used with more sophisticated analysis or new information to obtain more realistic potentials. It is conceivable that the data from this experiment could be used by someone adept at close-coupling calculations to produce an improved anisotropic potential for argon-methane or a more realistic anisotropic potential for neon-methane.

The neon-methane data is found in Tables 1–3 for the 375, 637, and 1010 K collision energies respectively. The argon-methane data is reproduced in Tables 4–6 for the 400, 678, and 1081 K collision energies respectively. In each table, Θ is the laboratory scattering angle and Δ is the estimated uncertainty in the datum measured at angle Θ. For these systems, $\frac{1}{2}\Delta$ was estimated as in Equation (26) of Chapter 1, except for angles less than 5° where the method in Reference 42 of Chapter 1 was used.

Table 1: *Neon-methane (375 K)*

Θ	Signal	Δ	Θ	Signal	Δ
2.50	1611.47	85.99	13.50	42.32	1.00
2.75	1629.21	78.51	13.75	39.63	1.02
3.00	1464.31	63.27	14.00	37.96	0.96
3.25	1307.32	50.30	14.25	33.89	0.98
3.50	1021.16	34.81	14.50	32.21	0.94
3.75	854.32	25.44	15.00	28.23	0.92
4.00	689.40	17.61	15.50	26.75	0.88
4.25	649.74	13.55	16.00	25.93	0.88
4.50	628.84	9.89	16.50	23.06	0.88
4.75	659.74	6.94	17.00	21.50	0.88
5.00	627.00	3.52	17.50	19.40	0.88
5.25	586.35	3.58	18.00	18.33	0.88
5.50	488.64	3.46	18.50	17.60	0.86
5.75	421.18	3.48	19.00	16.63	0.86
6.00	341.14	3.34	19.50	16.04	0.86
6.25	315.06	3.36	20.00	15.34	0.86
6.50	295.92	3.22	21.00	13.92	0.84
6.75	311.52	3.24	22.00	13.50	0.84
7.00	304.02	2.56	23.00	12.61	0.84
7.25	287.81	2.54	24.00	11.97	0.82
7.50	255.82	2.12	25.00	11.58	0.82
7.75	216.17	2.44	26.00	10.91	0.82
8.00	179.94	2.04	27.00	10.66	0.82
8.25	158.54	2.32	28.00	10.49	0.80
8.50	147.55	1.94	29.00	9.97	0.80
8.75	148.69	2.22	30.00	9.09	1.98
9.00	146.52	1.86	31.00	8.65	0.84
9.25	144.67	2.10	32.00	8.67	0.64
9.50	131.37	1.76	33.00	9.11	0.56
9.75	113.09	1.96	34.00	8.18	0.52
10.00	100.00	2.00	35.00	8.32	0.50
10.25	86.49	1.82	36.00	7.89	0.48
10.50	76.88	1.54	37.00	7.48	0.48
10.75	74.87	1.68	38.00	7.23	0.48

- continued -

Table 1: continued

Θ	Signal	Δ	Θ	Signal	Δ
11.00	74.61	1.44	39.00	6.96	0.48
11.25	74.74	1.54	40.00	7.03	0.42
11.50	72.15	1.32	41.00	6.89	0.42
11.75	67.22	1.40	42.00	6.83	0.42
12.00	59.75	1.20	43.00	6.92	0.42
12.25	53.40	1.26	45.00	6.29	0.42
12.50	47.37	1.10	47.00	6.06	0.42
12.75	45.24	1.14	49.00	5.75	0.44
13.00	42.42	1.04	51.00	6.15	0.44
13.25	42.01	1.08			

Table 2: *Neon-methane (637 K)*

Θ	Signal	Δ	Θ	Signal	Δ
3.00	2248.69	92.53	12.25	42.98	1.32
3.25	1885.23	68.40	12.50	42.40	1.26
3.50	1762.99	55.20	12.75	40.22	1.20
3.75	1636.74	43.13	13.00	39.61	1.12
4.00	1437.32	30.89	13.25	36.87	1.10
4.25	1127.26	18.97	13.50	36.40	1.06
4.50	875.36	10.75	13.75	35.44	1.04
4.75	709.05	5.51	14.00	34.18	1.00
5.00	639.53	3.82	14.25	32.76	0.98
5.25	618.04	3.82	14.50	32.39	0.96
5.50	576.08	3.80	14.75	31.53	0.96
5.75	491.43	3.76	15.00	30.42	0.94
6.00	391.88	3.72	15.50	28.51	0.92
6.25	304.82	3.64	16.00	27.20	0.92
6.50	260.22	3.60	16.50	24.96	0.90
6.75	244.06	3.54	17.00	24.91	0.90
7.00	239.39	3.50	17.50	25.03	0.92
7.25	223.73	3.38	18.00	23.34	0.92
7.50	191.25	3.32	18.50	23.64	0.92
7.75	153.01	3.28	19.00	23.16	0.90
8.00	129.82	3.20	19.50	21.94	0.90
8.25	112.64	3.12	20.00	20.67	0.90
8.50	106.38	3.04	21.00	19.75	0.76
8.75	107.70	2.94	22.00	18.73	0.76
9.00	100.17	0.60	23.00	18.16	0.74
9.25	89.81	2.30	24.00	17.06	0.74
9.50	73.79	2.20	25.00	16.44	0.72
9.75	66.18	2.12	26.00	15.97	0.74
10.00	63.57	2.06	28.00	14.65	0.72
10.25	60.19	1.98	30.00	14.23	0.72
10.50	59.50	1.90	32.00	13.53	0.72
10.75	58.21	1.80	34.00	12.92	0.72
11.00	53.13	1.72	36.00	12.39	0.72
11.25	50.72	1.62	38.00	11.24	0.72
11.50	46.44	1.54	40.00	10.80	0.72
11.75	43.72	1.48	42.00	10.42	0.72
12.00	44.16	1.44	44.00	10.72	0.72

Table 3: *Neon-methane (1010 K)*

Θ	Signal	Δ	Θ	Signal	Δ
2.50	608.70	43.57	17.00	5.44	0.38
3.00	440.90	29.20	18.00	4.82	0.37
3.50	272.90	18.74	19.00	4.75	0.37
4.00	165.90	13.18	20.00	4.58	0.37
4.50	132.90	10.78	21.00	4.15	0.26
5.00	84.24	0.80	22.00	4.08	0.26
5.50	56.82	0.80	23.00	3.80	0.25
6.00	46.14	0.89	24.00	3.76	0.25
6.50	31.57	0.74	25.00	3.62	0.25
7.00	24.29	0.71	26.00	3.22	0.25
7.50	21.33	0.79	28.00	3.08	0.24
8.00	16.39	0.76	30.00	3.13	0.24
8.50	13.57	0.74	32.00	2.88	0.24
9.00	12.39	0.71	34.00	2.65	0.24
9.50	10.94	0.68	36.00	2.69	0.25
10.00	10.00	0.60	38.00	2.44	0.25
11.00	8.88	0.51	40.00	2.43	0.25
12.00	8.18	0.45	42.00	2.36	0.25
13.00	7.14	0.41	44.00	2.42	0.26
14.00	7.06	0.39	46.00	2.12	0.26
15.00	6.51	0.38	48.00	2.33	0.26
16.00	6.03	0.38	50.00	2.33	0.26

Table 4: *Argon-methane (400 K)*

Θ	Signal	Δ	Θ	Signal	Δ
3.50	769.67	29.71	16.00	42.38	1.42
3.75	668.15	23.28	16.50	43.20	1.42
4.00	602.57	18.29	17.00	40.38	1.40
4.25	527.69	14.10	17.50	42.05	1.40
4.50	487.39	10.65	18.00	42.76	1.38
4.75	454.24	8.19	18.50	41.93	1.38
5.00	436.68	5.74	19.00	41.42	1.38
5.25	409.31	5.86	19.50	39.84	1.36
5.50	384.06	5.56	20.00	40.14	1.38
5.75	342.13	5.78	21.00	38.83	1.18
6.00	325.76	5.54	22.00	36.57	1.18
6.25	293.61	5.62	23.00	35.20	1.16
6.50	279.44	5.22	24.00	33.26	1.14
6.75	268.06	5.44	25.00	29.55	1.14
7.00	252.22	5.16	26.00	26.89	1.14
7.25	241.45	5.30	27.00	25.16	1.12
7.50	214.67	4.86	28.00	22.22	1.10
7.75	201.05	5.14	29.00	20.61	1.10
8.00	186.84	4.80	30.00	18.35	1.10
8.25	172.70	4.04	31.00	16.63	0.86
8.50	160.58	4.46	32.00	14.75	0.90
8.75	152.20	3.86	33.00	12.58	0.86
9.00	142.75	4.04	34.00	12.15	0.90
9.25	132.93	3.66	35.00	10.31	0.86
9.50	117.58	3.70	36.00	10.85	0.90
9.75	111.02	3.46	37.00	9.22	0.86
10.00	100.00	3.36	38.00	9.97	0.88
10.25	94.10	3.26	39.00	8.52	0.86
10.50	86.49	2.62	40.00	8.48	0.88
10.75	82.12	3.02	41.00	7.15	0.90

- continued -

Table 4: continued

Θ	Signal	Δ	Θ	Signal	Δ
11.00	74.35	2.42	42.00	7.10	0.88
11.50	65.27	2.20	43.00	6.90	0.90
12.00	59.10	2.00	44.00	6.82	0.88
12.50	55.47	1.82	45.00	7.01	0.92
13.00	49.27	1.70	46.00	6.15	0.88
13.50	49.71	1.60	47.00	6.62	0.90
14.00	45.38	1.54	48.00	5.72	0.88
14.50	45.22	1.50	49.00	4.89	0.92
15.00	42.12	1.48	50.00	6.02	0.88
15.50	42.24	1.44			

Table 5: *Argon-methane (678 K)*

Θ	Signal	Δ	Θ	Signal	Δ
2.50	1929.63	103.5	14.50	72.03	1.53
3.00	1240.31	55.62	14.75	69.14	1.21
3.50	902.89	32.55	15.00	65.08	1.49
4.00	667.58	18.49	15.25	64.80	1.18
4.50	441.17	9.28	15.50	60.69	1.45
5.00	321.83	4.76	15.75	58.48	1.16
5.50	240.28	4.72	16.00	56.98	1.44
6.00	175.00	4.62	16.25	54.03	1.16
6.50	138.15	4.45	16.50	51.57	1.44
7.00	119.00	4.29	16.75	48.78	1.16
7.50	107.41	3.38	17.00	46.52	1.30
7.75	104.03	3.30	17.25	44.79	1.08
8.00	100.81	3.26	17.50	41.96	1.29
8.25	99.62	3.16	17.75	41.03	1.08
8.50	95.93	3.10	18.00	38.23	1.31
8.75	98.56	3.00	18.25	36.72	1.08
9.00	97.43	2.91	18.50	35.41	1.31
9.25	97.54	2.81	18.75	33.26	1.08
9.50	99.58	2.75	19.00	31.43	1.32
9.75	99.42	2.66	19.25	29.89	1.09
10.00	100.00	0.84	19.50	27.33	1.33
10.25	100.79	2.49	19.75	27.80	1.09
10.50	101.52	2.98	20.00	25.75	1.09
10.75	104.04	2.28	21.00	22.09	1.34
11.00	100.85	2.69	22.00	16.73	1.82
11.25	101.22	2.07	23.00	16.00	1.80
11.50	98.21	2.42	24.00	13.21	1.78
11.75	96.28	1.86	25.00	11.24	1.76
12.00	96.30	2.19	26.00	10.21	1.22
12.25	92.09	1.67	28.00	8.42	0.70
12.50	91.14	1.97	30.00	7.37	0.70
12.75	89.94	1.51	32.00	6.68	0.70
13.00	86.23	1.78	34.00	6.46	0.71
13.25	85.01	1.38	36.00	5.98	0.73
13.50	82.43	1.66	38.00	6.10	0.72
13.75	80.43	1.29	40.00	5.73	0.74
14.00	77.79	1.57	42.00	5.67	0.71
14.25	74.49	1.25	44.00	4.60	0.70

Table 6: *Argon-methane (1081 K)*

Θ	Signal	Δ	Θ	Signal	Δ
2.50	1134.09	63.63	18.00	12.19	0.78
3.00	637.10	31.48	19.00	10.37	0.78
3.50	416.38	17.99	20.00	9.01	0.52
4.00	318.43	11.57	21.00	7.80	0.54
4.50	267.84	7.64	22.00	7.21	0.54
5.00	239.16	4.16	23.00	7.02	0.54
5.50	223.89	3.94	24.00	6.75	0.54
6.00	210.81	3.84	25.00	5.65	0.50
6.50	201.62	3.66	26.00	5.64	0.52
7.00	184.65	3.54	27.00	5.10	0.50
7.50	175.18	2.76	28.00	4.80	0.50
8.00	161.04	2.48	29.00	5.03	0.50
8.50	142.47	2.36	30.00	4.90	0.46
9.00	126.85	2.26	32.00	4.17	0.48
9.50	113.90	2.16	34.00	4.60	0.50
10.00	100.02	1.80	36.00	3.65	0.48
11.00	74.22	1.50	38.00	3.78	0.48
12.00	57.26	1.32	40.00	3.77	0.48
13.00	44.13	1.16	42.00	3.95	0.48
14.00	31.41	1.10	44.00	3.60	0.48
15.00	23.84	0.92	46.00	3.31	0.48
16.00	18.09	0.80	48.00	3.03	0.48
17.00	14.41	0.78	50.00	3.12	0.48

Appendix C

Helium-Chlorine and Neon-Chlorine
Experimental Data

Helium-Chlorine and Neon-Chlorine Data

It has become customary to publish the raw data obtained from scattering experiments. This is especially important in this case since this data is part of an ongoing study by another investigator. In addition, in light of my lack of satisfaction with the helium-chlorine potential, more extensive investigations are in order.

The helium-chlorine data is found in Tables 1 and 2 for the 340, and 511 collision energies respectively. The neon-chlorine data is reported in Tables 3 and 4 for the 464, and 612 collision energies respectively. In each table, Θ is the laboratory scattering angle and Δ is the estimated uncertainty in the datum measured at angle Θ. For these systems, Δ is the 90% confidence limit for replicate measurements as in Reference 41 of Chapter 1.

Table 1: *Helium-chlorine* (340 K)

Θ	Signal	Δ	Θ	Signal	Δ
5.00	1287.70	179.34	16.50	98.19	10.52
5.50	1085.22	43.97	17.00	94.89	6.75
6.00	1153.16	115.54	17.50	90.03	7.31
6.50	1028.51	38.39	18.00	80.12	10.64
7.00	943.60	88.04	18.50	72.01	7.34
7.50	694.93	26.82	19.00	58.10	6.20
8.00	523.13	42.05	19.50	62.17	6.48
8.50	362.91	13.33	20.00	56.43	6.04
9.00	285.17	25.94	21.00	58.06	6.30
9.50	231.04	13.19	22.00	48.59	6.67
10.00	267.25	12.23	23.00	45.94	7.95
10.50	274.50	11.05	24.00	47.14	6.45
11.00	298.65	12.72	25.00	45.28	10.30
11.50	274.86	8.32	26.00	42.69	8.89
12.00	260.37	10.78	27.00	41.44	7.69
12.50	209.77	10.53	28.00	39.26	8.78
13.00	170.40	7.54	29.00	35.53	7.99
13.50	131.31	11.35	30.00	36.36	6.17
14.00	116.56	7.57	31.00	33.80	7.45
14.50	94.27	6.23	32.00	32.04	6.21
15.00	100.00	7.00	33.00	31.01	6.48
15.50	98.85	7.27	34.00	37.15	6.28
16.00	100.77	8.42	35.00	32.45	6.31

Table 2: *Helium-chlorine* (511 K)

Θ	Signal	Δ	Θ	Signal	Δ
5.00	537.56	24.10	16.50	26.20	2.38
5.50	447.72	15.96	17.00	24.89	2.37
6.00	335.57	6.44	17.50	24.40	2.33
6.50	232.73	10.01	18.00	23.20	2.33
7.00	150.82	6.80	18.50	20.52	2.33
7.50	115.94	4.64	19.00	19.67	2.32
8.00	102.80	4.88	19.50	18.03	2.49
8.50	112.86	4.43	20.00	19.80	2.29
9.00	114.96	4.99	21.00	16.49	2.67
9.50	114.13	4.24	22.00	17.00	2.55
10.00	100.00	4.00	23.00	16.46	2.55
10.50	75.61	4.00	24.00	13.15	2.60
11.00	58.56	3.63	25.00	14.97	3.33
11.50	45.92	2.72	26.00	14.82	3.41
12.00	39.43	2.70	27.00	14.75	2.54
12.50	38.31	2.68	28.00	13.63	2.46
13.00	42.87	3.12	29.00	12.90	2.45
13.50	42.54	3.05	30.00	12.51	2.46
14.00	38.80	3.34	31.00	12.10	2.39
14.50	37.48	2.55	32.00	10.34	2.57
15.00	31.26	2.57	33.00	14.00	2.39
15.50	28.55	2.40	34.00	14.08	2.82
16.00	27.64	2.38	35.00	11.22	2.39

Table 3: *Neon-chlorine* (464 K)

Θ	Signal	Δ	Θ	Signal	Δ
4.00	371.58	9.42	16.50	31.24	0.94
4.50	294.27	3.58	17.00	28.32	0.68
5.00	240.78	3.74	17.50	25.39	0.84
5.50	202.92	2.34	18.00	23.70	0.76
6.00	186.00	2.27	18.50	21.69	0.68
6.50	169.37	4.23	19.00	19.48	0.79
7.00	155.16	2.02	19.50	17.82	0.56
7.50	144.71	1.79	20.00	16.96	0.80
8.00	135.53	2.15	21.00	14.75	0.76
8.50	124.62	2.59	22.00	13.04	0.95
9.00	114.57	2.41	23.00	11.12	0.51
9.50	109.89	1.84	24.00	10.38	0.56
10.00	100.00	2.00	25.00	9.16	0.69
10.50	93.27	2.35	26.00	8.51	0.68
11.00	86.61	2.16	27.00	7.79	0.49
11.50	80.25	1.63	28.00	8.04	0.49
12.00	72.88	1.21	29.00	7.30	0.54
12.50	67.56	0.96	30.00	6.92	0.48
13.00	61.80	1.51	31.00	6.72	0.48
13.50	56.68	1.25	32.00	6.35	0.48
14.00	51.17	0.99	34.00	6.69	0.48
14.50	46.34	0.95	36.00	5.78	0.48
15.00	42.03	0.81	38.00	5.91	0.52
15.50	36.85	0.83	40.00	5.58	0.48
16.00	34.77	0.84			

Table 4: *Neon-chlorine* (612 K)

Θ	Signal	Δ	Θ	Signal	Δ
4.50	354.49	2.85	14.25	32.88	0.52
4.75	325.36	2.32	14.50	30.77	0.62
5.00	309.16	2.21	14.75	29.26	0.83
5.25	297.32	1.59	15.00	27.79	0.50
5.50	284.77	1.57	15.25	26.18	0.58
5.75	265.80	2.66	15.50	24.66	0.47
6.00	245.04	1.76	15.75	23.25	0.47
6.25	231.61	1.39	16.00	21.86	0.57
6.50	222.94	1.95	16.25	20.73	0.54
6.75	214.94	2.00	16.50	19.49	0.54
7.00	205.26	1.51	16.75	18.73	0.42
7.25	191.62	1.18	17.00	17.55	0.51
7.50	178.33	2.03	17.25	17.02	0.54
7.75	167.23	2.69	17.50	16.27	0.69
8.00	160.18	1.77	17.75	15.31	0.42
8.25	154.53	1.37	18.00	14.61	0.37
8.50	144.44	1.38	18.25	14.22	0.53
8.75	136.04	1.13	18.50	13.84	0.37
9.00	125.47	1.14	18.75	12.94	0.42
9.25	118.04	1.38	19.00	12.79	0.37
9.50	111.57	1.86	19.25	12.03	0.58
9.75	106.35	1.48	19.50	11.80	0.37
10.00	100.00	1.00	19.75	11.11	0.56
10.25	93.33	0.68	20.00	11.04	0.78
10.50	86.24	0.62	21.00	9.65	0.51
10.75	80.43	0.65	22.00	8.97	0.80
11.00	76.41	0.76	23.00	8.27	0.40
11.25	71.52	0.83	24.00	7.89	0.40
11.50	67.60	0.55	25.00	7.22	0.93
11.75	63.29	0.58	26.00	7.07	0.39

- continued -

Table 4: continued

Θ	Signal	Δ	Θ	Signal	Δ
12.00	59.19	0.76	27.00	6.50	0.50
12.25	55.25	0.54	28.00	6.72	0.38
12.50	51.93	0.67	29.00	6.01	0.38
12.75	48.82	0.66	30.00	6.22	0.38
13.00	45.50	0.52	32.00	5.38	0.69
13.25	43.00	0.86	34.00	5.60	0.38
13.50	39.87	0.61	36.00	5.39	0.50
13.75	37.38	0.47	38.00	5.16	0.38
14.00	35.19	0.60	40.00	4.63	0.47